

Numerical Modeling of 3-Dimensional Surface Separation

By

Randolph Richard Settgaest

B.S. (University of California, Davis) 1996

M.S. (University of California, Davis) 1998

DISSERTATION

Submitted in partial satisfaction of the requirements for the degree of

DOCTOR OF PHILOSOPHY

in

CIVIL AND ENVIRONMENTAL ENGINEERING

in the

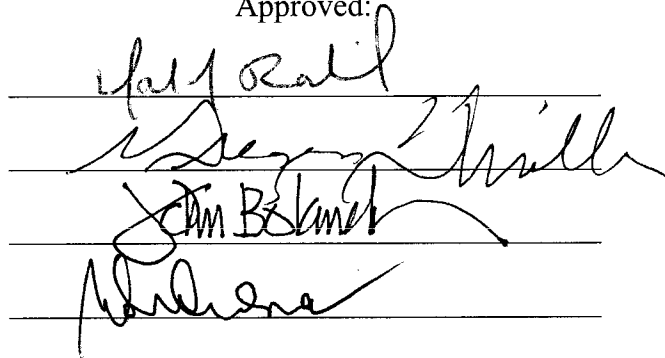
OFFICE OF GRADUATE STUDIES

of the

UNIVERSITY OF CALIFORNIA

DAVIS

Approved:

Four handwritten signatures are written on four horizontal lines. The signatures are in black ink and appear to be of varying styles, some more cursive and others more blocky.

Committee in Charge

(2006)

UMI Number: 3212882

INFORMATION TO USERS

The quality of this reproduction is dependent upon the quality of the copy submitted. Broken or indistinct print, colored or poor quality illustrations and photographs, print bleed-through, substandard margins, and improper alignment can adversely affect reproduction.

In the unlikely event that the author did not send a complete manuscript and there are missing pages, these will be noted. Also, if unauthorized copyright material had to be removed, a note will indicate the deletion.

UMI[®]

UMI Microform 3212882

Copyright 2006 by ProQuest Information and Learning Company.

All rights reserved. This microform edition is protected against unauthorized copying under Title 17, United States Code.

ProQuest Information and Learning Company
300 North Zeeb Road
P.O. Box 1346
Ann Arbor, MI 48106-1346

Abstract

Embedding cohesive surfaces into finite element analysis is a widely used technique for the numerical simulation of surface separation (i.e., crack propagation). The cohesive zone method applies cohesive tractions to the separating surfaces to simulate the effects of rupturing material. Typically, a traction-separation law is used to relate the magnitude of the cohesive tractions to the distance between the separating surfaces. Use of this simple relation results in a potentially overly simplistic theory, as issues such as crack-tip constraint levels are inherently ignored. In this study, the "Cohesive Continuum Framework" (CCF) is presented as a new 3-dimensional method for calculating the response of material undergoing the separation process. The CCF presents the concept of a kinematic tensor that includes contributions from the standard deformation gradient, gap vector, and a length scale. This tensor is used to update a material state using the same constitutive law as the surrounding bulk material. This material state is then used to generate cohesive stresses that are applied to the body. As the definition of such a tensor requires certain assumptions be made regarding the configuration of the rupturing material, two separate formulations are presented in this study. The Finite Thickness Layer Formulation (FTLF) assumes that the rupture process occurs across a layer of material with non-zero thickness, while the Surface Based Formulation (SBF) assumes that the rupture process occurs across a 2-dimensional surface. The CCF also specifies that a material rupture function be defined in order to quantify the progression towards complete rupture of a particular material state in a particular direction. The CCF is implemented in an explicit 3-dimensional finite element code. Various analyses using both linear elastic and Gurson void growth constitutive relations are presented in order to

display basic features of the CCF. A 3-point bend specimen is simulated, and provides good agreement with experimental results. The results of presented analyses indicate that the Cohesive Continuum Framework provides the natural ability to capture any dependencies on stress triaxiality near the crack tip, and represents a substantial contribution to the state of the art in computational fracture mechanics.

TABLE OF CONTENTS

1	<i>Introduction</i>	1
1.1	Conventional Fracture Mechanics	2
1.1.1	Linear Elastic Fracture Mechanics	2
1.1.2	Elastic-plastic Fracture Mechanics	8
1.2	Cohesive Zone Methods	10
1.3	Motivation for the Cohesive Continuum Framework	17
2	<i>The Cohesive Continuum Framework</i>	19
2.1	Preliminary Kinematics	20
2.2	General Methodology of The Cohesive Continuum Framework	22
2.2.1	Material Rupture Function	24
2.2.2	Enriched Kinematics	26
2.2.2.1	Finite Thickness Layer Approach	26
2.2.2.2	Surface Based Formulation	30
2.2.2.3	Enriched Kinematics Features	33
2.2.3	Cohesive Stresses	35
2.2.3.1	Finite Thickness Layer Assumption	36
2.2.3.2	Surface Based Approach	38
2.3	Summary	40
3	<i>Finite Element Method Implementation</i>	42
3.1	Finite Element Preliminaries	42
3.1.1	FEM Equations of Motion	42
3.1.2	Time Stepping	44
3.1.3	Element Formulation	46
3.1.4	Kinematics for Constitutive Input	49
3.2	Implementing the Cohesive Continuum Framework	50
3.2.1	Modeling the Rupturing Material	50
3.2.2	Tracking and Integrating Material States	50
3.2.2.1	Finite Thickness Layer Approach	50
3.2.2.2	Surface Based Approach	53
3.2.2.3	Other Considerations	54
3.2.3	Element Splitting and Node Duplication	54
3.2.4	Cohesive Stresses and Nodal Forces	56
3.2.4.1	Finite Thickness Layer Formulation	57
3.2.4.2	Surface Based Formulation	58
3.2.5	Cohesive Damping Traction and Anti-Intrusion Traction	61
3.3	Summary	63
4	<i>Numerical Results</i>	64
4.1	Material Models	64
4.1.1	Linear Elasticity	64
4.1.2	Gurson Void Growth	66
4.1.3	Material Model Summary	69
4.2	Elementary Model Behavior	69
4.2.1	Uniaxial Behavior	70
4.2.1.1	Linear Elastic Material	72
4.2.1.2	Gurson Material	74

4.2.2	Multiaxial Cyclic Behavior	75
4.2.3	Time Continuity	81
4.3	Mesh Refinement Study on a Double Cantilever Beam	83
4.4	Mesh Refinement Study on a Periodic Plate	89
4.5	CCF Gurson Model Calibration	94
4.6	Simulation of a Uniaxial Tension Test	97
4.7	Simulation of a 3-Point Bend Specimen	100
4.8	Confinement Study of a 3-point Bend Specimen	107
4.9	Summary	110
5	<i>Summary and Direction of Future Work</i>	<i>112</i>
	<i>References</i>	<i>116</i>

TABLE OF FIGURES

Figure 1.1: Crack in an Infinite Plate	3
Figure 1.2: J-integral	6
Figure 1.3: Nonlinear Elastic Unload vs Elastic Plastic Unload	9
Figure 1.4: Strip-Yield Model.....	10
Figure 1.5: Double Cantilever Beam.....	13
Figure 1.6: Existing Traction Separation Laws	13
Figure 2.1: Arbitrary Body Containing an Internal Surface.....	21
Figure 2.2: Separation Region Diagram.....	22
Figure 2.3: Separation Layer Diagram	22
Figure 2.4: Internal Points from Γ for Surface Based Formulation	32
Figure 2.5: Vector δz and $\bar{F}N$ Comparison for Surface Based Formulation	33
Figure 2.6: Energy Limiter Scenarios Illustrated.....	40
Figure 3.1: Parent Element and Nodal Coordinates.....	46
Figure 3.2: Separation Layer Λ as Portion of Bulk Elements.....	51
Figure 3.3: Diagram of Double-Point Integration for Λ	52
Figure 3.4: Diagram of Eight-Point Integration for Λ	52
Figure 3.5: Internal Point Definition for FE Implementation of Surface Based Formulation.....	54
Figure 3.6: Facet-Based Nodal Duplication Scheme	56
Figure 4.1: Illustration of Simple Test-Plate Mesh.....	70
Figure 4.2: Cohesive Traction vs Gap Opening for Finite Thickness Layer Formulation Under Uniaxial Strain Loading – Linear Elastic.....	71
Figure 4.3: Cohesive Traction vs Gap Opening for Surface Based Formulation Under Uniaxial Strain Loading – Linear Elastic.....	72
Figure 4.4: Cohesive Nodal Forces vs Gap Opening for Surface Based Formulation Under Uniaxial Strain Loading – Linear Elastic.....	74
Figure 4.5: Cohesive Traction vs Gap Opening for Finite Thickness Layer Formulation Under Uniaxial Strain Loading – Gurson	75
Figure 4.6: Complex Load Path for Test-Plate	76
Figure 4.7: FTLF Linear Elastic Cyclic Traction Separation Plots	79
Figure 4.8: SBF Linear Elastic Cyclic Traction Separation Plots.....	80
Figure 4.9: Deformed Double Cantilever Beam Meshes	84
Figure 4.10: Opening Force (LPF @10,000 Hz) per unit Thickness vs CMOD for Linear Elastic Double Cantilever Beam (Finite Thickness Layer Formulation).....	87
Figure 4.11: Rate of Energy Dissipation vs Crack Extension for Linear Elastic Double Cantilever Beam (Finite Thickness Layer Formulation).....	88
Figure 4.12: Opening Force (LPF @10,000 Hz) per unit Thickness vs CMOD for Linear Elastic Double Cantilever Beam (Surface Based Formulation).....	88
Figure 4.13: Rate of Energy Dissipation vs Crack Extension for Linear Elastic Double Cantilever Beam (Surface Based Formulation)	89
Figure 4.14: Illustration of Periodic Plate Meshes.....	91
Figure 4.15: Periodic Plate – Force vs Time	92
Figure 4.16: Periodic Plate – Energy Rate vs Normalized Crack Extension.....	93

Figure 4.17: Crack Velocity vs Normalized Crack Extension.....	94
Figure 4.18: Uniaxial Tension Test Simulation After Necking Occurs	97
Figure 4.19: Failure of a Uniaxial Tension Test Specimen. Necked Meshes with Cohesive Elements in Red, and Stress Strain Plot including Experimental Data.	99
Figure 4.20: Uniaxial Tension Test - Cohesive Traction vs Gap Opening at Various Radii	100
Figure 4.21: Schematic of 3-Point Bend Test.....	101
Figure 4.22: Mesh Used in Simulation of 3-point Bend Test.....	102
Figure 4.23: Deformed Mesh From Simulation of 3-point Bend Test.....	103
Figure 4.24: Rupture Zone Taken From the Simulation of a 3-point Bend Test.....	104
Figure 4.25: 3-Point Bend Simulation – Applied Top Force vs. CMOD.....	105
Figure 4.26: Dissipation Rate vs Crack Extension for Simulated 3-point Bend Test.....	106
Figure 4.27: J-R Curve For Simulated 3-point Bend Test.....	107
Figure 4.28: Sheet Mesh of 3-point Bend Specimen	108
Figure 4.29: Force Per Unit Thickness vs CMOD from 3-point Bend Sheet Mesh	109
Figure 4.30: Energy Dissipation Rate vs Crack Extension from 3-point Bend Sheet Mesh	109

1 Introduction

The generation of new surfaces in continuous bodies is a fundamental problem in the design and analysis of structures. Failure of structures, man-made or natural, typically involves the creation of a new surface, where the assumptions of continuum mechanics no longer apply. For example, the rupture of a pressure vessel typically begins with the growth of micro-cracks along the outer surface of the vessel. As the pressure in the vessel is increased, the material surrounding the micro-crack will reach a state such that the micro-crack extends through the material, thereby creating a new free surface. In a seemingly unrelated scenario, consider the standard slope stability problem in geotechnical engineering. Failure of the slope can occur due to in a section of material sliding along a “failure plane” that begins as a layer of highly deformed material. The common trait between these examples is that they both involve the creation of new external surfaces. It is the creation of this new surface through a once continuous body that violates the assumptions of traditional continuum based engineering approaches. Specifically, continuum mechanics assumes that the body is contiguous, contains no discontinuities, and does not generate new surfaces. In other words, interior points remain on the interior of the body. This assumption is obviously violated by the creation of a crack or failure plane, both of which signify a displacement discontinuity, running through the body.

The need to analyze bodies that may contain displacement discontinuities led to the development of the field generally known as fracture mechanics. As a gross generalization, the contribution that fracture mechanics makes to existing continuum

theory is the inclusion of a length scale. Defining a length scale in an appropriate manner facilitates the ability to model features inside an otherwise “continuous” body.

1.1 Conventional Fracture Mechanics

1.1.1 Linear Elastic Fracture Mechanics

The term Linear Elastic Fracture Mechanics (LEFM) is used to describe a class of problems that involve the extension of a crack through a linear elastic body. The topics introduced through a discussion of LEFM provide the fundamentals that are used to extend fracture mechanics theory to non-linear materials.

First consider the process of fracture from an atomistic point of view. If fracture is assumed to be nothing more than the breaking of atomic bonds, then the potential energy function that describes the bond between two atoms may be used to estimate the stress required to break that bond. An elementary order-of-magnitude calculation of the stress that is required break the bond (Anderson [1]) leads to:

$$\sigma_c = \frac{E}{\pi}, \quad (1.1)$$

where E is the Young’s modulus of the material. However, the experimental fracture strength of a material is typically orders of magnitude less than this σ_c . The reason for this discrepancy is that any real material is not a perfect lattice, and thus fracture is not accurately described by the simultaneous breaking of atomic bonds. Specifically, the presence of imperfections (i.e., flaws, micro-cracks) will result in stress concentrations in the near-tip region. Inglis [2], who studied elliptical holes in a flat plate, provided a quantitative basis to this statement when he calculated infinite stress at the tip of a

perfectly sharp crack. While it is not physically possible to have a perfectly sharp crack, as the atomic spacing provides a lower bound on crack tip radius, the results of Inglis' work proves that a severe stress concentration exists near the crack tip.

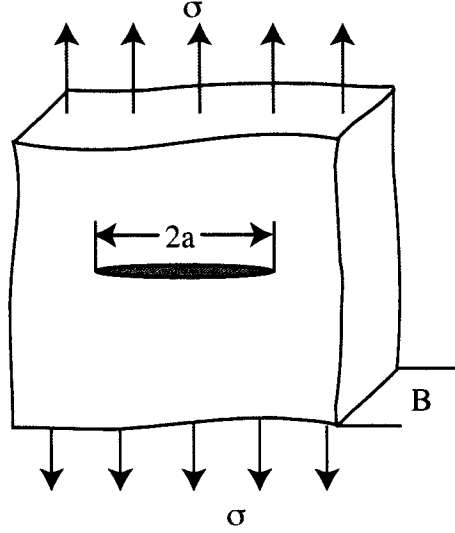


Figure 1.1: Crack in an Infinite Plate

In 1920 Griffith [3] applied thermodynamics to the extension of a pre-existing through-thickness crack of length $(2a)$ in an infinite plate of finite thickness (B) subject to a stress (σ) in one direction as shown in Figure 1.1. Griffith stated that for an incremental increase in crack area (dA) , the sum of the change of the potential energy of the body (Π) and the work required to generate new free surfaces (W_s) must be equal to zero, thus maintaining the total energy (E_t) of the system remains constant. This may be expressed as:

$$\frac{dE_t}{dA} = \frac{d\Pi}{dA} + \frac{dW_s}{dA} = 0. \quad (1.2)$$

Through the stress analysis of Inglis[2], the potential energy of an infinite plate of thickness (B) with a crack of length $2a$ is:

$$\Pi = \Pi_0 - \frac{\pi\sigma^2 a^2 B}{E}, \quad (1.3)$$

where Π_0 is the potential energy of an uncracked plate. Differentiation of equation (1.3) with respect to crack area yields the *rate of energy dissipation*, or what is commonly referred to as the *energy release rate* (G). This rate of energy dissipation is the amount of energy required to extend the crack area by some infinitesimal amount dA :

$$G = -\frac{d\Pi}{dA} = \frac{\pi\sigma^2 a}{E}. \quad (1.4)$$

The work required to create a new crack of length $2a$ may be defined using the surface energy (γ_s):

$$W_s = 4aB\gamma_s. \quad (1.5)$$

Substituting equations (1.4) and (1.5) into (1.2) leads to a relation for the stress required to extend the crack (fracture stress):

$$\sigma_f = \sqrt{\frac{2E\gamma_s}{\pi a}}. \quad (1.6)$$

Note that the fracture stress in equation (1.6) is the remote stress applied to the plate, not the local stress at the crack tip. Thus, Griffith's energy based approach to fracture effectively circumvents the difficulty of dealing with an unbounded stress field in the body. However, Griffith's approach requires an estimate of the surface energy γ_s , which may not be readily available.

Another approach to linear elastic fracture is through stress analysis of the crack tip region. Through work by Westergaard [4], Irwin [5], Sneddon [6], and Williams [7], the stress field near the crack tip due to a remote load σ may generally be expressed in polar coordinates as:

$$\sigma_{ij} = \frac{K}{\sqrt{2\pi r}} f_{ij}(\theta). \quad (1.7)$$

Note that equation (1.7) contains $1/\sqrt{r}$, and thus the stress field approaches infinity as the crack tip is approached. The variable K is known as the *stress intensity factor*. If the singularity is regarded as a byproduct of mathematical assumptions used to approximate the stress field (i.e., perfect linear elasticity with an infinitely sharp crack), the stress intensity factor provides a finite value that quantifies the magnitude of the stress field in the region of the crack tip. The units for the stress intensity factor are stress*(length)^{1/2}, thus its use as a fracture parameter introduces the requisite length scale into the fracture theory.

The stress intensity factor may be utilized to predict fracture in brittle materials through a simple procedure. A pre-cracked specimen of simple geometry is loaded until the crack propagates. The value of K is calculated for the conditions (i.e., remote stress) at which the propagation occurs and is recorded as the critical stress intensity factor (K_c). The variable K_c is considered a material parameter, and thus may be used to characterize the material's resistance to fracture in other geometries. In other words, if K can be calculated for some arbitrary geometry, then that value of K may be compared to K_c . If K is less than K_c , then it is predicted that the crack does not extend. If K is greater than K_c , then it is predicted that the crack does extend, although it may not run through the entire specimen due to the change in geometry (which produces a change in K) caused by the extension of the crack.

In the most general case of unsymmetrical geometry and loading, three distinct stress-intensity parameters appear (K_I , K_{II} , K_{III}). Mode I represents normal opening separation, Mode II represents in plane shear, and Mode III represents out of plane shear. The stress intensity factors may be related to the energy release rate through:

$$G = \frac{K_I^2}{E'} + \frac{K_{II}^2}{E'} + \frac{K_{III}^2}{2\mu},$$

where :

$$E' = E \text{ for plane stress}$$

$$E' = \frac{E}{1 - \nu^2} \text{ for plane strain.}$$
(1.8)

Through equation (1.8), the procedure for the evaluations of crack growth outlined above may be applied to G rather than K . To this end, once K_c is determined for a loading condition, which may include multi-mode factors, G_c may be calculated through equation 1.8. Thus for any set of K 's there will be a value of G that may be compared to G_c to evaluate if the loading will initiate fracture. However, a given value of G_c is generally valid only for the particular relative proportions of K_I , K_{II} , and K_{III} under which the test was conducted.

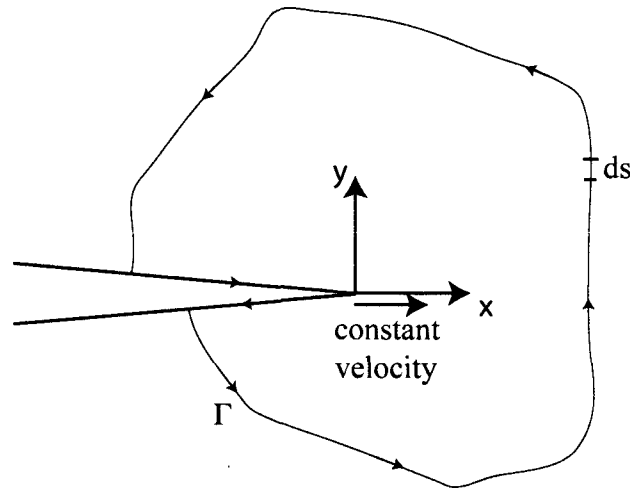


Figure 1.2: J-integral

Another important concept in fracture mechanics, and perhaps the most widely used, is the so-called J-integral. Rice [8] applied a path independent integral, which he called the J-integral, to the problem of a straight crack extending through a sheet of elastic material at constant velocity. He showed that the value of this integral is equal to the rate of energy dissipation that results from the extension of the crack, for an elastic material (i.e., $J=G$). Consequently, G may be calculated from J instead of the stress intensity factor. For the situation in Figure 1.2, the J-integral is defined as:

$$J = \int_{\Gamma} \left(w \, dy - t_i \frac{\partial u_i}{\partial x} \, ds \right),$$

(1.8)

where:

w = strain energy density

\mathbf{t} = traction vector

\mathbf{u} = displacement vector.

As this integral can be shown to be path-independent, the path that provides the simplest calculation of J may be selected. Specifically, a path may be chosen such that the components of the J-integral are calculated using far-field quantities (i.e., no consideration of the near-tip fields is required). Thus, the J-integral provides a much simpler means to evaluate the potential for fracture in elastic bodies than the use of stress intensity factors, which requires a characterization of the stress field the near-tip region.

As previously stated, LEFM assumes that the body is composed of linear elastic material. If this assumption is strictly enforced, the applicability of LEFM to real-world problems is rather limited. To assess the applicability of LEFM to real materials that yield near the crack tip, the concept of *small-scale yielding* is introduced. Small-scale yielding refers to the relation between the size of the plastic zone surrounding the crack tip, and the overall size of the body. If the size of the plastic zone is comparable to the size of the specimen,

then small-scale yielding does not apply and LEFM cannot be used. If however the size of the plastic zone is small compared to the size of the specimen, then small-scale yielding is said to apply and LEFM provides a valid estimate of the near-tip stress field.

1.1.2 Elastic-plastic Fracture Mechanics

LEFM is not suited to predict fracture when considering materials that exhibit a significant amount of plastic deformation away from the crack tip. Specifically, LEFM performs poorly when the energy dissipation associated with plastic deformation of the body is much greater than the energy required to create a new surface. This is in fact the case in most metallic materials.

The term Elastic-Plastic Fracture Mechanics (EPFM) is generally used to describe the analysis of fracture in an inelastic material. The most common approach to fracture in an elastic-plastic material is to attempt to mimic the inelastic behavior with a nonlinear elastic material. This behavior is typically achieved through use of the Ramberg-Osgood relation for uniaxial loading:

$$\frac{\varepsilon}{\varepsilon_y} = \frac{\sigma}{\sigma_y} + \alpha \left(\frac{\sigma}{\sigma_y} \right)^n, \quad (1.8)$$

where ε_y and σ_y are the yield strain and stress respectively, and n is a hardening exponent.

Power law elasticity of this type results in a stress field singularity that is often referred to as the HRR singularity after Hutchinson [9] and Rice and Rosengren [10]. The use of a nonlinear elastic material is justified by the simple assertion that under monotonic loading, stress-strain curve of the nonlinear elastic material can appear identical to that of

a to a plastic material. However this reasoning breaks down if the material unloads (Figure 1.3), as for example occurs with actual crack extension. For this reason, EPFM is only useful to model crack initiation.

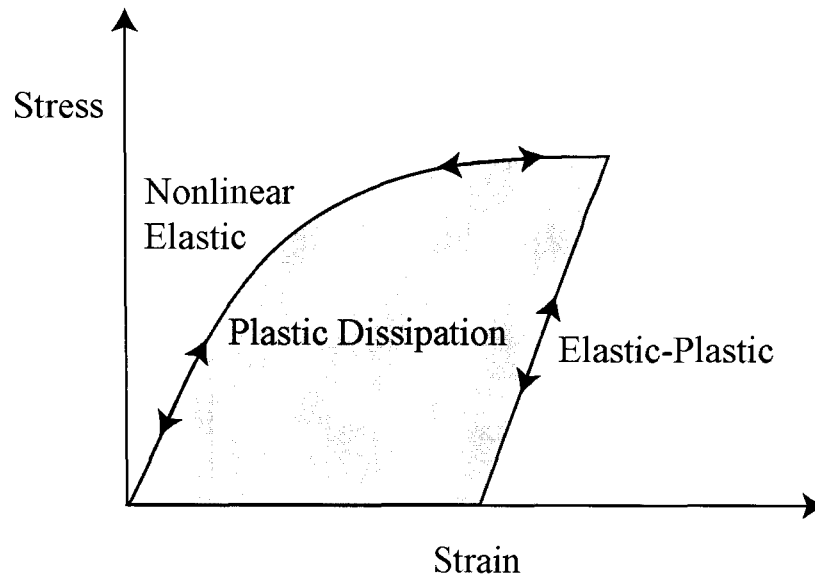


Figure 1.3: Nonlinear Elastic Unload vs Elastic Plastic Unload

Perhaps the most significant use of the nonlinear elastic assumption is in connection with the J-integral. It should be noted that the constant velocity crack growth assumption of the J-integral implies that a portion of the material is in the process of unloading. In particular, material in the wake of the crack tip undergoes significant unloading. Under the nonlinear elastic assumption, this unloading process will follow the nonlinear elastic curve back to the origin defined by equation (1.8), rather than the linear elastic unload expected from a real elastic-plastic material. This results in a situation where all energy associated with the loading of the near-tip region is returned as mechanical energy. This differs from elastic-plastic loading where a significant portion of this energy is dissipated

(Figure 1.3). For these reasons, J-integral based EPFM does not offer legitimate predictions of crack behavior after crack extension initiates.

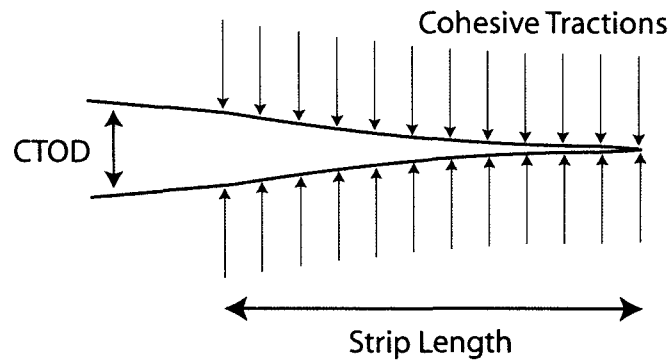


Figure 1.4: Strip-Yield Model

1.2 Cohesive Zone Methods

The use of cohesive zone methods in finite element modeling is prevalent in modern computational fracture mechanics. The so-called strip-yield model of Dugdale [11] and analysis of Barenblatt [12] represent the genesis of modern cohesive zone models. While their motivations were different (Barenblatt envisioned inter-atomic forces, whereas Dugdale envisioned plastic material deformation in macroscopic, ductile specimens), they both postulated that a finite length strip of material could be placed directly behind the crack tip to provide a closing traction, as shown in Figure 1.4. In Dugdale's model, this closing traction, or *cohesive traction*, is taken equal to the yield stress of the material, while the length of the strip is determined by requiring that the effects of the traction cancel the stress singularity from the remote load. In other words, a linear analysis of the near-tip region subject to the cohesive tractions alone shows a stress singularity as the crack tip is approached. The length of the strip is defined such that the stress intensity factor that results from the cohesive tractions is equal to the negative of the stress

intensity factor produced by the remote loading. Rather than focus on the specifics of the cohesive models as originally proposed, the following discussion abstracts the general scheme of the cohesive zone method.

Consider a linear elastic body with a crack that contains a cohesive zone near the crack tip. This cohesive zone is fully described by a cohesive traction (t_c) of variable magnitude (with a maximum value equal to the yield stress σ_y), and is applied over some constant length (α). Now consider that the body is subjected to remote loading (σ) some distance from the crack. This remote loading results in a stress singularity in the near-tip region which is referred to as K_σ for the purposes of this discussion. In response to this, the magnitude of the cohesive traction may be increased such that it results in a stress singularity (K_t) that is equal to the negative of K_σ . Since the body is linear elastic, superposition applies and the singular terms in the stress fields will cancel with each other. Thus as the remote load is increased, the cohesive traction may be increased (up to its yield stress) in such a manner that no singular stress field will result from the combined loading. As the remote loading is increased indefinitely, the cohesive traction will eventually reach its maximum value (σ_y). After the cohesive stress has reached its maximum, any increase in the remote load will result in a singular stress field. It is assumed that the infinite stress at the crack tip implies that the material at this point must rupture, thus the crack must extend. In a problem such as the infinite plate shown in Figure 1.1, the remote stress at which this occurs could be considered the fracture stress (σ_f).

Because the infinite plate problem is an example of unstable crack growth (i.e., any increase in the crack size will decrease the fracture stress), consider a problem that exhibits stable crack growth. Stable crack growth implies that any extension of the crack will result in a reduction in stress near the crack tip. One such problem is the double cantilever beam shown in Figure 1.5. The ends of the beams are displaced at the rate (v), and the mid-plane between the upper and lower beams represents the crack path. As the ends of the beams are displaced, the crack tip region is loaded along with the cohesive zone as described above. Once the applied displacement is sufficient to cause the cohesive tractions to reach their maximum value, an additional displacement increment results in an infinite stress at the crack tip. Assuming that the material can withstand some finite maximum value (such as σ_y), the material at the crack-tip will rupture, thereby extending the crack. As the crack extends, the remote loading is reduced as a result of the change in geometry. The reduction in remote loading results in a reduction in K_I , which allows the system to remain stable. It is assumed that the cohesive zone follows the crack tip such that it remains of constant length (α) (i.e., the cohesive zone follows the crack tip), and thus the process may continue for further displacements. Note that if the crack is propagating at some arbitrary rate, the cohesive tractions are always equal to σ_y . Thus the rate of energy dissipation is equal to $(\sigma_y * CTOD_f)$, where $CTOD_f$ is the CTOD at the point that the cohesive traction is disengaged (i.e. the tail of the cohesive zone).

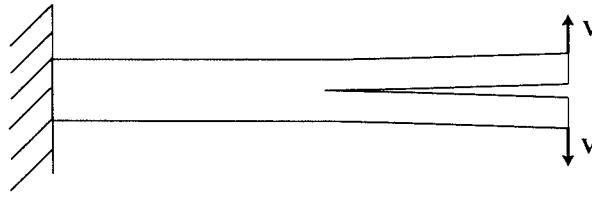


Figure 1.5: Double Cantilever Beam

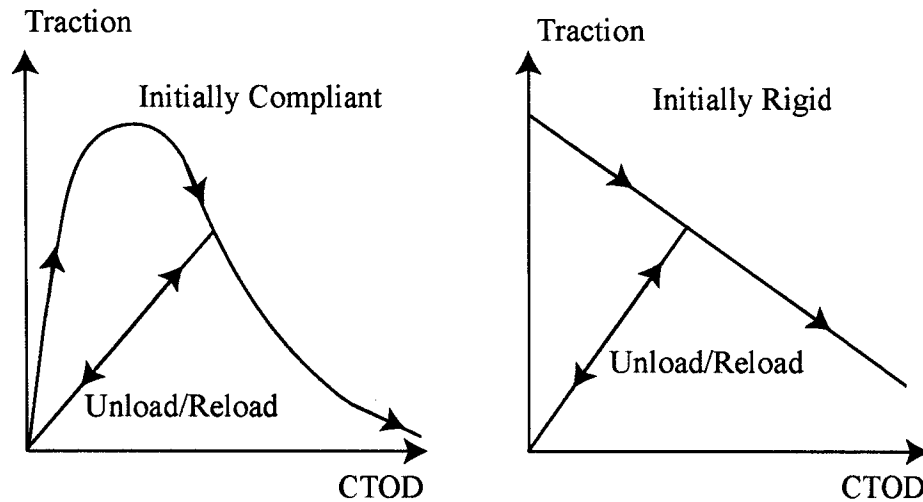


Figure 1.6: Existing Traction Separation Laws

The cohesive zone model as it is described in the literature is simply a generalization of the ideas described above. Rather than a simple cohesive traction that remains constant across a fixed length cohesive zone, the value of the cohesive traction is defined to be a function of the crack tip opening displacement (CTOD – See Figure 1.4) as in Barenblatt [12]. Needleman [13] implemented the cohesive zone model into the context of the finite element method. Needleman proposed an *initially compliant* traction separation polynomial of similar shape to the one shown in Figure 1.6. Subsequent proposals that vary the shape of the curve have been published, but the general nature of the curve (rising from zero gap opening to a plateau, then degrading until zero traction) remains. Rice and Wang [14] propose a traction separation based on atomic curve fits for solute

segregation. Needleman [15] and Xu and Needleman [16, 17, 18] propose a linear increase in traction followed by an exponential decay. Tvergaard and Hutchinson [19] propose a relation that consists of three linear sections, one rising from the origin, a flat segment, and a linear degradation to complete separation. Another type of traction separation is implemented in the *initially rigid* cohesive zone element utilized by Camacho and Ortiz [20,21] and Ortiz and Pandolfi [22]. The initially rigid cohesive zone element does not allow a displacement jump until certain criteria are met as illustrated in Figure 1.6.

The cohesive zone method has been implemented in finite element settings with some success. In particular, complex 3-dimensional problems involving fracture have been simulated using multi-axial cohesive zone methods, as shown by Camacho and Ortiz [20, 21]. However, there remain unresolved issues.

The initially compliant family of traction separation relations requires that the cohesive zone exist throughout the entire loading, even before appreciable stresses are present in the body. Upon loading, all cohesive zone elements are allowed to deform as per the initial compliance of the traction separation relation. If cohesive zones are specified at every inter-element facet, then the initial cohesive zone compliance introduces an unintended mesh dependence that culminates in zero stiffness under infinite mesh refinement. Klein and Foulk and Chen and Wimmer and Gao [23] provide a thorough discussion of the compliance problem, and suggest guidelines to mitigate such effects.

This mesh dependence may be avoided if the crack path is known prior to the analysis, so that cohesive zone elements may be specified only along the crack path. While this remedy is effective, setting a predetermined crack path represents a serious limitation for problems where the direction of the crack propagation is unknown a priori.

The initially rigid type of cohesive relations does not result in compliance problems. This type of cohesive element is only active once a criterion, such as a measure of stress or some type of damage parameter, is reached. However, these formulations contain their own set of complications. For example, the unload-reload curve of this relation is linear elastic through the origin. If the cohesive element is unloaded immediately after activation, then it is possible that the element will have an exceedingly high stiffness. Such a condition is sure to cause substantial problems with the numerical solution scheme used. Another issue with initially rigid cohesive relations is that they are not guaranteed to provide a time continuous solution, as discussed by Papoulia [24]. A time continuous method will ensure that the nodal forces generated by the cohesive tractions immediately after separation are equal to the nodal forces generated by the bulk elements (disconnected from the node in question after separation) immediately prior to separation. Thus, the node will not be subjected to any shock-type loading as a result of the separation. The reason that such a loading is of substantial concern is that the traction separation relations of the initially rigid cohesive zone methods typically are always of negative slope. The negative slope of the traction separation relation results in a condition where the overall problem loses its ellipticity, and difficulties ensue similar to those encountered when a softening material model is specified [25, 26, 27]. The problem may

be summed up by the following sequence of events. The non-physical shock load resulting from cohesive element initiation (typically multi-axial loading) will produce a gap opening that is not a result of the physical process, but rather the numerical solution procedure. This unintended gap opening will move the tractions down the traction-separation curve, thereby causing the cohesive element to degrade prematurely. This reduction of the cohesive tractions leads to further gap opening, which leads to a greater reduction in the tractions and so on. Papoulia [24] proposed an initially rigid formulation that enforces time continuity through a procedure that sets the initial value cohesive tractions such that the nodal forces remain continuous in time everywhere in the body. However, Papoulia points out that this formulation suffers traction locking, for which no remedy is available. Papoulia suggests that the cohesive traction gap opening relationship is insufficient for attaining numerically sound methods.

Another issue with the traction-separation relationship that governs the cohesive zone models is that it does not take the effects of near-tip constraints into account. The term constraint, as it is used here, refers to the level of triaxiality of the stress space. Consider that the effect of constraint, such as the specification of plane stress or plane strain, is an essential factor when formulating any mechanics problem. The fact that cohesive zone method does not intrinsically endow its traction separation relations with the ability to vary with the level constraint represents a significant shortcoming. Mathur, Needleman and Tvergaard [28] showed that the level of constraint has a strong influence over the fracture process if failure occurs through void growth and coalescence. Costanzo [29] contends that traction separation relations that specify cohesive traction based solely on

the opening displacement are not equipped to provide a realistic fracture model. He provides a generalized cohesive zone framework that accounts for deformations parallel to the fracture surface. Siegmund and Brocks [30, 31] also assert that the stress state at the crack tip (e.g., triaxiality, constraint) has significant influence on the process of surface separation for problems where void growth and coalescence are key factors in the separation process. Thus, a traction separation relation that has been formulated/calibrated for a low triaxiality condition will be inapplicable to a high triaxiality condition. To address this situation, Siegmund and Brocks propose that the traction separation relation vary with triaxiality.

1.3 Motivation for the Cohesive Continuum Framework

The preceding discussion highlights key features and weaknesses of current cohesive zone methods. The highlighted shortcomings of the cohesive zone method provide motivation for the formulation of a new cohesive theory. Much of the appeal of the cohesive zone method is its conceptual simplicity, as one only need specify a relation between cohesive traction and gap opening to develop a basic cohesive zone model. However, it is this simplistic viewpoint that makes the inclusion of features such as near-tip confinement difficult.

Therefore, in this dissertation a new type of cohesive zone approach called the Cohesive Continuum Framework (CCF) is introduced. The CCF differs from standard cohesive zone method in that it seeks to specify cohesive stresses from a complete 3D constitutive

response, rather than a simple 1D relationship (i.e., traction separation relation). For a complete description of the underlying approach of the CCF see chapter 2.

It is the goal of the CCF that the following conditions be met intrinsically:

- The effects of constraint near the crack tip are accounted for.
- The model user is relieved of the responsibility of specifying a traction-separation relation.
- Complete reversibility, and change of loading direction, are allowed and treated in a physically meaningful manner.
- Time continuity is achieved under mesh refinement.
- Unconditional mesh independence is achieved.

In chapter 2, the formulation of the Cohesive Continuum Framework is presented.

Chapter 3 discusses the details of implementing the CCF into a finite element setting.

Chapter 4 presents various numerical results aimed at displaying the capabilities of the CCF. Chapter 5 presents a summary of the efforts presented here.

2 The Cohesive Continuum Framework

When simulating a boundary value problem that requires the generation of new free surfaces, standard continuum methodologies typically fail. Techniques such as the so-called “cohesive zone method” may be added to the standard solution methods to introduce a length scale into the problem. As stated previously, the cohesive zone method applies cohesive tractions to a portion of the surfaces directly following the crack tip to achieve this. It is with this concept in mind that the Cohesive Continuum Framework (CCF) is introduced.

The Cohesive Continuum Framework seeks to provide an enrichment of standard continuum mechanics such that transitions from a standard continuum boundary value problem to a surface separation boundary value problem are admitted naturally. The CCF may also be viewed as an effort to extend the general cohesive zone method by replacing the “traction-separation law” with a relation derived from a fully 3-dimensional material state that is dependent on a standard continuum based constitutive law. The CCF is not limited to the application of a “cohesive traction” and will typically involve more complicated constraints applied to separating regions. In a homogeneous boundary value problem, the CCF mandates that the material response that is used to generate any constraints on the separating surfaces will derive from the same constitutive law that governs the bulk continuum (i.e., the material away from the separating region). As will become evident from the contents of this chapter, it is this dependence on continuum constitutive law that allows the CCF to provide a smooth transition from a standard

continuum BVP to a surface generation BVP while accounting for level of constraint in the surrounding bulk.

The definition of the CCF begins with a description of the body that is subject to surface generation. Once the components of the body have been defined, the general approach of the CCF is outlined. From there the specifics of each component of the CCF are described in detail.

2.1 Preliminary Kinematics

Consider a material body that occupies an open spatial region B , and is bounded by the surface ∂B at the current time (t). This body can also be said to occupy the open region B_0 , and be bounded by the surface ∂B_0 at some reference time prior to any surface separation as illustrated in Figure 2.1. An arbitrary material point may be defined such that its position is $\mathbf{x} \in B$ and $\mathbf{X} \in B_0$ in the current and reference configurations respectively. Now consider an arbitrary surface $\Gamma_0 \subset B_0$ with unit normal \mathbf{N} and tangent unit vectors \mathbf{M}_α ($\alpha=1, 2$) such that $\{\mathbf{N}, \mathbf{M}_1, \mathbf{M}_2\}$ form an orthonormal triad at every point on Γ_0 . The surface Γ_0 will be called the *rupture surface*, as it is the surface that ultimately separates into a pair of new boundary surfaces. For any point $\mathbf{X} \in \Gamma_0$, there exists an open neighborhood $R \subset B_0$ of \mathbf{X} such that $R = R^+ \cup R^- \cup (R \cap \Gamma_0)$ where $R^+ \cap R^- = \emptyset$; i.e. the surface Γ_0 divides the region R into two disjoint open regions $R^{+,-}$ (Figure 2.2). The surfaces $(\bigcup_{\mathbf{x} \in \Gamma_0} \partial R^{+,-} \cap \Gamma_0)$ are referred to as $\Gamma_0^{+,-}$ respectively. Whereas $\Gamma_0^{+,-}$ are geometrically identical to Γ_0 , their respective outward unit normal vectors $\mathbf{N}^{+,-}$ satisfy $\mathbf{N}^+ + \mathbf{N}^- = \mathbf{0}$. The

current position vector and surface limited deformation gradients $\forall \mathbf{X} \in \Gamma_0^{+,-}$, are defined as:

$$\mathbf{x}^{+,-} = \lim_{\xi \rightarrow 0^+} \mathbf{x}(\mathbf{X} - \xi \mathbf{N}^{+,-}) \quad (2.1)$$

$$\mathbf{F}^{+,-} = \lim_{\xi \rightarrow 0^+} \mathbf{F}|_{\mathbf{X} - \xi \mathbf{N}^{+,-}} \quad (2.2)$$

Further, we define the *gap vector* on Γ_0 as:

$$\mathbf{v} = \mathbf{x}^+ - \mathbf{x}^-, \mathbf{X} \in \Gamma_0 \quad (2.3)$$

Now consider that there exists a pair of surfaces $\partial\Lambda_0^{+,-}$ such that for all $\mathbf{X} \in \Gamma_0$

$$\partial\Lambda_0^{+,-} = \mathbf{X} - \frac{\lambda}{2} \mathbf{N}^{+,-} \quad (2.4)$$

The surfaces $\partial\Lambda_0^{+,-}$ may be used as bounds in the definition of a material layer Λ_0 . This layer has a finite thickness equal to λ in the reference configuration, and is shown in Figure 2.3. This layer is bisected by Γ , and thus may utilize the orthonormal triad $\{\mathbf{N}, \mathbf{M}_1, \mathbf{M}_2\}$ defined in Figure 2.1 as a coordinate frame.

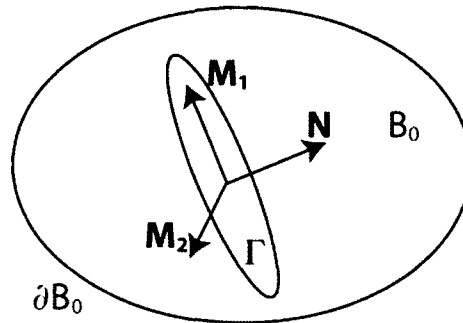


Figure 2.1: Arbitrary Body Containing an Internal Surface

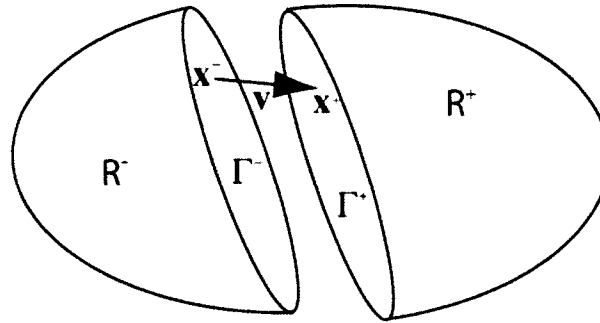


Figure 2.2: Separation Region Diagram

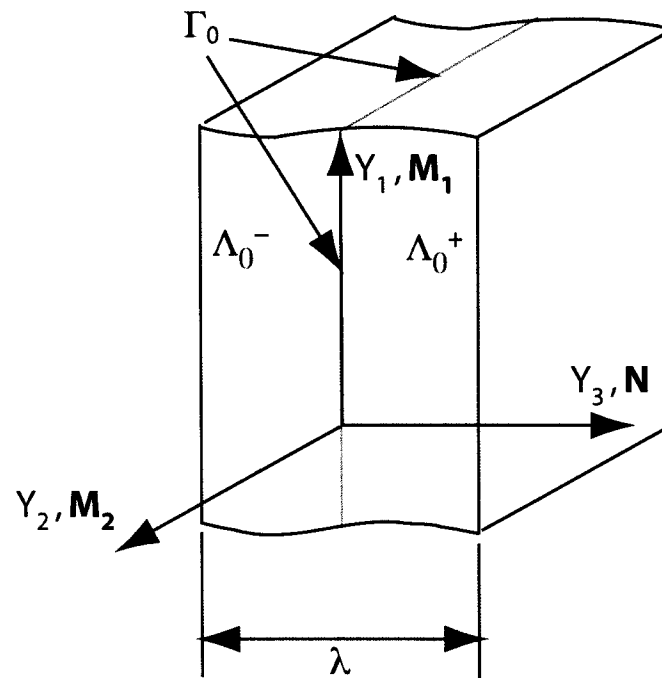


Figure 2.3: Separation Layer Diagram

2.2 General Methodology of The Cohesive Continuum Framework

The Cohesive Continuum Framework provides a flexible tool that may be used to simulate surface separation in an arbitrary body. In addition to standard continuum mechanics, the CCF introduces three new concepts in its definition. First, a *material rupture function* Φ is defined to provide a quantitative measure of the material's progression in the rupture process. This quantity will be used to dictate the location and

direction of material rupture. Once a rupture function has been defined, assumptions must be made about the configuration of the rupturing material so that enriched kinematics may be defined for the rupturing material. For instance, one could assume that the material undergoing the separation process exists only for $\mathbf{X} \in \Gamma_0$ (i.e., ruptured material exists on the rupture surface). This *surface based formulation* (SBF) is similar to standard cohesive zone approaches, as a simple traction-separation constitutive relation will only involve quantities taken from the rupture surface. Another option is to assume that there exists a finite thickness layer (Λ) shown in Figure 2.3. In this *finite thickness layer formulation* (FTLF) the physical process of rupture is assumed to occur over a finite volume in contrast with the surface based formulation that assumes that the rupture material possesses no volume. The inclusion of a rupture volume gives the finite thickness layer formulation certain advantages over the surface based formulation, as is be discussed in section 2.3. In the following sections both the surface based and finite thickness approaches will be explored. It is worthwhile to note that a substantial amount of the time spent on researching this topic was spent attempting to produce a stable version of the surface based formulation. The goal of a surface based formulation eventually yielded to the finite thickness layer formulation. However the development of the finite thickness layer formulation provided key insights into the source of the difficulties encountered with the surface based formulation. These insights have led to the development of energy limiters (discussed in section 2.2.3.2), which are essential for the stability of the surface based formulation.

Once material rupture has initiated, and the assumptions regarding the rupturing material configuration are made, enriched kinematics must be defined for the rupturing material regions. It is within the enriched kinematics that a length scale will be incorporated into the formulation. The enriched kinematics are then used to generate suitable input to a standard local constitutive relation. Lastly, the material state that results from the enriched kinematics must be applied to the body (i.e., cohesive tractions, etc.) in some physically consistent manner.

2.2.1 Material Rupture Function

The *material rupture function* $\Phi(Q, \mathbf{X}, \mathbf{N})$ provides a scalar measure of the progression towards rupture in a particular direction. Input to the function consists of the material state Q , the position vector of the material point being evaluated \mathbf{X} , and the unit vector \mathbf{N} . The rupture function may be viewed as an operator on the material state that characterizes the potential for separation in the reference direction \mathbf{N} . In order to accurately model material rupture, the rupture function should have a dependence on variables that describe the process of rupture (e.g., void volume fraction in void growth and coalescence). Since the rupture function is given no other information other than the material state, position, and orientation, the constitutive model must provide these descriptors. Thus, the constitutive model must include state variables that can be used to adequately describe the rupture process. For instance, if a material were known to rupture through void growth and coalescence, use of a linear elastic constitutive model would be entirely inadequate. Therefore it is important to stress that the choice of constitutive model remains a primary factor in the behavior of any CCF implementation.

If it is assumed that a valid material state exists $\forall \mathbf{X} \in B_0$, then the rupture function may be calculated $\forall \mathbf{X} \in B_0$ in all orientations. To make use of the rupture function, a pair of critical values $\Phi_1(\mathbf{X})$ and $\Phi_2(\mathbf{X})$ are defined such that Φ_1 indicates the value of $\Phi(\mathbf{Q}, \mathbf{X}, \mathbf{N})$ at which the separation process begins, whereas Φ_2 indicates the value at which the separation process is complete. If $\Phi < \Phi_1 \quad \forall \mathbf{X} \in B_0$ in all orientations, then no rupture is indicated and the standard continuum BVP applies to the entire body B_0 . If there exists some material point $\mathbf{X} \in B_0$ where $\Phi_1 < \max_{\mathbf{N}} \Phi(\mathbf{Q}, \mathbf{X}, \mathbf{N}) < \Phi_2$, then there exists a rupture surface Γ_0 at \mathbf{X} with unit normal \mathbf{N} . Thus the path of the surface separation front is determined by the value of \mathbf{N} that maximizes Φ . For any material point for which $\Phi(\mathbf{X}, \mathbf{N}, \mathbf{Q}) = \Phi_2$, the surfaces $\Gamma_0^{+, -} \in \partial B_0$ and are thereafter subject to external boundary conditions.

Also of note is that the inclusion of the position vector \mathbf{X} in Φ, Φ_1, Φ_2 allows for material heterogeneity in the body. Specifically, the rupture function itself may be given some dependence on the position, and/or the values of Φ_1, Φ_2 may vary with position. With this flexibility, both the bulk and fracture aspects of the material response can be tuned.

As a matter of convenience, we define the *separation coefficient* to track the extent of the separation process:

$$s = \begin{cases} 0 & \Phi \leq \Phi_1 \\ \frac{\Phi - \Phi_1}{\Phi_2 - \Phi_1} & \Phi_1 \leq \Phi \leq \Phi_2 \\ 1 & \Phi \geq \Phi_2 \end{cases} \quad (2.5)$$

$s \geq 0$.

As is evident from equation 2.5, the separation coefficient is a monotonically increasing function of Φ that varies linearly between values of zero at $\Phi=\Phi_1$, and unity at $\Phi=\Phi_2$.

2.2.2 Enriched Kinematics

Throughout the solution of a continuum boundary value problem, the deformation gradient \mathbf{F} and its history are taken as the kinematic basis by which “input” for any constitutive evaluation is calculated. As in the continuum problem, the Cohesive Continuum Framework relies on a local constitutive evaluation everywhere in the body B . However, the CCF also seeks to distribute the effects of a discontinuity (i.e., non-zero gap vector) across the layer Λ , thus a deformation gradient like tensor is proposed to replace \mathbf{F} . This gradient-like tensor, which is referred to as the *bridging tensor*, is used to define a material state that is useful for the purpose of assessing progression towards separation. In the following sections, suitable bridging tensors are discussed for the finite thickness layer approach as well as the surface based approach. It is strongly emphasized that these tensors are not truly deformation gradients in the conventional sense; instead, they serve as a kinematic basis by which to generate input to the bulk constitutive law on Γ . They are only useful to the extent that they lead to meaningful characterizations of the material state through the rupture process, and should not be considered as a valid means by which to transform actual vectors and tensors to the current configuration.

2.2.2.1 Finite Thickness Layer Approach

The Finite Thickness Layer approach assumes that there exists a layer of material where the rupture process occurs, as shown in Figure 2.3. The goal is to postulate a bridging tensor such that it is well defined $\forall \mathbf{X} \in \Lambda$ for situations where the gap vector is non-zero. The expression for the bridging tensor may be motivated by first considering a

companion displacement field \mathbf{u}_G . Making use of the coordinate frame defined in Figure

2.3, \mathbf{u}_G is defined as:

$$\mathbf{u}_G = \begin{cases} \mathbf{u} + \frac{(Y_3 + \lambda/2)}{\lambda} \mathbf{v} & -\lambda/2 \leq Y_3 \leq 0^- \\ \mathbf{u} + \frac{(Y_3 - \lambda/2)}{\lambda} \mathbf{v} & 0^+ \leq Y_3 \leq \lambda/2 \\ \mathbf{u} & \text{otherwise} \end{cases} \quad (2.6)$$

The companion displacement field seeks to distribute the displacement attributable to the gap vector linearly over the layer Λ_0 , which has a thickness λ centered on Γ . When the gap vector is equal to zero, the companion displacement field is equal to the physical displacement field (\mathbf{u}). However, when the gap vector attains a non-zero value, the physical displacement field is discontinuous while the companion displacement field remains continuous over the entire body B_0 . The *companion deformation gradient* (\mathbf{F}_G) may be calculated $\forall \mathbf{X} \in B_0$ taking the gradient of \mathbf{u}_G as follows:

$$\begin{aligned} \frac{\partial \mathbf{u}_G}{\partial \mathbf{X}} &= \frac{\partial \mathbf{u}}{\partial \mathbf{X}} + \frac{\partial}{\partial \mathbf{X}} \left(\frac{(Y_3 \pm \lambda/2)}{\lambda} \mathbf{v} \right) \\ \frac{\partial \mathbf{u}_G}{\partial \mathbf{X}} &= (\mathbf{F} - \mathbf{I}) + \frac{1}{\lambda} \left[(Y_3 \pm \lambda/2) \frac{\partial \mathbf{v}}{\partial \mathbf{X}} + \frac{\partial(Y_3 \pm \lambda/2)}{\partial \mathbf{X}} \mathbf{v} \right] \\ \delta_{ij} + \frac{\partial u_{Gi}}{\partial X_j} &= F_{ij} + \frac{1}{\lambda} \left[(Y_3 \pm \lambda/2) \frac{\partial v_i}{\partial X_j} + \frac{\partial(Y_3 \pm \lambda/2)}{\partial X_j} v_i \right] \\ \delta_{ij} + \frac{\partial u_{Gi}}{\partial X_j} &= F_{ij} + \frac{1}{\lambda} \left[(Y_3 \pm \lambda/2) \frac{\partial v_i}{\partial Y_k} \frac{\partial Y_k}{\partial X_j} + N_j v_i \right] \\ \delta_{ij} + \frac{\partial u_{Gi}}{\partial X_j} &= F_{ij} + \frac{1}{\lambda} \left[(Y_3 \pm \lambda/2) \begin{pmatrix} \frac{\partial v_{Y_1}}{\partial Y_1} & \frac{\partial v_{Y_1}}{\partial Y_2} & \frac{\partial v_{Y_1}}{\partial Y_3} \\ \frac{\partial v_{Y_2}}{\partial Y_1} & \frac{\partial v_{Y_2}}{\partial Y_2} & \frac{\partial v_{Y_2}}{\partial Y_3} \\ \frac{\partial v_{Y_3}}{\partial Y_1} & \frac{\partial v_{Y_3}}{\partial Y_2} & \frac{\partial v_{Y_3}}{\partial Y_3} \end{pmatrix} \begin{pmatrix} \frac{\partial Y_1}{\partial X_1} & \frac{\partial Y_1}{\partial X_2} & \frac{\partial Y_1}{\partial X_3} \\ \frac{\partial Y_2}{\partial X_1} & \frac{\partial Y_2}{\partial X_2} & \frac{\partial Y_2}{\partial X_3} \\ \frac{\partial Y_3}{\partial X_1} & \frac{\partial Y_3}{\partial X_2} & \frac{\partial Y_3}{\partial X_3} \end{pmatrix} + N_j v_i \right] \end{aligned}$$

$$\begin{aligned}
\delta_{ij} + \frac{\partial u_{Gi}}{\partial X_j} &= F_{ij} + \frac{1}{\lambda} (Y_3 \pm \lambda/2) \left[\begin{pmatrix} \frac{\partial v_{Y_1}}{\partial Y_1} & \frac{\partial v_{Y_1}}{\partial Y_2} & \frac{\partial v_{Y_2}}{\partial Y_1} & \frac{\partial v_{Y_2}}{\partial Y_2} & \frac{\partial v_{Y_3}}{\partial Y_1} & \frac{\partial v_{Y_3}}{\partial Y_2} \end{pmatrix} \begin{pmatrix} 0 \\ 0 \\ 0 \end{pmatrix} \begin{pmatrix} (\mathbf{M}_1)_1 & (\mathbf{M}_1)_2 & (\mathbf{M}_1)_3 \\ (\mathbf{M}_2)_1 & (\mathbf{M}_2)_2 & (\mathbf{M}_2)_3 \\ (\mathbf{N})_1 & (\mathbf{N})_2 & (\mathbf{N})_3 \end{pmatrix} + N_j v_i \right] \\
\delta_{ij} + \frac{\partial u_{Gi}}{\partial X_j} &= F_{ij} + \frac{1}{\lambda} (Y_3 \pm \lambda/2) \left[\begin{pmatrix} \frac{\partial v_{Y_1}}{\partial Y_1} & \frac{\partial v_{Y_1}}{\partial Y_2} & \frac{\partial v_{Y_2}}{\partial Y_1} & \frac{\partial v_{Y_2}}{\partial Y_2} & \frac{\partial v_{Y_3}}{\partial Y_1} & \frac{\partial v_{Y_3}}{\partial Y_2} \end{pmatrix} \begin{pmatrix} \frac{\partial v_{Y_1}}{\partial Y_1} (\mathbf{M}_1)_1 + \frac{\partial v_{Y_2}}{\partial Y_1} (\mathbf{M}_2)_1 \\ \frac{\partial v_{Y_1}}{\partial Y_2} (\mathbf{M}_1)_2 + \frac{\partial v_{Y_2}}{\partial Y_2} (\mathbf{M}_2)_2 \\ \frac{\partial v_{Y_2}}{\partial Y_1} (\mathbf{M}_1)_1 + \frac{\partial v_{Y_3}}{\partial Y_1} (\mathbf{M}_2)_1 \\ \frac{\partial v_{Y_2}}{\partial Y_2} (\mathbf{M}_1)_2 + \frac{\partial v_{Y_3}}{\partial Y_2} (\mathbf{M}_2)_2 \\ \frac{\partial v_{Y_3}}{\partial Y_1} (\mathbf{M}_1)_3 + \frac{\partial v_{Y_3}}{\partial Y_2} (\mathbf{M}_2)_3 \end{pmatrix} + N_j v_i \right] \\
\delta_{ij} + \frac{\partial u_{Gi}}{\partial X_j} &= F_{ij} + \frac{1}{\lambda} (Y_3 \pm \lambda/2) \left[\begin{pmatrix} \frac{\partial v_{Y_1}}{\partial Y_1} & \frac{\partial v_{Y_1}}{\partial Y_2} & \frac{\partial v_{Y_2}}{\partial Y_1} & \frac{\partial v_{Y_2}}{\partial Y_2} & \frac{\partial v_{Y_3}}{\partial Y_1} & \frac{\partial v_{Y_3}}{\partial Y_2} \end{pmatrix} \begin{pmatrix} \frac{\partial v_{Y_1}}{\partial Y_1} (\mathbf{M}_1)_1 \\ \frac{\partial v_{Y_1}}{\partial Y_2} (\mathbf{M}_1)_2 \\ \frac{\partial v_{Y_2}}{\partial Y_1} (\mathbf{M}_1)_3 \\ \frac{\partial v_{Y_2}}{\partial Y_2} (\mathbf{M}_1)_3 \\ \frac{\partial v_{Y_3}}{\partial Y_1} (\mathbf{M}_1)_3 \\ \frac{\partial v_{Y_3}}{\partial Y_2} (\mathbf{M}_1)_3 \end{pmatrix} + \begin{pmatrix} \frac{\partial v_{Y_1}}{\partial Y_2} (\mathbf{M}_2)_1 \\ \frac{\partial v_{Y_2}}{\partial Y_1} (\mathbf{M}_2)_2 \\ \frac{\partial v_{Y_2}}{\partial Y_2} (\mathbf{M}_2)_3 \\ \frac{\partial v_{Y_3}}{\partial Y_2} (\mathbf{M}_2)_3 \end{pmatrix} + N_j v_i \right]
\end{aligned}$$

$$\mathbf{F}_G = \mathbf{1} + \frac{\partial \mathbf{u}_G}{\partial \mathbf{X}} = \begin{cases} \mathbf{F} + \frac{1}{\lambda} \mathbf{v} \otimes \mathbf{N}^- + \frac{(Y_3 + \lambda/2)}{\lambda} \left[\frac{\partial \mathbf{v}}{\partial Y_1} \otimes \mathbf{M}_1 + \frac{\partial \mathbf{v}}{\partial Y_2} \otimes \mathbf{M}_2 \right] & -\lambda/2 \leq Y_3 \leq 0^- \\ \mathbf{F} + \frac{1}{\lambda} \mathbf{v} \otimes \mathbf{N}^- + \frac{(Y_3 - \lambda/2)}{\lambda} \left[\frac{\partial \mathbf{v}}{\partial Y_1} \otimes \mathbf{M}_1 + \frac{\partial \mathbf{v}}{\partial Y_2} \otimes \mathbf{M}_2 \right] & 0^+ \leq Y_3 \leq \lambda/2 \\ \mathbf{F} & \text{otherwise.} \end{cases} \quad (2.7)$$

The first term in equation (2.7) is simply the deformation gradient taken from the continuum material inside Λ . For points that lay on the separation surface (i.e. $\mathbf{X} \in \Gamma_0$), equation (2.2) may be used to define the gradient. The second term in equation 2.7 normalizes the gap vector \mathbf{v} by the length scale (i.e., layer thickness) and applies this vector in the direction \mathbf{N} . The third term presents the gradient of the gap vector \mathbf{v} in the tangent directions of the separation surface. (By definition, the gap vector does not vary in the direction of the separation surface normal). Inclusion of the gradient of the gap vector greatly complicates the formulation as is discussed in section 2.2.3.1. Furthermore, the gradient of the gap vector is very small for surfaces near the front of the separation surface (i.e., near the crack tip the separation surfaces are nearly parallel), while it may attain larger values away from the front. Since the main region of concern is near the crack tip, the gap gradient term in equation (2.7) is removed, and the remaining two terms are used to define the bridging tensor (\mathbf{G}):

$$\mathbf{G} = \begin{cases} \mathbf{F} + \frac{1}{\lambda} \mathbf{v} \otimes \mathbf{N}^- & \mathbf{X} \in \Lambda_0 \\ \mathbf{F} & \mathbf{X} \notin \Lambda_0. \end{cases} \quad (2.8)$$

To illustrate the ramifications of equation (2.8), let us first examine how \mathbf{G} transforms a material line element lying along the direction \mathbf{a}_0 in the reference configuration.

Specifically, consider the transformation from the reference configuration to the current configuration with the vector components expressed in terms of the orthonormal triad $\{\mathbf{N}$,

$\mathbf{M}_1, \mathbf{M}_2\}$ described previously. Prior to the onset of separation ($\Phi < \Phi_1$), conventional continuum kinematics fully applies (e.g., $\mathbf{G}\mathbf{a}_0 = \mathbf{F}\mathbf{a}_0 = \mathbf{a}$). Once the rupture process is initiated ($\Phi > \Phi_1$), the vectors components $\{\mathbf{N}, \mathbf{M}_1, \mathbf{M}_2\}$ are treated differently.

Specifically, if $\mathbf{a}_0 = \mathbf{M}_1$ or \mathbf{M}_2 (i.e., \mathbf{a}_0 lies in the rupture plane) then the material line element is transformed by \mathbf{G} in an identical manner as if it were transformed by \mathbf{F} .

However, if $\mathbf{a}_0 = \mathbf{N}$ then the transformation of \mathbf{a}_0 is now described by the continuum deformation gradient plus the length scale normalized gap vector (i.e., $\mathbf{G}\mathbf{N} = \mathbf{F}\mathbf{N} + \frac{\mathbf{v}}{\lambda}$).

2.2.2.2 Surface Based Formulation

The Surface Based Formulation (SBF) assumes that only the material points $\mathbf{X} \in \Gamma_0$ are subject to enriched kinematics for the purposes of evaluating the constitutive response of the rupturing material. Prior to postulating a bridging tensor, first consider the average of the deformation gradients at $\mathbf{X}^{\pm} \in \Gamma_0^{\pm}$:

$$\bar{\mathbf{F}} = \frac{1}{2}(\mathbf{F}^+ + \mathbf{F}^-). \quad (2.9)$$

Prior to initiation of the rupture process, the deformation gradient will generally be continuous across Γ_0 , thus $\bar{\mathbf{F}} = \mathbf{F}^+ = \mathbf{F}^-$ and standard continuum mechanics fully applies.

When \mathbf{v} attains a non-zero magnitude (i.e., the separation process begins), the standard deformation gradient is undefined on Γ_0 . To construct a model for the behavior of rupturing material at points $\mathbf{X} \in \Gamma_0$, the effects of the displacement jump across Γ_0 must be accounted for. For this task the bridging tensor is proposed as:

$$\mathbf{G} = \begin{cases} \bar{\mathbf{F}} & \text{if } \Phi \leq \Phi_1 \\ \bar{\mathbf{F}}(\mathbf{I} - \mathbf{N} \otimes \mathbf{N}) + \left(\mathbf{w} + \frac{\mathbf{v}}{\lambda}\right) \otimes \mathbf{N} & \text{if } \Phi > \Phi_1. \end{cases} \quad (2.10)$$

As done in the previous section, consider how G acts on an arbitrary vector (\mathbf{a}_0). If $\mathbf{a}_0 = \mathbf{M}_1$ or \mathbf{M}_2 (i.e., \mathbf{a}_0 lies in the rupture plane) then the material line element is transformed by $\bar{\mathbf{F}}$ ($\mathbf{G}\mathbf{M}_\alpha = \bar{\mathbf{F}}\mathbf{M}_\alpha$). However, if $\mathbf{a}_0 = \mathbf{N}$ then the transformation of \mathbf{a}_0 is now described by the kinematic vector (\mathbf{w}), plus the addition of the gap vector normalized by a length scale (i.e., $\mathbf{G}\mathbf{N} = \mathbf{w} + \frac{\mathbf{v}}{\lambda}$).

Different choices of the kinematic vector \mathbf{w} may be specified from a variety of readily available kinematic quantities. The choice \mathbf{w} will determine what specific features (e.g., reversibility, time continuity) the CCF implementation will possess. A strict requirement for the selection of \mathbf{w} is that it must not remove the length-scale (λ) from the problem. One logical choice of \mathbf{w} is $\bar{\mathbf{F}}\mathbf{N}$, as this provides an appealing continuity of state prior to and immediately after separation. However, this choice results in the appearance of various numerical instabilities; thus a more complex choice is required. Toward this end, consider two material points ($\mathbf{Z}^{+,-}$) which are a distance (δZ) away from Γ_0 along the normal \mathbf{N} , as shown in Figure 2.4. Let the vector between the two points be defined as:

$$\delta\mathbf{Z} = \mathbf{Z}^+ - \mathbf{Z}^-. \quad (2.12)$$

The vector \mathbf{w} is then specified to be:

$$\mathbf{w} = \frac{\delta\mathbf{Z} - (\mathbf{v} \cdot \mathbf{n}_{dz})\mathbf{n}_{dz}}{|\delta\mathbf{Z}|},$$

where :

$$\mathbf{n}_{dz} = \frac{\delta\mathbf{Z}}{|\delta\mathbf{Z}|}. \quad (2.13)$$

If $\mathbf{v}=\mathbf{0}$, the expression for \mathbf{w} approaches $\bar{\mathbf{F}}\mathbf{N}$ in the limit as the distance δZ approaches zero. The major reason for using equation (2.13) for \mathbf{w} rather than $\bar{\mathbf{F}}\mathbf{N}$ lays in the relation

between \mathbf{v} and $\bar{\mathbf{F}}\mathbf{N}$. In the course of numerical calculations, the two vectors \mathbf{v}/λ and $\bar{\mathbf{F}}\mathbf{N}$ may counteract each other. This will inevitably lead to non-physical oscillations where the components of the two vectors are substantially out of phase. In contrast, the expression for \mathbf{w} in equation (2.13) will typically be much closer to the phase of \mathbf{v} , especially if δZ is very small. Figure 2.5 illustrates how this choice of \mathbf{w} may differ from $\bar{\mathbf{F}}\mathbf{N}$.

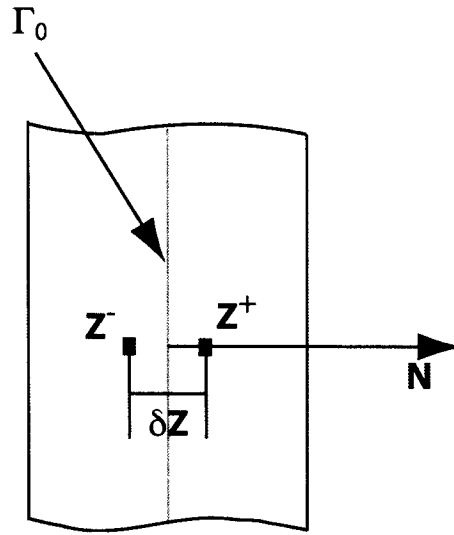


Figure 2.4: Internal Points from Γ for Surface Based Formulation

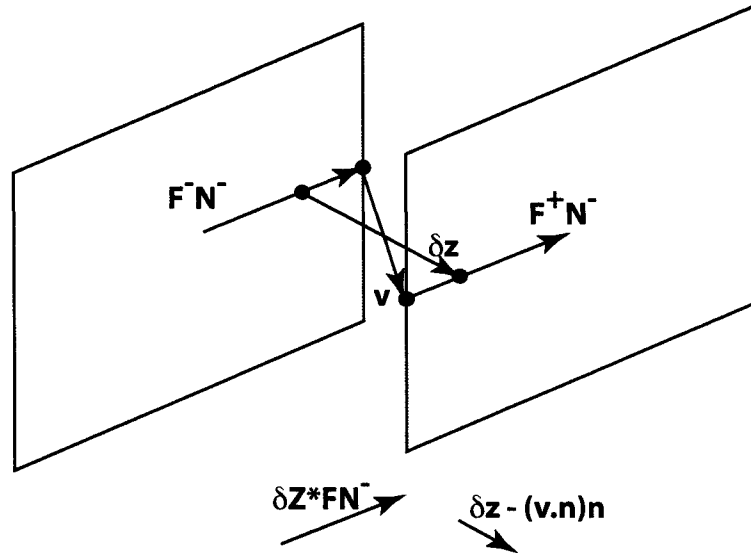


Figure 2.5: Vector δz and $\bar{F}N$ Comparison for Surface Based Formulation

2.2.2.3 Enriched Kinematics Features

In the previous two sections, enriched kinematics have been proposed for both the finite thickness layer approach and the surface based approach culminating in equations (2.8) and (2.10, 13). While the two formulations differ significantly, discussion of the general characteristics of the resulting bridging tensors \mathbf{G} may be done together.

As \mathbf{G} is a kinematic quantity that is used to replace the standard continuum gradient for purposes of constitutive evaluations, it is appropriate to consider how \mathbf{G} will evolve throughout two specific loading situations. The first situation to consider is the transition from a standard boundary value problem ($\Phi(\mathbf{X}) < \Phi_1 \quad \forall \mathbf{X} \in B_0$) to a surface separation problem ($\exists \mathbf{X} \in B_0 \ni \Phi(\mathbf{X}) > \Phi_1$). Let t_s be the time at which the separation process begins ($\Phi = \Phi_1$), and $t_s^{+,-}$ bound an infinitesimal increment (δt_s) in time surrounding t_s . For any material that relies on \mathbf{G} to generate kinematic input for a constitutive update, a finite

change in \mathbf{G} over δt_s will potentially result in a finite change in the stress state within the material. This change of the stress state will lead to non-physical stress waves being generated at the point of separation. For this reason, it is desirable that this transition be such that no discontinuity occurs in \mathbf{G} . Satisfaction of this condition results in what may be referred to as *time-continuity*. In this case we use the term time-continuity to imply that there is no discernible change in relevant quantities over δt_s . For example, if \mathbf{G} is continuous over δt_s and the stresses are applied between the two configurations appropriately (i.e., the effects of the stress state on the body immediately after separation mimics the effects of the stress state on the body preceding separation), then the regions surrounding the separation surface will not experience a change in state over δt_s . If the state of the material surrounding the separation surface does not change, then the acceleration field remains continuous over δt_s . A continuous acceleration field indicates that there are no abrupt changes in the displacement field over δt_s , and subsequently \mathbf{G} itself, as a result of the separation. Thus the continuity of \mathbf{G} encourages a response in the surrounding material region that, in turn, will tend to promote a smooth transition of \mathbf{G} .

Another important situation to consider is when a loaded body undergoing the separation process is unloaded, or loading is reversed. An elementary consideration of the expression for \mathbf{G} reveals that if \mathbf{F} evolves such that there is zero stress in the body (i.e., the body is fully unloaded), the only means by which \mathbf{G} may differ from \mathbf{F} is through a non-zero gap vector. Thus \mathbf{v} may or may not revert back to zero, depending on the constitutive behavior of the material. Whatever the specific constitutive behaviors may

be, equilibrium will enforce that the stress state in Λ return to zero as well, and the equilibrium quantities of \mathbf{F} and \mathbf{v} will be achieved.

Based on the preceding two discussions, we make the statement that \mathbf{G} provides a length-scale equipped, reversible, time-continuous expression that describes the kinematics in Λ . Thus \mathbf{G} is an acceptable candidate by which to generate the kinematic input for use in the state update of the separating material via the bulk constitutive law.

2.2.3 Cohesive Stresses

Once appropriate kinematics are defined as input to the constitutive relation, a method by which the rupturing material influences the body must be described. Specifically, the stress state of the rupturing material, which will be referred to as the *cohesive stress*, must be allowed to influence equilibrium of the body in some manner. In conventional cohesive zone models, the application of stress is done via a “cohesive traction” applied to the separation surfaces. As stated previously this “cohesive traction” is derived from a “traction-separation law” which is separate from the standard constitutive relations used to describe the bulk material. In contrast, the CCF has a fully 3-dimensional material state by which to generate a *cohesive stress*. This cohesive stress may be expressed as the standard Cauchy Stress (\mathbf{T}) multiplied by a scalar function (r):

$$\mathbf{T}_c = r(s) \cdot \mathbf{T}. \quad (2.15)$$

The scalar function $r(s)$ is referred to as the *stress-reduction factor*, and is defined as:

$$r(s) = \begin{cases} 1 & s = 0 \\ f(s) & 0 < s < 1 \\ 0 & s = 1 \end{cases} \quad (2.16)$$

$$\frac{df(s)}{ds} < 0.$$

The appropriateness of a stress-reduction factor is evident when considering the origin of the Cauchy Stress on which it acts. The material state, and thus the Cauchy Stress, is derived from constitutive relations driven by the enriched kinematics specified in equations (2.8, 2.10). While the introduction of the Rupture Function (Φ) and a non-zero value of \mathbf{v} in \mathbf{G} may imply that the material may not be fully connected, this implication is lost when \mathbf{G} is used in the same manner as a standard continuum based gradient to update a material state. No information pertaining to the separation of the material is passed to the constitutive model; therefore the stresses generated by the constitutive model assume that the material is still fully connected from a macroscopic point of view. If the constitutive model does not provide means for a stress reduction based on its own "damage" parameters, then a method for reducing the stresses must be specified outside the scope of the constitutive relation. For constitutive models with an intrinsic stress reduction, such as the Gurson void growth model [32, 33], the stress reduction factor may be defined near unity until the separation coefficient is itself near unity.

2.2.3.1 Finite Thickness Layer Assumption

It is crucial to observe that the cohesive stresses (\mathbf{T}_c) that result from the modified constitutive response in the layer Λ must be applied in a manner consistent with the assumed configuration of Λ . Specifically, the discontinuity that bisects Λ implies the stresses in $\Lambda^{+,-}$ must be accompanied by cohesive tractions (denoted by Piola tractions $\mathbf{p}^{+,-}$) that are applied to the separating surfaces $\Gamma^{+,-}$. Furthermore, these tractions must be consistent, in

a certain sense, with the cohesive stresses in $\Lambda^{+,-}$. This can be understood by considering a “filament” \mathcal{L} of material lying normal to Γ (i.e., along \mathbf{N}) and described in the reference configuration, by an infinitesimal area $dA \subseteq \Gamma$ and $-\frac{\lambda}{2} < Y_3 < \frac{\lambda}{2}$. In the first of the two scenarios, the filament undergoes separation at its middle, subject to the cohesive tractions, which tend to hold the halves together. The rate of work on \mathcal{L} per unit area Γ ($\dot{E}_{\mathcal{L}}$) in a quasistatic process is:

$$\dot{E}_{\mathcal{L}} = \int_{-\lambda/2}^{0-} \left((P_c)_{ij} \dot{F}_{ij} \right) dY_3 + \int_{0+}^{\lambda/2} \left((P_c)_{ij} \dot{F}_{ij} \right) dY_3 - (p_i^+ \dot{u}_i^+ + p_i^- \dot{u}_i^-),$$

where :

$$\mathbf{P}_c = \mathbf{T}_c \mathbf{F}^{-T} \det(\mathbf{F}).$$

Assume for a moment that $\mathbf{p}^{+,-} = \mathbf{P}_c \mathbf{N}^{+,-}$, where \mathbf{P}_c is taken on the surface of Γ . Now consider $\mathbf{p}^{+,-}$ were specified to be zero, then \mathbf{G} , on which \mathbf{P}_c is based and which involves the gap vector \mathbf{v} , would be obliged to accommodate the condition $\mathbf{P}_c \mathbf{N} = \mathbf{0}$ at $Y_3 = 0$. Specifically, if \mathbf{v}/λ is increasing – i.e., if the surfaces are separating – then momentum balance implies \mathbf{F} must be such that $\mathbf{F}\mathbf{N}$ is decreasing at an even faster rate. This contraction in the normal direction is, in turn, accompanied by expansion in the plane of Γ . Ultimately, this expansion opposes the in-plane stress components, leading to a negative rate of work done – i.e., and unphysical energy source.

Now consider a second scenario, in which the filament \mathcal{L} remains intact, but actually deforms with the deformation gradient equal to the bridging tensor \mathbf{G} . In this case, the rate of work done on \mathcal{L} per unit area Γ ($\dot{E}_{\mathcal{L}_2}$) in a quasistatic process is:

$$\dot{E}_{\mathcal{L}_2} = \int_{-\lambda/2}^{\lambda/2} (P_c)_{ik} \dot{G}_{ik} dY_3. \quad (2.18)$$

In this case, it is obvious that no unphysical energy source arises, as the cohesive stress \mathbf{P}_c is doing work through the deformation rate that actually produces the stress. Inserting equation 2.8 into this relation yields:

$$\begin{aligned} \dot{E}_{\mathcal{L}2} &= \int_{-\lambda/2}^{\lambda/2} \left((P_c)_{ij} \dot{F}_{ij} \right) dY_3 - \bar{P}_{ij} (\dot{u}_i^+ N_j^+ + \dot{u}_i^- N_j^-) \\ \text{where } \bar{P}_{ij} &= \frac{1}{\lambda} \int_{-\lambda/2}^{\lambda/2} (P_c)_{ij} dY_3. \end{aligned} \quad (2.19)$$

Comparing (2.17) to (2.19) suggests that the cohesive traction can be defined, such that no energy source is created, as:

$$p_i^{+-} = \bar{P}_{ij} N_j^{+-}. \quad (2.20)$$

2.2.3.2 Surface Based Approach

Since the surface based approach assumes that the rupturing material exists only on a surface, the application of a cohesive traction alone to Γ is an appropriate means by which to apply the cohesive stress. A cohesive traction suited for this task may be defined as:

$$p_i^{+-} = P_{ij} N_j^{+-}. \quad (2.21)$$

In equation (2.21), \mathbf{P} is the first Piola-Kirchoff stress of the rupturing material, and is defined on Γ . This approach resembles the standard cohesive zone idea in that a cohesive traction is the only means by which the rupturing material influences the equations of motion. However, the use of enriched kinematics to update the material state on Γ , and use of equation (2.21) rather than some direct relation between the cohesive traction and the gap vector (as is done in conventional cohesive zone models), complicates the situation dramatically. In particular, the components of \mathbf{G} that act in the \mathbf{M} -directions

introduce the ability for the rupturing material to act as an energy source. This is obviously non-physical, as the rupture process should always result in a net dissipation of energy. Furthermore, the surface based approach essentially assumes that the rupturing material has no volume, which implies that energy may not be stored via the cohesive tractions. This leads to the conclusion that a cohesive traction couple must not do positive work on the system point wise. This requirement may be expressed as:

$$\mathbf{p}^+ \cdot \dot{\mathbf{u}}^+ + \mathbf{p}^- \cdot \dot{\mathbf{u}}^- \leq 0 \quad \forall X \in \Gamma_0. \quad (2.22)$$

This condition is referred to as an *energy limiter*. In order to satisfy this condition, the cohesive tractions calculated in equation (2.21) should be modified such that either the displacement rate is sufficiently altered as to satisfy equation (2.22), or the magnitude of the traction is equal to zero. In connection with the second possibility, the scaling factor (c) is applied while recognizing that the cohesive tractions are equal and opposite:

$$\begin{aligned} \mathbf{p}_{sc} &= p_{sc} \mathbf{n}_p = c_s \mathbf{p}^+ = -c_s \mathbf{p}^-, \\ \text{where } 0 &\leq c_s \leq 1. \end{aligned} \quad (2.23)$$

The resulting modification of equation (2.22) using \mathbf{p}_{sc} is

$$\begin{aligned} \mathbf{p}_{sc} \cdot (\dot{\mathbf{u}}^+ - \dot{\mathbf{u}}^-) &\leq 0 \\ \mathbf{p}_{sc} \cdot \dot{\mathbf{v}} &\leq 0. \end{aligned} \quad (2.24)$$

It should be borne in mind that a reduction in \mathbf{p} through use of the scaling factor (c_s), will directly affect the velocity at $X \in \Gamma_0$. Furthermore, if equation (2.24) is violated, it is implied that a reduction in \mathbf{p} will result in a reduction in the rate of the gap displacement. A simple one-dimensional example of how this reduction takes place is illustrated in Figure 2.6. The first illustration in this figure shows a situation where the cohesive tractions and displacement rate vectors are in opposite directions, thus satisfying equation

(2.24). The second illustration shows a situation where the cohesive tractions and displacement rate vectors are in the same direction, thus violating the condition in (2.24). The subsequent reduction in the cohesive tractions takes place, which results in either the magnitude of the traction or the displacement rates equaling zero, thus satisfying equation (2.24).

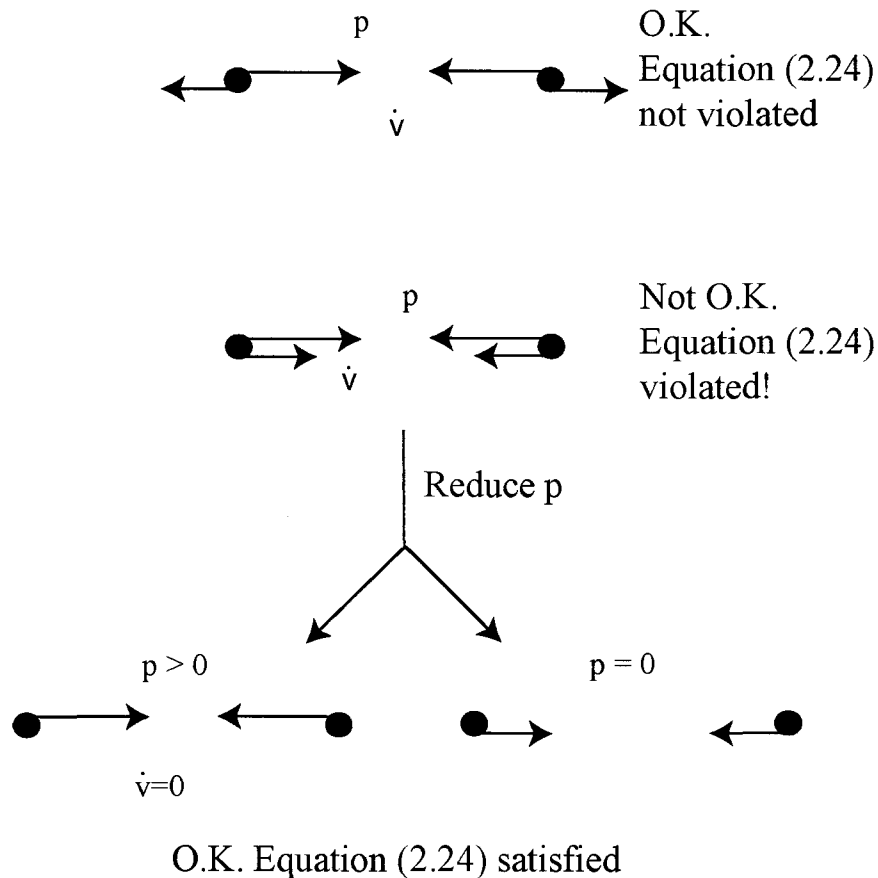


Figure 2.6: Energy Limiter Scenarios Illustrated

2.3 Summary

In this chapter the Cohesive Continuum Framework for the modeling of surface generation problems has been explained in detail. The kinematics required to describe the problem have been defined for two possible assumed configurations of the rupturing material. The first proposed configuration assumes that the rupture process occurs over a

finite-thickness layer of material, while the second proposed configuration assumes that the rupture process occurs on a surface. A so-called rupture function has been defined to provide a quantitative measure of the degree of rupture in the material. Enriched kinematics suitable for generating input into a standard constitutive relation has been defined for both approaches. The enriched kinematics have been presented in the form of a so-called bridging tensor that takes the place of the deformation gradient for the purposes of a constitutive evaluation. The bridging tensors are expressed in terms of the surrounding bulk deformation gradient, the gap vector, a length scale, and a surface normal. Once a constitutive update takes place using these kinematics, the stress state of the rupturing material (cohesive stress) is applied to the body in a manner consistent with the assumed configuration of the rupturing material (i.e., surface based or finite thickness layer).

3 Finite Element Method Implementation

In order to evaluate the performance of the Cohesive Continuum Framework, both the finite thickness and surface based formulations have been implemented in a time-explicit 3D finite element structural dynamics code. The CCF has been implemented in a standard finite element procedure, as the finite element method constitutes a convenient platform for testing the CCF. The code, which is named CCFEM, has been constructed for the sole purposes of developing the CCF. CCFEM is written in C++ using language features such as class inheritance, class templates, and the standard template library. CCFEM has been successfully compiled using the Gnu c++ compiler (g++ 3.3, 4.0) as well as the Intel c++ compiler (icpc 8.0). The development platform for CCFEM is a combination of Metroworks Codewarrior© running on Mac OS 10.4, in tandem with the g++ compiler on Mac OS. The code is then ported to both g++ and icpc on Redhat Linux 9.

3.1 *Finite Element Preliminaries*

Prior to describing the implementation of the Cohesive Continuum Framework, the specifics of the finite element method used here are described. To this end, the derivation of the FEM equations of motion, as well as specific features of the FEM implementation are set forth.

3.1.1 FEM Equations of Motion

Spatial discretization of balance of momentum via the weak form is discussed in this section, whereas its subsequent temporal discretization is covered in the next. The strong form of equilibrium in the reference configuration may be expressed as:

$$P_{ij,j} - \rho_0 a_i = 0 \quad \forall \mathbf{X} \in B_0 \quad (3.1)$$

In equation (3.1), \mathbf{P} is the first piola-Kirchhoff stress, ρ_0 is the reference density of the material, and B_0 is the body in its reference configuration. The boundary of B is defined as ∂B , with the further specification that $\partial_u B$ represents the portion of the boundary subject to kinematic boundary conditions, and $\partial_t B$ the portion of the boundary subject to traction boundary conditions. Since any free boundary surface may be classified as belonging to $\partial_t B$ with an applied traction equal to zero, it is appropriate to state that $\partial B = \partial_t B \cup \partial_u B$. A vector test function \mathbf{v} , where $\mathbf{v} \in \{\mathbf{v} \mid \mathbf{v} \in C^0(B), \mathbf{v} = \mathbf{0} \text{ on } \partial_u B\}$, is dotted with the strong form and the result is integrated over the volume of the body (B):

$$\begin{aligned} \int_{B_0} v_i \rho_0 a_i dV &= \int_{B_0} v_i P_{ij,j} dV \Rightarrow \\ \int_{B_0} v_i \rho_0 a_i dV &= \int_{B_0} \left[(v_i P_{ij})_j - v_{i,j} P_{ij} \right] dV \quad \forall \{\mathbf{v} \mid \mathbf{v} \in C^0(B), \mathbf{v} = \mathbf{0} \text{ on } \partial_u B\}. \end{aligned} \quad (3.2)$$

Application of the divergence theorem to the first term on the right hand side of 3.2 yields:

$$\int_{B_0} v_i \rho_0 a_i dV = \int_{\partial_t B_0} v_i \bar{p}_i dA - \int_{B_0} v_{i,j} P_{ij} dV \quad \forall \{\mathbf{v} \mid \mathbf{v} \in C^0(B), \mathbf{v} = \mathbf{0} \text{ on } \partial_u B\}. \quad (3.3)$$

In equation (3.3), $\bar{\mathbf{p}}$ is the first Piola traction vector applied to the boundary. The solution to the weak form (3.3) is now approximated via the Galerkin method as follows. The vector test function \mathbf{v} , as well as the acceleration \mathbf{a} are approximated in terms of FEM shape functions:

$$\begin{aligned} \mathbf{v} &= \sum_{a \in \eta_0} \mathbf{v}_a \Phi_a \\ \mathbf{a} &= \sum_{b \in \eta_0} \mathbf{a}_b \Phi_b + \sum_{b \in \eta_u} \mathbf{a}_b \Phi_b. \end{aligned} \quad (3.4)$$

Here, η_u =set of nodes subject to kinematic boundary conditions, and $\eta_0=\{1,2,3,\dots,N\}$, where N is the number of free nodes. In other words η_0 is the set of “free” nodes.

Substituting equation (3.4) into equation (3.3) yields:

$$\sum_{a=1}^N v_{ia} \left(\sum_{b=1}^N \int_{B_0} \Phi_a \Phi_b \rho_0 a_{bi} dV - \int_{\partial_i B_0} \Phi_a \bar{p}_i dA + \int_{B_0} \Phi_{a,j} P_{ij} dV \right) = 0. \quad (3.5)$$

Since the relation in equation (3.5) must hold $\forall v_{ia}$, it must also be true that:

$$\sum_{b=1}^N \int_{B_0} \Phi_a \Phi_b \rho_0 a_{bi} dV - \int_{\partial_i B_0} \Phi_a \bar{p}_i dA + \int_{B_0} \Phi_{a,j} P_{ij} dV = 0, a \in \eta_0. \quad (3.6)$$

This expression may be rewritten such that it applies at a specific point in time:

$$\sum_{b=1}^N \int_{B_0} \Phi_a \Phi_b \rho_0 a_{bi}^{n+1} dV = \int_{\partial_i B_0} \Phi_a \bar{p}_i^{n+1} dA - \int_{B_0} \Phi_{a,j} P_{ij}^{n+1} dV, a \in \eta_0. \quad (3.7)$$

Equation (3.7) provides the discrete equation of motion for the finite element method. In the setting of explicit FEM, this relation is used to solve for the end step accelerations (\mathbf{a}^{n+1}) given the end step stress state \mathbf{P}^{n+1} .

3.1.2 Time Stepping

For the purposes of this research effort, the explicit Newmark method (second order accurate) is used to advance the solution to equation (3.7) in time. This method first requires that the incremental nodal displacements be calculated over the time step. Using the beginning step velocity ($\dot{\mathbf{u}}^n$) and acceleration (\mathbf{a}^n), the incremental nodal displacement is expressed as:

$$\hat{\mathbf{u}} = \mathbf{u}^{n+1} - \mathbf{u}^n = \dot{\mathbf{u}}^n \cdot \Delta t + \frac{1}{2} \mathbf{a}^n \cdot \Delta t^2. \quad (3.8)$$

This relation provides the increment over the time step ($\hat{\mathbf{u}}$) as well as the total displacement from the reference configuration (\mathbf{u}^{n+1})-(the beginning step displacement

(\mathbf{u}^n) is already known). Using these displacements, the stretch and rotation increments are calculated at every integration point using the incremental kinematics algorithm presented by Rashid [34]. Next, the constitutive update is performed, and incremental rotations are applied to bring the material state (Q) to t^{n+1} . Given that the stresses at t^{n+1} are now known, the appropriate nodal accelerations at t^{n+1} may be calculated through equation (3.7). It bears stating that the left hand side of equation (3.7) must be integrated using nodal integration points in order for the overall algorithm to be explicit. If this were not the case, then the solution for \mathbf{a}^{n+1} would require solving a system of linear equations. Once \mathbf{a}^{n+1} is known, the velocity at t^{n+1} is calculated using:

$$\dot{\mathbf{u}}^{n+1} = \dot{\mathbf{u}}^n + \frac{1}{2}(\mathbf{a}^n + \mathbf{a}^{n+1}) \cdot \Delta t. \quad (3.9)$$

At this point, all end step quantities are known (\mathbf{u}^{n+1} , $\dot{\mathbf{u}}^{n+1}$, \mathbf{a}^{n+1} , Q^{n+1}) and the process is repeated from the beginning to obtain the solution for the following increment in time.

For numerical stability, explicit Newmark requires that the time step does not exceed some limiting value (Δt_{\max}). A guideline for the calculation of conservative estimates to Δt_{\max} is given by Flanagan and Belytschko[35]. They recommended that Δt_{\max} be estimated by:

$$\Delta t_{\max} \leq l \sqrt{\frac{\rho}{3\lambda + 6\mu}}, \quad (3.10)$$

where l is the minimum element dimension, ρ is the material density, λ is Lamé's constant, and μ is the shear modulus.

3.1.3 Element Formulation

This implementation of the finite element method uses standard 8-node hexahedral solid elements with tri-linear shape functions. The parent element and nodal coordinates are shown in figure 3.1.

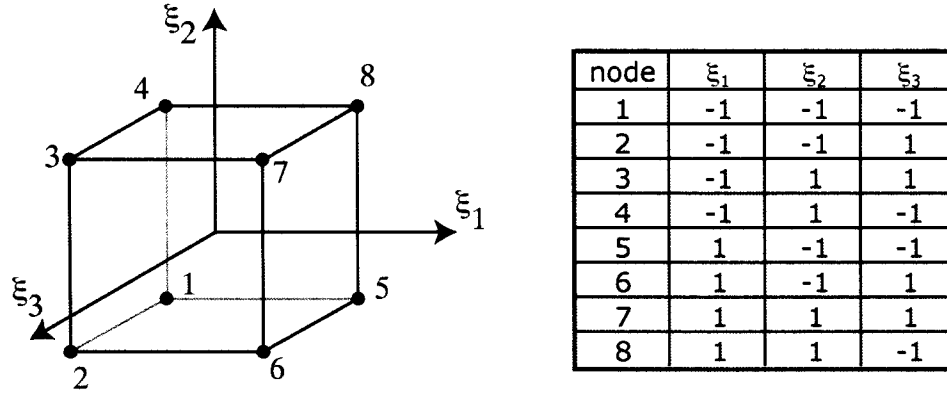


Figure 3.1: Parent Element and Nodal Coordinates

If (ξ_1, ξ_2, ξ_3) are coordinates in the parent domain, and $(\xi_{a1}, \xi_{a2}, \xi_{a3})$ indicate the coordinates of node “a” in the parent domain, then the standard tri-linear shape functions associated with the parent element are written as:

$$\Phi_a(\xi_1, \xi_2, \xi_3) = \frac{1}{8}(1 + \xi_1 \xi_{a1})(1 + \xi_2 \xi_{a2})(1 + \xi_3 \xi_{a3}). \quad (3.10)$$

The volume integrals in equation (3.7) must be evaluated using numerical integration. The stress term is integrated using 8 integration points on the interior of the element, while the acceleration term is integrated using 8 integration points located at the nodes. Following standard practice, a 2x2x2 Gaussian quadrature rule is used for the stress term so that the integration points are located at the coordinates outlined in Figure 3.1, with the coordinate vector being scaled by a factor of $1/\sqrt{3}$. The acceleration term is integrated using nodal integration points to ensure that the method is indeed explicit. Following the

application of this numerical integration scheme, the FEM equation of motion may be written as:

$$\sum_{k=1}^{nelem} (\rho_0 a_{ai}^{n+1} |J_a|) = \sum_{m=1}^{ntbc} \sum_{b=1}^4 \left(\left(\Phi_a \bar{P}_i^{n+1} |J_a| J_a^{-T} N \right) \right)_b - \sum_{k=1}^{nelem} \sum_{b=1}^8 \left(\left(\Phi_{a,j} P_{ij}^{n+1} \right) \right)_b |J_b|, \quad (3.11)$$

where $J_a = \frac{\partial \mathbf{X}}{\partial \boldsymbol{\xi}} \bigg|_{\boldsymbol{\xi}_a}$.

In the summations in equation (3.11), *nelem* is the number of elements, and *ntbc* is the number of facets that have traction boundary conditions applied to them. The use of nodal integration points on the left-hand side of equation (3.11) results in explicit calculation of the acceleration at each node without solving a system of equations.

The choice of a tri-linear hexahedral element necessitates a discussion of the performance characteristics. It is well accepted that fully integrated the tri-linear hexahedron performs poorly for near-incompressible materials. This is of particular importance in this application, as the use of elastoplastic constitutive relations is all but a mandatory feature in any solid mechanics code. If a fully integrated hexahedron (8 independent integration points) is specified in conjunction with a near-incompressible material, the result is typically an overly stiff representation of the material or even mesh locking. The assumption of a tri-linear displacement field is the cause of such behaviors, as it is unable to adequately represent incompressible displacement fields ($\nabla \cdot \mathbf{u} = 0$).

There are several formulations that allow the tri-linear hexahedron to be used in combination with near-incompressible materials. Flanagan and Belytschko [36] have presented a uniform strain hexahedral element that contains a single integration point

in the center of the element. This approach effectively removes overly stiff behavior, but allows zero energy modes (hourglass modes) of deformation to form (i.e., patterns of nodal displacements occur that do not affect the strain in the center of the element). To combat the growth of these zero energy modes Flanagan and Belytschko [36] and Flanagan and Ong and Liu and Kennedy [37] specify the application of hourglass control forces. Due to its relative simplicity and computational efficiency, the uniform strain element is widely used in practice. Alternatively, selective reduced integration is proposed by Nagtegaal [38] and is extended by Hughes [39] in the form of the so-called B-bar methods. These approaches under-integrate the volumetric components of strain while keeping the standard integration for the deviatoric components. The assumed enhanced strain methods proposed by Simo and Rifai [40], and Simo and Armoro [41], and Simo and Armoro and Taylor [42] are particularly of interest. In this study, an enhanced low order formulation similar to that proposed by Souza *et al.* [43] and Rashid and Selimotic [44] is utilized for nearly incompressible material models. This formulation specifies 8 integration points within a single element, but enforces a uniform volume change in the kinematics used to update all material states in the element. Multiplying the deformation gradient at each integration point by a spatially varying scaling factor enforces the uniform volume change, thus assuring that the determinant of the incremental deformation gradient ($\hat{\mathbf{F}}$) will be constant across the element. Specifically, the average determinant of the incremental deformation gradient in a single element (K) is calculated using equation (3.1).

$$\det(\hat{\mathbf{F}})_{ave} = \frac{\int_K \det(\hat{\mathbf{F}}) dV}{\int_K dV}. \quad (3.12)$$

For each point in the element, a scaling factor may be defined as follows:

$$c = \left(\frac{\det(\hat{\mathbf{F}})_{ave}}{\det(\hat{\mathbf{F}})} \right)^{1/3}. \quad (3.13)$$

Thus multiplying the deformation gradient at each point by its associated scaling factor, as shown in equation (3.13), produces the *constant volume gradient* ($\hat{\mathbf{F}}_{cv}$).

$$\hat{\mathbf{F}}_{cv} = c \cdot \hat{\mathbf{F}}. \quad (3.14)$$

The constant volume gradient assures that the determinant of $\hat{\mathbf{F}}$ is constant over the entire element, and is used for all constitutive evaluations. However, it should be noted that the constant volume gradient should never be used for any kinematic transformations, as it is not fully descriptive of the actual displacement field.

3.1.4 Kinematics for Constitutive Input

The finite element methodology provides a means by which to calculate field gradients at any point on the interior of an element. These field gradients are used to generate kinematic variables suitable for updating the material state. In order to generate these kinematic variables, the incremental kinematics method given by Rashid [34] is used.

This method essentially decomposes the incremental deformation gradient ($\hat{\mathbf{F}} = \frac{\partial x^{n+1}}{\partial x^n}$) into an average “rate of deformation” tensor across the time step multiplied by the time step ($\mathbf{D}_a \cdot dt$), followed by a pure rotation $\hat{\mathbf{R}}$. The deformation tensor is input into the constitutive relation, and the resulting end of step state variables are then rotated using $\hat{\mathbf{R}}$.

3.2 Implementing the Cohesive Continuum Framework

3.2.1 Modeling the Rupturing Material

The implementation of the Cohesive Continuum Framework into a finite element code requires that the regions associated with the separation process be defined relative to the discretized problem. The separation facet (Γ) is used to represent a discrete section of the rupture surface. This facet, which is shared by both bulk elements prior to separation, and possibly the separation layer (Λ) are defined as shown in Figure 3.2. The separation layer is defined such that it intrudes into the surrounding bulk elements by a distance $\lambda/2$ on each side of the separation facet. It should be noted that the finite thickness layer approach requires that the separation layer be defined, but the surface based approach does not.

3.2.2 Tracking and Integrating Material States

3.2.2.1 Finite Thickness Layer Approach

The finite thickness layer approach assumes that a portion of each element surrounding the potential separation facet (Γ) contains material subject to rupture (Λ is defined in figure 3.2). In accordance with this assumption, the separation layer Λ (Figure 3.3, 3.4) may contain 2 to 8 *integration points* at a distance $Y_3 = \pm\lambda/4$ from the facet. An integration point on one side of the facet has a mirrored integration point on the other side of the facet, and together these integration points are referred to as an *integration couple*. The points that make up an integration couple have the same Y_1 and Y_2 coordinates, while the Y_3 coordinates have opposite sign. The number and location of the integration

points should mimic the integration rule used in the bulk elements. If a fully integrated element is specified, then the choice of 8 integration points (4 couples) is appropriate (Figure 3.4). If a reduced integration rule is used, then 2 integration points (1 couple) is appropriate (Figure 3.3). In figures 3.3 and 3.4 the locations of the integration points are marked by the solid rectangles.

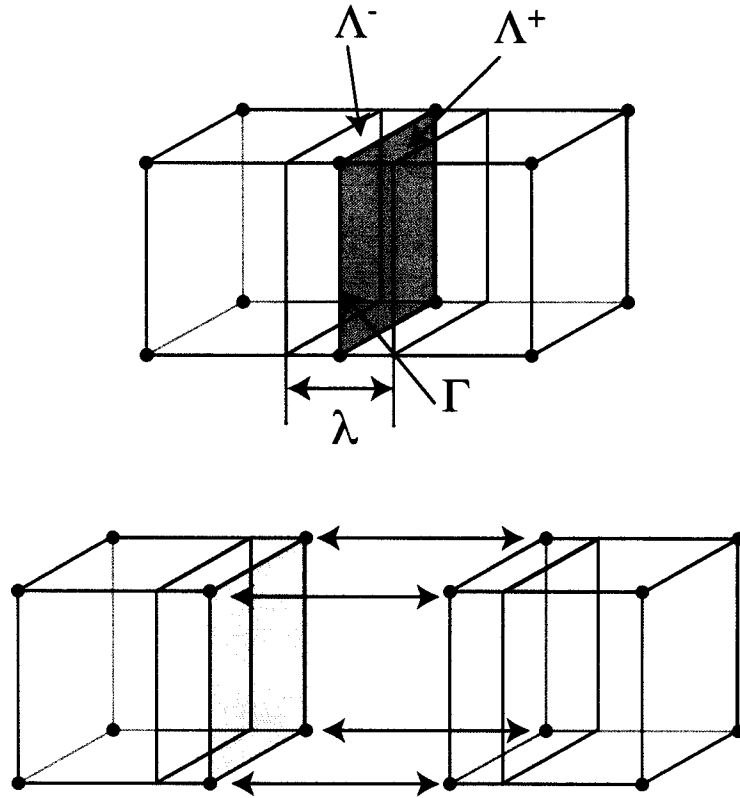


Figure 3.2: Separation Layer Λ as Portion of Bulk Elements

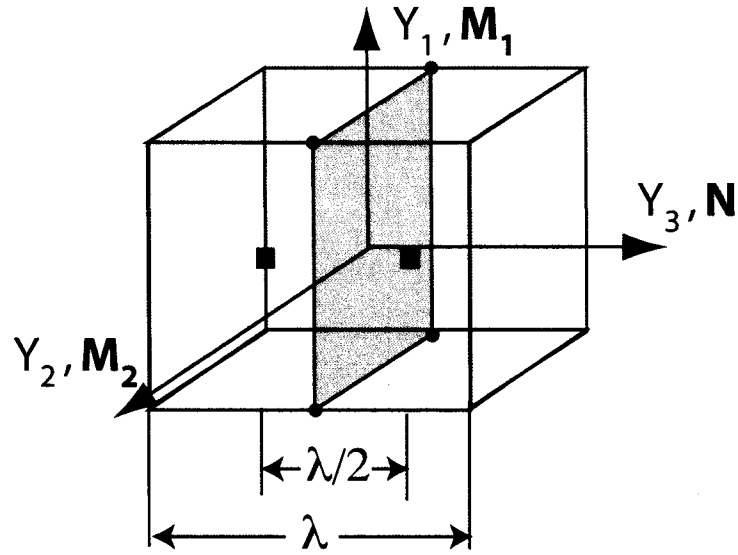


Figure 3.3: Diagram of Double-Point Integration for Δ

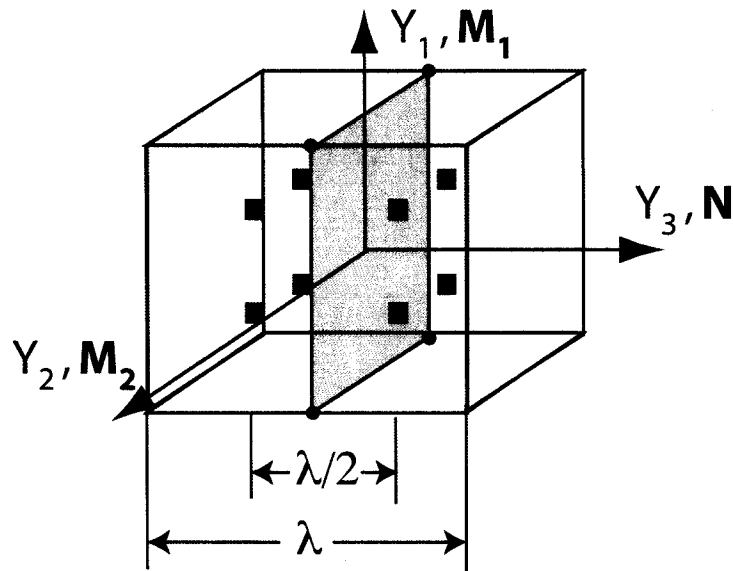


Figure 3.4: Diagram of Eight-Point Integration for Δ

The material states at the CCF integration points are updated under the assumption that \mathbf{G} (equation (2.8)) represents the deformation gradient in Δ . Prior to the initiation of the separation process ($\Phi < \Phi_1$), the gap vector (\mathbf{v}) is always equal to zero, thus \mathbf{G} is equal to

the standard continuum gradient. After the initiation of the separation process, the non-zero gap vector (\mathbf{v}) is calculated for each integration couple using a pair of formerly coincident points on the separation facet. This pair of points has the same Y_1 and Y_2 coordinates as the associated integration couple, but has an Y_3 coordinate equal to zero (i.e., the points initially lie on Γ). The presence of \mathbf{v} in \mathbf{G} causes G to differ from the value of the standard continuum gradient, thus the material state in Λ differs significantly from what would be calculated at the same material point using the continuum gradient.

It is clear that this implementation requires that the elements surrounding the separation facet be larger than $\lambda/2$ in the Y_3 direction. This requirement is a result of the manner in which the layer has been posed as a subspace of the discrete element. Thus the layer is not allowed to be larger than the element pair that it belongs.

3.2.2.2 Surface Based Approach

The surface based approach assumes that the rupture material only exists on the separation facet Γ . The potential rupture facet may contain 1 to 4 integration points in pattern similar to those illustrated in Figures 3.3 and 3.4. However, the Y_3 coordinates of the integration points are always zero. In addition, a pair of points must be defined such that they are a small distance away from the rupture facet Γ . These points represent $\mathbf{Z}^{+,-}$ as defined in section 2.2.2.2. Typical values for the perpendicular distance from the rupture facet Γ to a point $\mathbf{Z}^{+,-}$ range from 1-5% of the element length, as illustrated in Figure 3.5. Ideally a smaller value will provide superior stability over larger values, although smaller values may reduce the maximum stable time step.

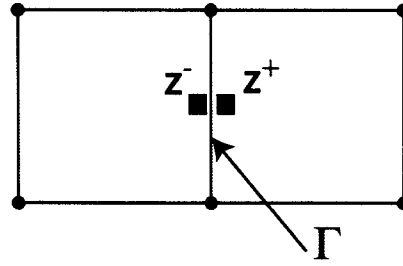


Figure 3.5: Internal Point Definition for FE Implementation of Surface Based Formulation

The material states at the CCF integration points are updated using \mathbf{G} (equation 2.10) as the assumed deformation gradient. Prior to the initiation of the separation process ($\Phi < \Phi_1$), the gap vector (\mathbf{v}) is always equal to zero, thus \mathbf{G} is equal to $\bar{\mathbf{F}}$. After the initiation of the separation process, the non-zero gap vector (\mathbf{v}) is calculated for each integration point using the pair of formerly coincident points, see equation (2.3).

3.2.2.3 Other Considerations

Use of the constant volume change element described in section 3.1.3 requires that the volume change condition must be enforced in some manner for the CCF material points as well as the standard continuum material points. It is decided that the constant volume change condition should be applied only to the portions of \mathbf{G} that are derived from the bulk element. Therefore the only terms in \mathbf{G} that are subjected to the constant volume change condition are those that taken from the bulk gradient \mathbf{F} .

3.2.3 Element Splitting and Node Duplication

In a standard FEM setting, the creation new surfaces along element boundaries require that node duplication occur. The duplication of a node is dependent on the values of the rupture function at the CCF integration points corresponding to the Γ to which the node is

connected. Specifically, whenever the value of the rupture function at a CCF integration point exceeds the specified value for initiation of rupture ($\Phi > \Phi_1$), the facet Γ is available for separation. Facets with ($\Phi > \Phi_1$) are referred to as “pending facets” to signify their readiness to participate in the node duplication process. When a node is surrounded by a collection of pending facets such that these facets provide a *closed path* around the node, the node is duplicated and the element connectivity is modified accordingly. A *facet path* is formed by traversing facet edges to move between neighboring facets. A *closed path of pending facets* implies that there exists a path that leads back to the facet at which the path originated, and that all facets along the path are pending facets. This logic is illustrated in Figure 3.6, where one non-duplication condition is presented along with two duplication conditions. Once a closed path is found, the node may be duplicated to form a new *node pair*, and element connectivity is reassigned such that one node belongs to all elements on one side of the facet path, and the other node belongs to elements on the opposite side.

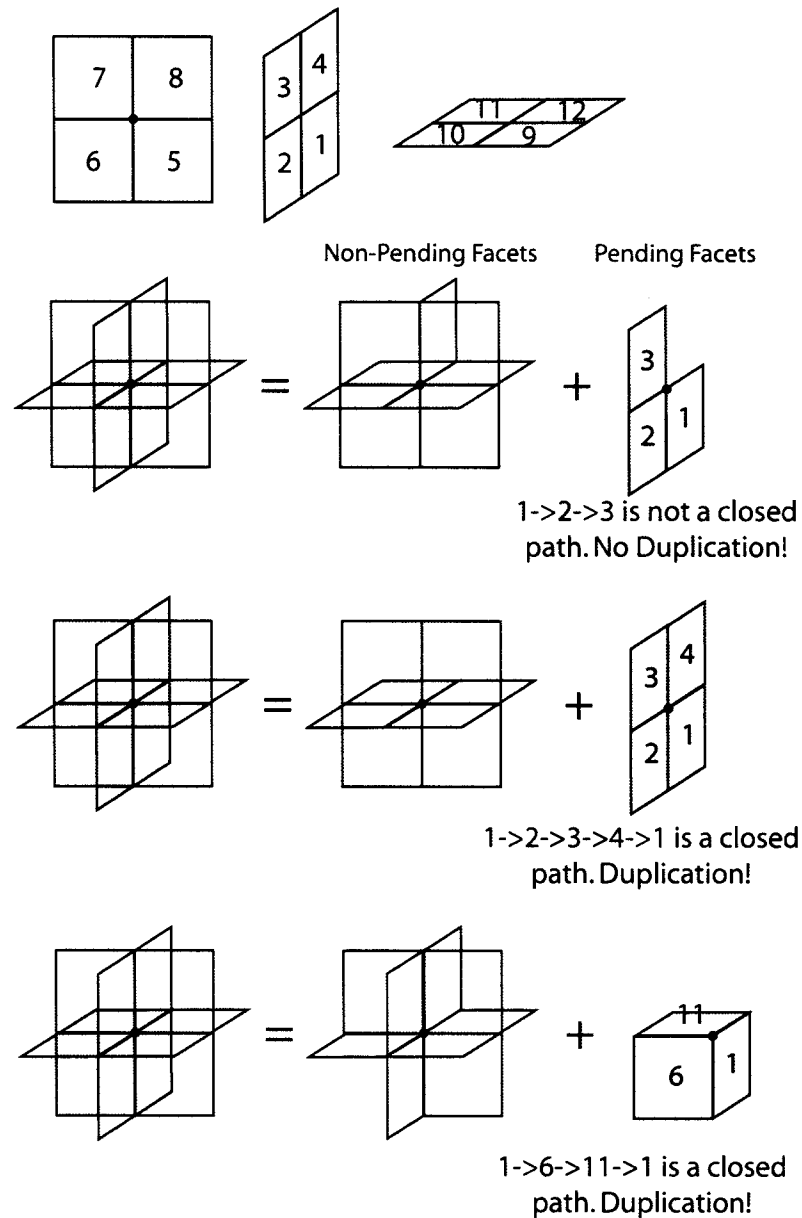


Figure 3.6: Facet-Based Nodal Duplication Scheme

3.2.4 Cohesive Stresses and Nodal Forces

Once a node has been duplicated, nodal forces corresponding to the cohesive stress must be applied to the resulting node pair. The description of cohesive stress application given in section 2.2.3 may be readily applied in the setting of the finite element method. The addition of a cohesive stress term requires that extra terms be added to the weak

equations of motion. The form of the additional terms is determined by the formulation used, as described in what follows.

3.2.4.1 Finite Thickness Layer Formulation

The procedure for cohesive stress application described in section 2.2.3.1 requires that the stress state in Λ be described at the interior CCF integration point, and that cohesive tractions defined in equation (2.20) be applied to the separation surface. As the separation surface (Γ) is represented by the separation facet, and the finite thickness layer Λ is explicitly defined as a portion of the surrounding continuum elements, the application of cohesive stresses results in terms being added to the equations of motion (equation (3.11)). The extra terms mimic the application of traction to a surface, as well as the presence of a cohesive stress state in Λ . Equation (3.11) is rewritten to show explicitly the additional cohesive terms:

$$\begin{aligned} \sum_{k=1}^{nelem} (\rho_0 a_{ai}^{n+1} |J_a|) = & \sum_{m=1}^{ntbc} \sum_{b=1}^4 \left(\left(\Phi_a \bar{p}_i^{n+1} |J_a| J_a^{-T} N \right) \right)_b - \sum_{k=1}^{nelem} \sum_{b=1}^8 \left(\left(\Phi_{a,j} P_{ij}^{n+1} \right) \right)_b |J_b| \\ & + \sum_{m=1}^{ncf} \sum_{b=1}^4 \sum_{side=1}^2 \left(\left(\Phi_a (-1)^{side+1} (P_c^{n+1})_i |J_a| J_a^{-T} N \right) \right)_b - \left(\left(\Phi_{a,j} (P_c^{n+1} - P^{n+1})_{ij} \right) \right)_b |J_{\Lambda b}| \end{aligned} \quad (3.15)$$

The last term in equation (3.15) represents the contribution of the CCF to the equations of motion. In the additional term, the outer summation limit “ ncf ” represents the number of cohesive facets/layers that are undergoing the separation process. The inner summation loops over the number of CCF integration points on/in a facet/layer. To simplify the explanation and implementation, the number of integration points is set at 4. If reduced integration point is desired, the location of all 4 integration points may be set to the middle of the facet or layer cross-section as shown in Figure 3.3.

The first part of the cohesive term in equation (3.15) applies the cohesive tractions (as defined in equation (2.20)) to the surface of the separating facet in the same manner in which boundary tractions are applied to an external facet. The second part of the cohesive term provides nodal force contributions from the cohesive stress (\mathbf{P}_c) minus the bulk stress (\mathbf{P}) within volume Λ . This is done for each of the two elements that surround the separating facet. Each element has an appropriately scaled Jacobian determinant ($\mathbf{J}_{\Lambda b}$) such that the numerical integration results in only a portion of the element volume being attributed to the volume Λ . The subtraction of the bulk stress is necessary due to the fact that Λ contributes nodal forces based on the bulk stress as a result of the standard bulk element formulation (second overall term in equation (3.15)). If this subtraction were not performed, the volume Λ would essentially apply nodal force contributions twice with \mathbf{P} and \mathbf{P}_c each being used once to represent the stress in the layer. This procedure requires that the bulk material state be calculated at the CCF integration for this purpose. - i.e., a material state is tracked at the CCF integration point location using the \mathbf{F} in addition to \mathbf{G} .

3.2.4.2 Surface Based Formulation

The procedure for cohesive stress application described in section 2.2.3.2 consists of the application of tractions on the separating facets, and the correction of the nodal forces to restrict energy generation. As in the previous section, the separation surface Γ is discretized into a collection of separating facets. Application of tractions to these facets results in an extra term in the equations of motion, which are written as:

$$\begin{aligned}
\sum_{k=1}^{nelem} (\rho_0 a_{ai}^{n+1} |\mathbf{J}_a|) &= \sum_{m=1}^{nibc} \sum_{b=1}^4 \left(\left(\Phi_a \bar{P}_i^{n+1} |\mathbf{J}_a| \|\mathbf{J}_a^{-T} \mathbf{N}\| \right) \right)_b - \sum_{k=1}^{nelem} \sum_{b=1}^8 \left(\left(\Phi_{a,j} P_{ij}^{n+1} \right) \right)_b |\mathbf{J}_b| \\
&+ \sum_{m=1}^{ncf} \sum_{b=1}^4 \sum_{side=1}^2 \left(\left(\Phi_a (-1)^{side+1} (\mathbf{p}_c^{n+1})_i |\mathbf{J}_a| \|\mathbf{J}_a^{-T} \mathbf{N}\| \right) \right)_b.
\end{aligned} \tag{3.16}$$

Equation (3.16) utilizes the cohesive traction (\mathbf{p}_c) defined in equation (2.21), and applies the traction in the same manner as boundary tractions are applied to external facets. As above, the outer summation limit “ ncf ” represents the number of cohesive facets that are undergoing the separation process, while the inner summation loops over the number of CCF integration points on a facet. To simplify the explanation and implementation, the number of integration points is once again set to 4.

Once the nodal force contributions from all the CCF facets are compiled, they must be subjected to an energy limiter as described in equation (2.24). If two nodes, referred to as node 1 and node 2, are the result of node duplication, then the sum of the cohesive forces dotted with the velocity of the nodes upon which they act may never be positive. This is written as:

$$\mathbf{f}_{c1} \cdot \dot{\mathbf{u}}_1 + \mathbf{f}_{c2} \cdot \dot{\mathbf{u}}_2 \leq 0. \tag{3.17}$$

In this relation, \mathbf{f}_c is the nodal force that results from the cohesive traction, and $\dot{\mathbf{u}}_1$ is used to represent velocity of the node to ensure that the velocity is not mistaken for the gap vector (\mathbf{v}). This condition must be enforced for every node pair that results from node duplication. Furthermore, for a node that is duplicated only once, it is known that the cohesive forces are equal and opposite. Thus the cohesive force \mathbf{f}_c may replace \mathbf{f}_{c1} and \mathbf{f}_{c2} through the relation $\mathbf{f}_c = \mathbf{f}_{c1} = -\mathbf{f}_{c2}$. This substitution, along with the specification of the time that the relation applies (t^{n+1}), yields:

$$\mathbf{f}_c^{n+1} \cdot (\dot{\mathbf{u}}_{c1}^{n+1} - \dot{\mathbf{u}}_2^{n+1}) \leq 0 \quad (3.18)$$

Defining the nodal force resulting from the bulk element contributions as \mathbf{f}_b and the mass associated with the node as m , the velocity at t^{n+1} may be written as:

$$\begin{aligned} \dot{\mathbf{u}}^{n+1} &= \dot{\mathbf{u}}^n + \frac{1}{2}(\mathbf{a}^n + \mathbf{a}^{n+1}) \cdot \Delta t \\ \dot{\mathbf{u}}^{n+1} &= \dot{\mathbf{u}}^n + \frac{1}{2}\mathbf{a}^n \cdot \Delta t + \frac{1}{2}(\mathbf{f}_b^{n+1} + \mathbf{f}_c^{n+1}) \cdot \Delta t / m \\ \dot{\mathbf{u}}^{n+1} &= (\dot{\mathbf{u}}^n + \frac{1}{2}\mathbf{a}^n \cdot \Delta t + \frac{1}{2}\mathbf{f}_b^{n+1} \cdot \Delta t / m) + \frac{1}{2}\mathbf{f}_c^{n+1} \cdot \Delta t / m \end{aligned} \quad (3.19)$$

The last form of equation (3.19) indicates that the velocity at t^{n+1} depends on the velocity and acceleration at t^n , the nodal force due to the bulk elements at t^{n+1} , and the nodal force due to the cohesive tractions at t^{n+1} . Therefore the velocity at t^{n+1} may be directly manipulated by altering \mathbf{f}_c^{n+1} . Therefore \mathbf{f}_c^{n+1} is multiplied by a scale factor (c_s), as described in equation (2.23), to enforce the condition in equation (3.18). Substituting (3.19) into (3.18), defining $\dot{\mathbf{u}}_b^{n+1/2} = (\dot{\mathbf{u}}^n + \frac{1}{2}\mathbf{a}^n \cdot \Delta t + \frac{1}{2}\mathbf{f}_b^{n+1} \cdot \Delta t / m)$, and applying the scale factor to \mathbf{f}_c yields:

$$\begin{aligned} c_s \mathbf{f}_c^{n+1} \cdot \left\{ \left[\dot{\mathbf{u}}_{b1}^{n+1/2} + \frac{1}{2}c_s \mathbf{f}_c^{n+1} \cdot \Delta t / m \right] - \left[\dot{\mathbf{u}}_{b2}^{n+1/2} + \frac{1}{2}c_s \mathbf{f}_c^{n+1} \cdot \Delta t / m \right] \right\} &\leq 0 \\ c_s \mathbf{f}_c^{n+1} \cdot (\dot{\mathbf{u}}_{b1}^{n+1/2} - \dot{\mathbf{u}}_{b2}^{n+1/2}) + \frac{c_s^2 \Delta t}{m} (\mathbf{f}_c^{n+1} \cdot \mathbf{f}_c^{n+1}) &\leq 0. \end{aligned} \quad (3.20)$$

If the condition in equation (3.20) is violated, the scaling factor may be adjusted to a value between $[0,1]$ such that the equivalence condition is satisfied. The scaling factor is calculated as:

$$\begin{aligned} c_s \mathbf{f}_c^{n+1} \cdot (\dot{\mathbf{u}}_{b1}^{n+1/2} - \dot{\mathbf{u}}_{b2}^{n+1/2}) + \frac{c_s^2 \Delta t}{m} (\mathbf{f}_c^{n+1} \cdot \mathbf{f}_c^{n+1}) &= 0 \\ c_s &= \left\langle -\frac{m \mathbf{f}_c^{n+1} \cdot (\dot{\mathbf{u}}_{b1}^{n+1/2} - \dot{\mathbf{u}}_{b2}^{n+1/2})}{\Delta t (\mathbf{f}_c^{n+1} \cdot \mathbf{f}_c^{n+1})} \right\rangle. \end{aligned} \quad (3.21)$$

Again note that c_s must always lie between zero and unity. It is important to note that this procedure only applies for separable nodes that are allowed to duplicate only a single

time. If multiple node duplications are required, the task of applying an energy limiter becomes much more complex. For this reason, only single duplications are addressed in this study.

3.2.5 Cohesive Damping Traction and Anti-Intrusion Traction

In structural dynamics simulations, it is often desirable to introduce damping to reduce high frequency noise that may be generated as a result of the analysis. While it is shown in the following section that the CCF does not require damping to attain physical results, it is still advantageous to provide a means by which to damp certain undesired motions. For example, use of the constant volume elements appears to have slightly detrimental effects on the overall stability of problems containing active CCF elements. These stability concerns are often extremely subtle, and often do not appear in most constant volume element enabled analysis. However, when the instability does appear, it may be controlled by specifying a *cohesive damping traction* ($\mathbf{p}_{\text{damping}}$), which is proportional to the rate of the gap vector. This cohesive damping traction is defined as:

$$\mathbf{p}_{\text{damping}} = \left(2\gamma_{\text{ccf}} \sqrt{\rho_0 (\lambda_{\text{Lamé}} + 2\mu)} \right) \dot{\mathbf{v}},$$

where :

- γ_{ccf} is the cohesive damping coefficient
- $\lambda_{\text{Lamé}}$ is the elastic Lamé's constant
- μ is the elastic shear modulus
- $\dot{\mathbf{v}}$ is the rate of the gap vector .

(3.22)

The parameters used in equation (3.22) are taken from the material parameters of the bulk material save the cohesive damping coefficient. Values of the cohesive damping coefficient typically range from 0.01 to 0.5, although the effects of the damping on the

overall solution should always be checked to ensure that it does not alter the overall solution.

Another concept that is of use in practice is the application of a so-called *anti-intrusion traction*. It will be demonstrated that the CCF inherently provides some measure of resistance to inter-penetration between the two surfaces of the cohesive facet. In some cases it is desirable to introduce an additional resistance to intrusion. To this end, the anti-intrusion traction is defined as:

$$\mathbf{p}_{\text{intrusion}} = \left[\frac{(\mathbf{n} \cdot \mathbf{v})}{\lambda} (\lambda_{\text{lamee}} + 2\mu) \right] \mathbf{n},$$

where :

- λ_{lamee} is the elastic lamee's constant
- λ is the length scale
- μ is the elastic shear modulus
- \mathbf{v} is the gap vector
- $\mathbf{n} = \bar{\mathbf{F}}^{-T} \mathbf{N} / |\bar{\mathbf{F}}^{-T} \mathbf{N}|$.

(3.23)

To apply the damping and intrusion tractions, their values are simply added to the cohesive tractions as such:

$$\mathbf{p} = \mathbf{p}_c + \mathbf{p}_{\text{damping}} + \mathbf{p}_{\text{intrusion}}$$
(3.24)

The tractions that result from equation (3.24) are then used in place of the cohesive traction in equations (3.15) and (3.16). Although the additions of damping and anti-penetration tractions are outside the scope of the CCF, and for the majority of problems unnecessary, they provide a valuable addendum to the concept by adding increased reliability and greater resistance to non-physical surface penetrations.

3.3 Summary

In this section a description of an explicit dynamics finite element code has been presented. The derivation of the equations of motion discretized for a finite element application have been presented, as well as a description of the explicit time stepping scheme and element formulations used. This code serves as the platform by which the Cohesive Continuum Framework is to be tested. Implementations of both the finite thickness layer and the surface based formulations of the CCF are described in detail. These descriptions cover the generation of enriched kinematic input for updating the rupturing material states, and appropriate methods of cohesive stress application such that stable solutions are attained.

4 Numerical Results

In this section the results of a series of Cohesive Continuum Framework enhanced finite element analyses are presented. To demonstrate the flexibility of the CCF, multiple material models are specified in various example problems. These examples are intended to illustrate the performance of the CCF with regard to key goals such as reversibility, time continuity, and constraint sensitivity.

4.1 Material Models

As stated in section 2.2.1, the ability of the rupture function to model a specific rupture process is entirely dependent on the state variables made available by the chosen material model. If the material model does not provide an adequate description of the material process that underlies the rupture process, then the rupture function has little chance of accurately modeling rupture. For the purposes of illustration and exploration, two bulk constitutive models were implemented as described below.

4.1.1 Linear Elasticity

The first material modeled was a brittle steel, for which a simple linear elastic constitutive relation was specified. The linear elastic assumption may be expressed by relating the rate of stress to the rate of deformation as follows:

$$\dot{\mathbf{T}} = \lambda \cdot \text{tr}(\mathbf{D}_a) + 2\mu\mathbf{D}_a. \quad (4.1)$$

This simple material description is used to provide a means by which the features of the CCF may be studied without being influenced by a more complex constitutive relation. As such, the linear elastic relation is used in the simple test problems that are intended to illustrate basic model behaviors.

The CCF requires that the selection of a constitutive assumption be accompanied by a definition of the rupture function. As the only state variable present in this constitutive relation is the stress tensor, the rupture function must be constructed from the stress tensor only. Accordingly, the rupture function is chosen as:

$$\begin{aligned}\Phi_{rupture} &= \sigma_1 \\ \text{where :} \\ \sigma_1 &\text{ is the maximum eigenvalue}\end{aligned}\tag{4.2}$$

This choice of rupture function is equal to the magnitude of the traction on the plane with normal \mathbf{n} . The units of the rupture function are stress, thus Φ_1 and Φ_2 are the stresses at which rupture initiates and completes respectively. As discussed in section 2.2.3, calculation of a cohesive stress requires the definition of a so-called stress reduction factor. For this material, 2 stress reduction factors are defined as:

$$r \approx e^{-\frac{s}{0.045}}\tag{4.2a}$$

$$r = 1 - s,\tag{4.2b}$$

where s is the separation coefficient. The first stress reduction factor is applied in conjunction with a limiting condition such that the magnitude of the cohesive traction does not exceed 800 MPa. This first specification is used when attempting to model the brittle steel. The second stress reduction factor is used only for the test plate load-path tests that are intended to show features of the CCF rather than model a specific real material.

4.1.2 Gurson Void Growth

The second material used in this study is a forged 21-6-9 steel. This material is expected to exhibit ductile fracture through void growth and coalescence. Therefore, a measure of void growth should be used in the rupture function. Rice and Tracy [45] suggest that a standard J2-Plasticity constitutive relation may be used, where the void growth is related to plastic strain and stress triaxiality. However, Gurson [32, 33] provides a material model that directly tracks void growth, which makes it a better-suited candidate to model the rupture process in this material. The Gurson model presented here is a rate-independent elastic-plastic softening model, in which it is assumed that evolution of the yield-stress obeys power law hardening:

$$Y = Y_0 \left[1 + \left(\frac{\varepsilon_{eps}}{\varepsilon_{ref}} \right)^h \right]. \quad (4.3)$$

Through this relation, the magnitude of the yield stress increases with increasing *effective plastic strain* ($\dot{\varepsilon}_{eps} = \sqrt{2/3 \mathbf{D}_p : \mathbf{D}_p}$ where \mathbf{D}_p is the plastic part of the rate of deformation tensor). The Gurson model specifies a yield surface that exhibits softening through terms involving the void volume fraction (f) state variable. Needleman and Tvergaard [46] modified Gurson's work to give the modified Gurson yield surface:

$$\phi_{GURSON} = \left(\frac{s_{vm}}{Y} \right)^2 + 2 \cdot Q_1 \cdot f \cdot \cosh \left(\frac{3}{2} \frac{Q_2 \cdot p}{Y} \right) - \left[1 + (Q_1 \cdot f)^2 \right] = 0. \quad (4.4)$$

where ($S_{ij} = T_{ij} - p\delta_{ij}$) is the deviatoric stress, and ($s_{vm} = \sqrt{\frac{3}{2} S_{ij} S_{ij}}$) is the von-Mises

stress. It is the second term in equation (4.4) that allows the Gurson yield surface to shrink as f increases. In fact the yield surface shrinks to a point as the void volume fraction (f) approaches a critical value ($f_c = 1/Q_1$). The size of the surface also varies with

pressure. If the pressure is large, the \cosh term is large, and the softening effects of the void volume fraction are amplified. In contrast, if the pressure is small the softening effects of the void volume fraction are reduced.

Note that the void volume fraction (f) is a variable that is intended to track the volume of the voids divided by the total volume in an arbitrary region. While the existence of physical voids would introduce a length scale into the problem through the void radius or the distance between voids, the Gurson model is still a continuum-based formulation and does not provide an actual description of finite length features. Thus the voids are not treated as micro-structural entities. Instead, they are accounted for by considering a homogenized, unvoided material that exhibits dilatant plasticity.

Since plasticity does not allow for volume change, the volumetric portion of the plastic strain tensor must be attributed to void growth. Thus the evolution of the void volume fraction is calculated through the simple relation:

$$\dot{f} = (1 - f) \text{tr}(\mathbf{D}_p). \quad (4.5)$$

In addition to growth of existing voids, the ability to nucleate voids is essential to the modeling process. Various nucleation models have been proposed by Gurson [33] and Needleman and Rice [47] and Chu and Needleman [48]. A combination of these approaches are used as follows:

$$\dot{f}_{nucleation} = \dot{\epsilon}_p \frac{f_\epsilon}{\sigma_\epsilon \sqrt{2\pi}} e^{-\frac{1}{2} \left(\frac{\epsilon - \epsilon_N}{\sigma_\epsilon} \right)^2} + \dot{p}_{max} \frac{f_p}{\sigma_p \sqrt{2\pi}} e^{-\frac{1}{2} \left(\frac{p_{max} - p_N}{\sigma_p} \right)^2},$$

where :

$\dot{\epsilon}_p$ is the rate of effective plastic strain

\dot{p}_{max} is the rate of increase in the maximum pressure seen by the material

f_ϵ is the maximum void volume fraction nucleated by the strain term (4.8)

f_p is the maximum void volume fraction nucleated by the pressure term

ϵ_N is the mean strain at which the distribution is centered

p_N is the mean pressure at which the distribution is centered

σ_ϵ is the standard deviation of strain based distribution

σ_p is the standard deviation of pressure based distribution.

This relation specifies that the nucleation of voids be normally distributed around a mean effective plastic strain and a mean pressure. The amount of void volume fraction that may be nucleated through strain and pressure is equal to f_ϵ and f_p respectively. Note that Chu and Needleman use $(p+Y)$ rather than p for the stress based nucleation.

Since the void volume fraction provides a direct measure of the amount of voids present in a material, it is a prime candidate for use in the rupture function. In this work the rupture function is simply set equal to the void volume fraction.

Through numerical experimentation, it has been determined that the near-incompressible nature of the Gurson model (prior to void growth) induces non-physical behavior when the surface based formulation is specified. Specifically, the reversibility features of the CCF perform poorly when the surface based formulation is used in conjunction with a near-incompressible material: A change in loading direction or intrusion causes the method to exhibit non-physical behavior in the form of high amplitude stress cycles. For

this reason, only the finite thickness layer formulation is applied to problems involving the Gurson constitutive model.

4.1.3 Material Model Summary

Table 4.1 presents a summary of material parameters used in the following analyses. In the Gurson model, the values are $Q1$ and $Q2$ are taken from Tvergaard [49, 50]. Brown and Embury [51] and Andersson [52] provide a guideline for initial estimates of Φ_2 .

Material Model	Linear Elastic	Gurson
	$\rho = 7900 \text{ kg/m}^3$ $E = 1.9\text{E}11 \text{ Pa}$ $\nu = 0.3$	$\rho = 7900 \text{ kg/m}^3$ $E = 1.9\text{E}11 \text{ Pa}$ $\nu = 0.3$ $Y_0 = 6.8\text{E}8 \text{ Pa}$ $\epsilon_{\text{ref}} = 0.58$ $h = 0.56$ $f_{\text{init}} = 0.0$ $Q_1 = 1.5$ $Q_2 = 1.0$ $f_\epsilon = 0.02$ $\epsilon_N = 0.3$ $\sigma_\epsilon = 0.1$ $f_p = 0.005$ $p_N = 1.75\text{E}9 \text{ Pa}$ $\sigma_p = 2.5\text{E}8 \text{ Pa}$
Rupture Parameters	$\Phi = \sigma_1$ $\Phi_1 = 8.0\text{E}8$ $\Phi_2 = 2.0\text{E}10$	$\Phi = f$ $\Phi_1 = 0.02$ $\Phi_2 = 0.4$
Stress Reduction Function	$r \approx e^{-\frac{s}{0.045}}$ or $(1-s)$	$r = (1 - s^{1.5})$
Length Scale	20 μm	100 μm

Table 4.1

4.2 Elementary Model Behavior

The elementary behavior of the cohesive continuum framework enhanced finite element code is presented in this section. For these simulations, a simple plate problem is

specified, as shown in Figure 4.1. This plate consists of 98 nodes and 36 elements. The nodes along the vertical ($X_2=0$) centerline of the mesh are specified as “separable,” and are therefore candidates for duplication. To restrict this problem such that separation occurs only on the centerline of the mesh, only facets that lay on the centerline ($\mathbf{N}=[1,0,0]$) are allowed to participate in the separation process.

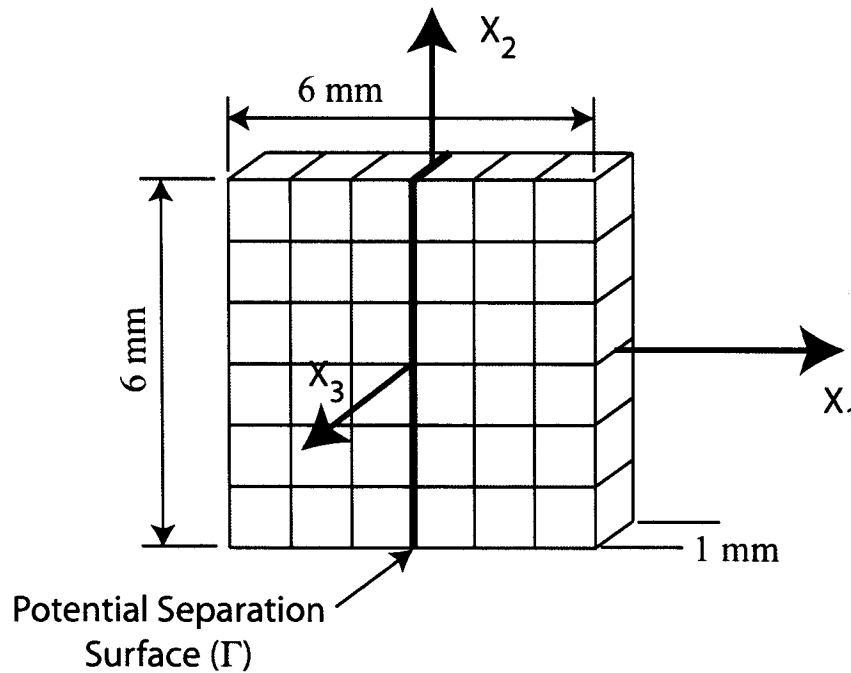


Figure 4.1: Illustration of Simple Test-Plate Mesh

4.2.1 Uniaxial Behavior

To determine the behavior of the CCF in uniaxial strain loading (1D loading), the simple plate problem is subjected to kinematic boundary conditions such that the nodes on the right side of the mesh ($X_1=3$ mm) are pulled in the positive X_1 direction, and the nodes on the left face of the mesh ($X_1=-3$ mm) are pulled in the negative X_1 direction at a velocity of 0.01 m/s. To achieve uniaxial strain loading, all nodes are confined in the X_2 and X_3

directions for the duration of the simulation. Both the brittle (linear elastic) and ductile (Gurson) materials were used.

Since the goal of these simple simulations is to illuminate the behavior of the CCF itself, the data is presented in terms of the cohesive tractions plotted against gap opening displacement for one of the center facets. While this choice of data does not provide all information pertaining to the behavior of a given simulation (e.g. there are other factors that effect the equations of motion in the finite thickness layer formulation), the cohesive tractions and gap opening displacements do provide a point of comparison to traction-separation relations used in cohesive zone methods. The overall applied force versus displacement curves are not presented, as their inclusion might (falsely) suggest that these tests are intended to simulate uniaxial tension tests.

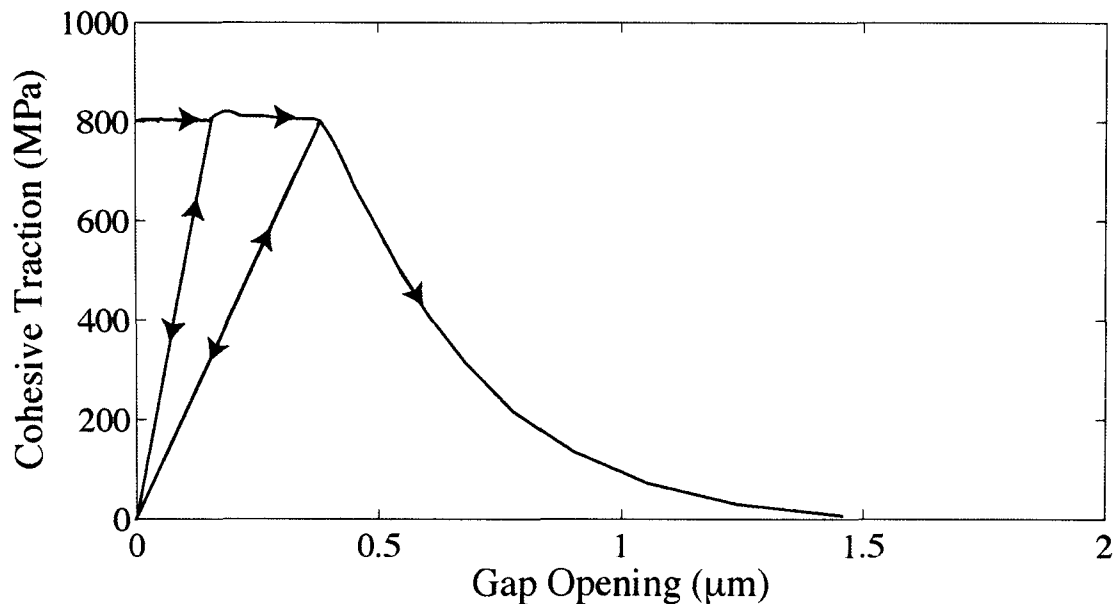


Figure 4.2: Cohesive Traction vs Gap Opening for Finite Thickness Layer Formulation Under Uniaxial Strain Loading – Linear Elastic

4.2.1.1 Linear Elastic Material

The finite thickness layer and surface based formulations have been tested using the plate problem under uniaxial strain loading with two unload/reload cycles. The *cohesive traction* versus *gap opening displacement* curves that result from the finite thickness layer formulation are plotted in Figure 4.2, and the results for the surface based formulation are plotted in Figure 4.3. Since the tractions for the linear elastic material have been limited to 800 MPa, each traction separation curve is initially flat. The small oscillations present along this portion of the curve are a result of the stress reduction factor being specified at discrete points and linearly interpolated, rather than specified as a continuous function.

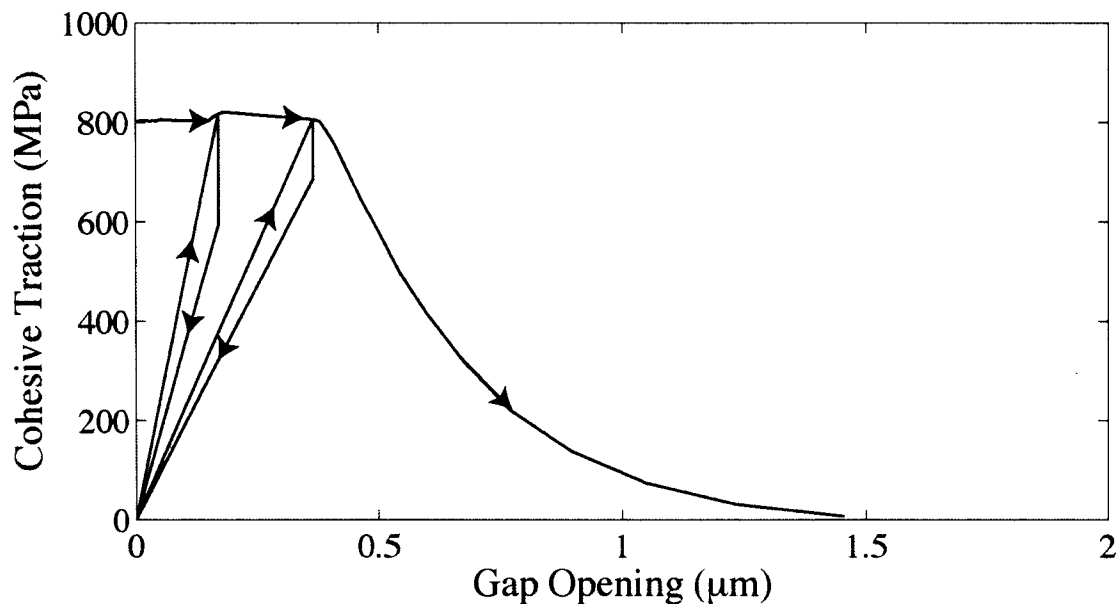


Figure 4.3: Cohesive Traction vs Gap Opening for Surface Based Formulation Under Uniaxial Strain Loading – Linear Elastic

The unload/reload cycle for the FTLF is a simple linear elastic line back to the origin.

The surface based formulation presents a much more intricate unloading process. To emphasize, it is the cohesive traction that is shown in the plot, not the nodal force. As a result of the energy limiter described in section 3.2.4.2, the nodal forces that result from

the cohesive tractions may be scaled to ensure that they do no work on the body. In light of this, the traction separation curve shown in Figure 4.3 does not necessarily represent the actual effects of the cohesive tractions on the nodes. To gain a complete picture, consider what occurs as a result of the energy limiter. As the body is unloaded, the gap may try to close. If the cohesive tractions are pulling the gap closed, then the energy limiter is applied such that the cohesive nodal forces are reduced and the gap does not close, thus ensuring that no work is done by the cohesive tractions. For this reason the unload curve is initially vertical, which indicates that there is no gap closure. This process occurs until the scaling factor reaches zero, at which point the cohesive forces have no ability to do work and the gap may close. In other words, in the traction separation curve, the portion of the unloading curve that approaches the origin actually corresponds to zero cohesive nodal force. Thus the nodal force curve should actually drop vertically to the abscissa, and then travel horizontally to the origin. This is confirmed when the cohesive forces that result from the tractions and energy limiter are plotted as in Figure 4.4. This shows that the surface based formulation will actually dissipate energy during a complete unload/reload cycle. This behavior is expected as the energy limiter specifies only that the cohesive forces may not do positive work. As a consequence, the nodes are free to move in any manner that the dynamics of the problem dictate, as long as that motion does not result in positive work done by the cohesive forces.

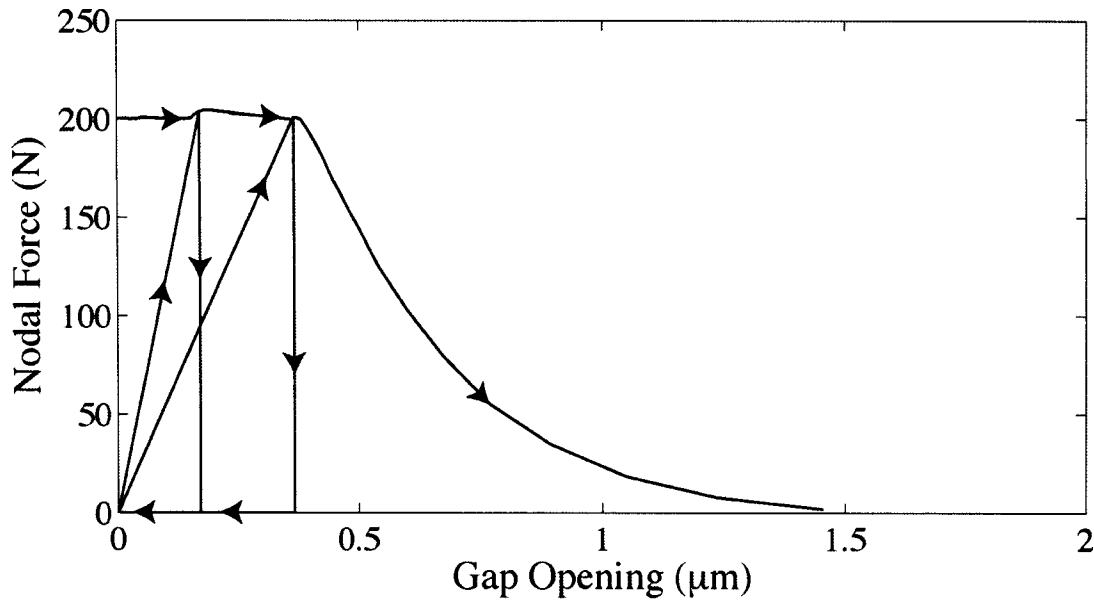


Figure 4.4: Cohesive Nodal Forces vs Gap Opening for Surface Based Formulation Under Uniaxial Strain Loading – Linear Elastic

4.2.1.2 Gurson Material

A similar uniaxial strain analysis was carried out using the Gurson constitutive assumption. However, only the finite thickness layer formulation was used for reasons discussed in section 4.1.2. Figure 4.5 presents the *cohesive traction vs gap opening* relation. The major insight to be gained from this plot is that the unload/reload curve does not pass through the origin. Instead, the unload/reload drops to the abscissa value that corresponds to zero elastic strain. As is the case in standard continuum problems, plastic strain results in permanent deformation (continuum deformation + gap opening) that is not recovered upon unloading.

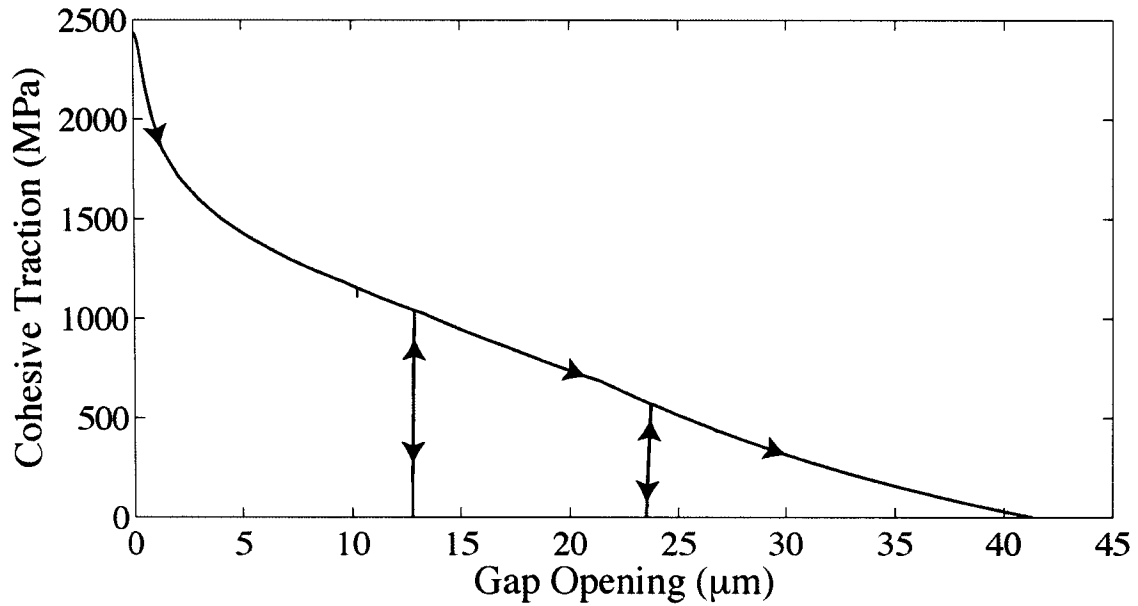


Figure 4.5: Cohesive Traction vs Gap Opening for Finite Thickness Layer Formulation Under Uniaxial Strain Loading – Gurson

4.2.2 Multiaxial Cyclic Behavior

To illustrate how the CCF responds to complex loading paths, the simple plate mesh shown in Figure 4.1 was subjected to a loading path that combines axial/shear loading, contains several changes of the loading directions, and involves compression to test the ability of the model to resist intrusion. Figure 4.6 illustrates the loading path in terms of displacement vectors, which are applied to the left and right extremes of the mesh via velocity boundary conditions (the B.C. applied to the left extreme is the negative of the path shown). In addition, images of the deformed meshes are illustrated on the path to show the effects that a loading path has on the mesh. A particular portion of the loading path is identified by the letter that is placed at the end of the path in Figure 4.6. The magnitude of the specified velocities start at zero, increase linearly throughout the first half of the loading segment, then decrease linearly to zero at the end of the loading segment. As the goal of this experiment is to display features of the CCF as clearly as

possible, the linear elastic constitutive model is used. Furthermore, the stress reduction factor specified in equation 4.2 is replaced by $(1-s)$ in order to simplify the traction separation relation.

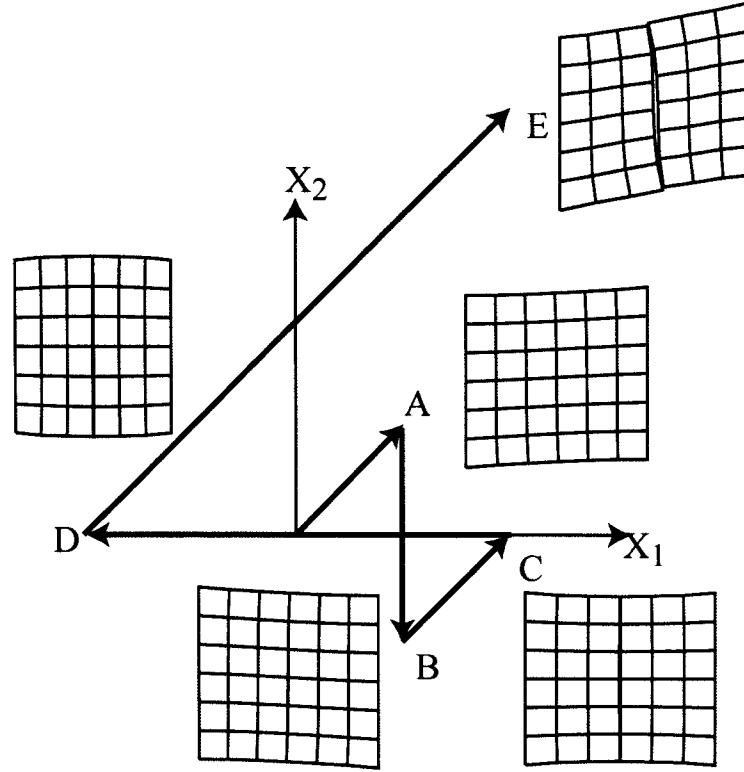


Figure 4.6: Complex Load Path for Test-Plate

Figures 4.7 and 4.8 plot the normal and shear Cauchy tractions within one of the facets along the separation plane for both finite thickness and surface based formulations. In addition, to illustrate the effects of cohesive damping as defined in section 3.2.5, the analyses are run with and without damping. The letters on the plots are used to signify the end of each loading path as defined in Figure 4.6.

Loading path A is a combination of normal tension and shear. Sometime during this path, the rupture criterion is satisfied for all facets on the potential separation plane, and node duplication occurs. The duplication results in slight ripples in the stress and gap

displacement, indicated that time continuity may be an issue. Time continuity will be discussed further in the next section.

Loading path B is a shear load that reverses the component of shear loading from path A, but keeps the normal displacement fixed. It is seen that the shear traction and gap displacement completely reverse direction in a linear fashion, while the normal traction stays nearly constant.

Loading path C is identical in direction to loading path A, but at the end of this loading path, the problem ends up in pure normal tension. As expected, the normal component of the traction and gap vectors increase in a manner similar to what is observed during loading path A. The normal component ends at some positive value, while the shear component approaches the origin.

Loading path D then enforces a normal compression on the mesh. For the finite thickness layer formulation, the normal components of the traction and gap vector approach zero with a linear relation to each other, similar to the unload/reload cycles observed in the uniaxial strain loadings from section 4.2.1.1. For the surface based formulation, the energy limiter has the same effect on the unloading as in section 4.2.1.1. Once the origin is reached and intrusion occurs, the cohesive stresses reverse sign and push the separation surfaces apart. However, as long as the stress-reduction factor is still applied to the cohesive stresses, a finite amount of intrusion cannot be prevented. Attempts to temporarily set the stress reduction factor to unity while intrusion is taking place have

proven to cause complications that are considered a strong enough deterrent as to accept the intrusion for the time being. However, the anti-intrusion traction does provide some measure of additional intrusion resistance, as is evident through the change in slope after the gap displacement becomes negative. This loading illustrates how the CCF provides resistance to intrusion naturally, but does not provide a strict no-interpenetration rule.

Loading path E again mimics the loading from A and C. The normal loading curve moves back up the unload/reload curve from D. The shear loading starts from the beginning of the loading path, thus causing the normal loading to deviate from the unload-reload path prior to reaching the previous point at which the unload from path D began (note no shear loading at beginning of path D).

The use of cohesive damping as defined by equation 3.22 is shown to “smooth” the traction-separation relations, especially in the shear directions. Since the overall loading path remains unaffected, moderate cohesive damping is considered not to significantly alter the solution.

With this simple problem we have shown an example of how the CCF possesses a natural ability to simulate fracture problems which are subjected to combined loading, changes in loading direction, unloading, and even intrusion.

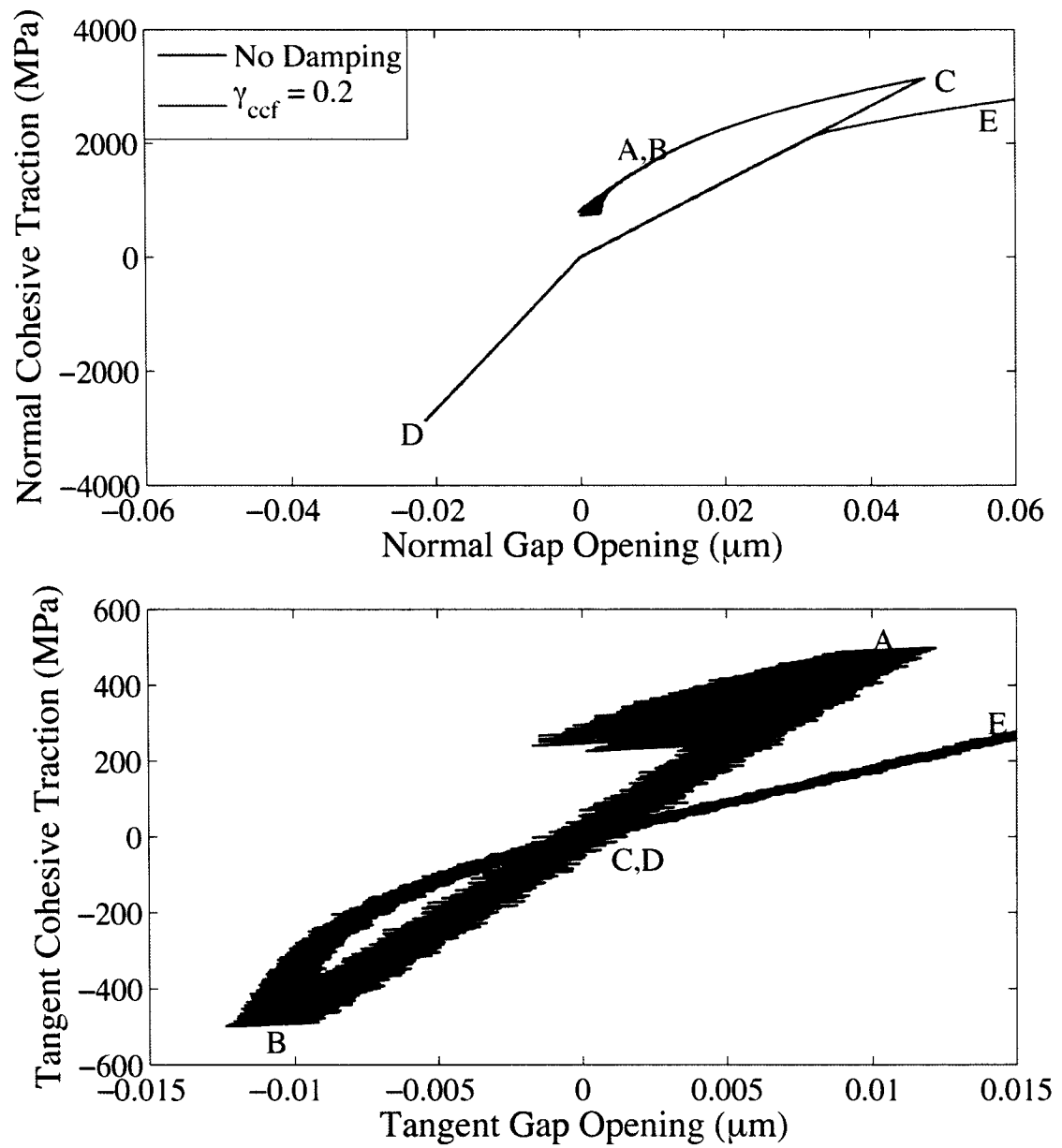


Figure 4.7: FTLF Linear Elastic Cyclic Traction Separation Plots

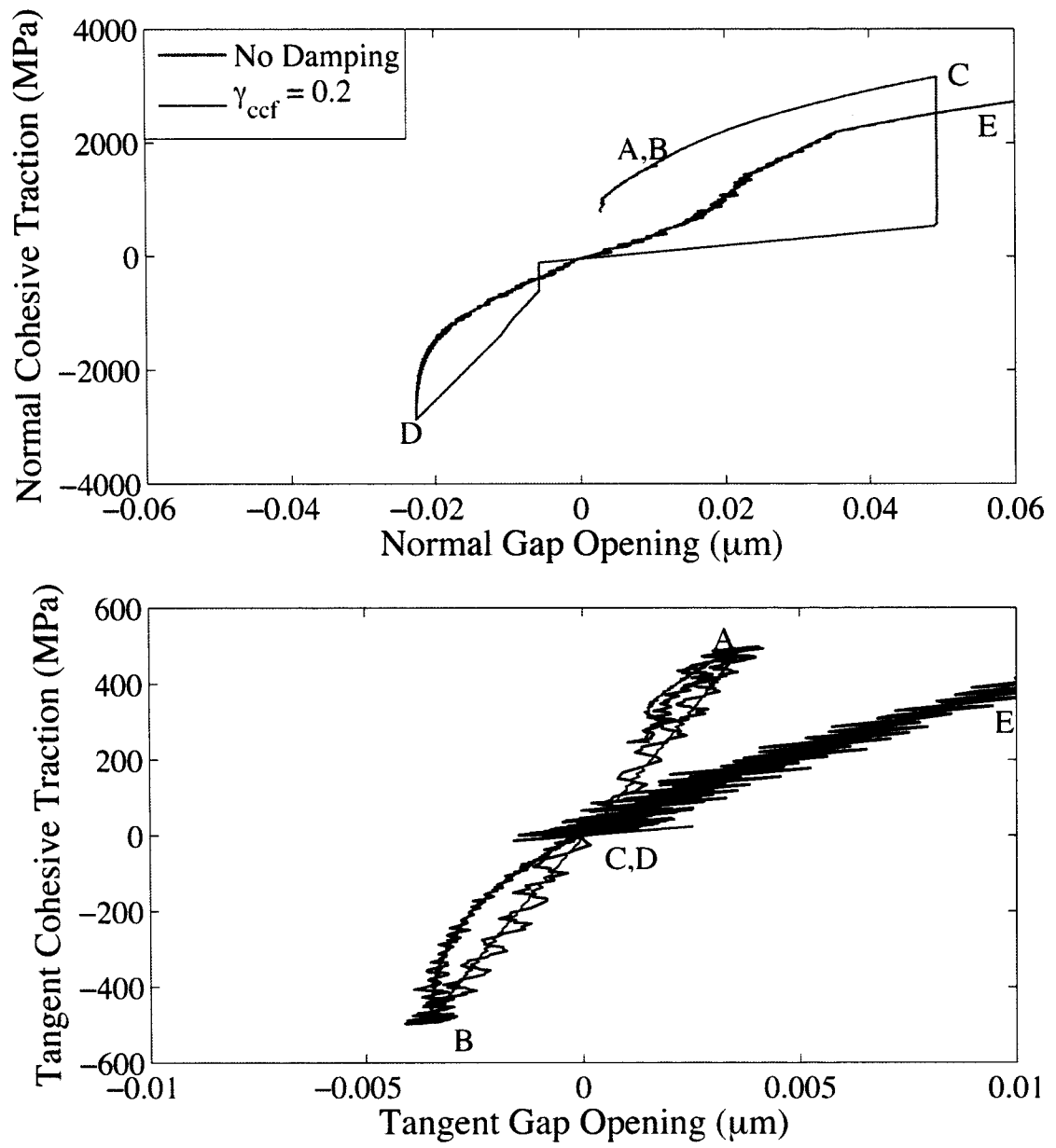


Figure 4.8: SBF Linear Elastic Cyclic Traction Separation Plots

4.2.3 Time Continuity

Through the previous two examples, the time continuity behavior of the CCF may be examined. Prior to a discussion of the data, the quantity by which time continuity is measured must be defined. To this end, the *net normalized nodal acceleration* (\mathbf{a}_{nnn}) is defined as:

$$\mathbf{a}_{nnn} = \frac{(\mathbf{f}_{cohesive} + \mathbf{f}_{bulk}) / (\frac{1}{2}m) - (\mathbf{f}_{bulk} + \mathbf{f}_{nc_bulk}) / (m)}{|\mathbf{f}_{cohesive}| / (\frac{1}{2}m)}$$

where:

m = nodal mass prior to duplication

$\mathbf{f}_{cohesive}$ = nodal force from cohesive stresses

\mathbf{f}_{bulk} = nodal force from connected bulk elements (post-duplication)

\mathbf{f}_{nc_bulk} = nodal force from connected bulk elements (pre-duplication)

(4.8)

For a perfectly time continuous method, \mathbf{a}_{nnn} should equal zero immediately after separation. Deviation from zero represents error due to time discontinuity. In the case of uniaxial strain loading, the CCF displays excellent time continuity characteristics as $|\mathbf{a}_{nnn}| < 10^{-8}$, which is essentially zero for this numerical setting, for all three coordinate directions. However in the case of multi-axial loading such as in loading path A in section 4.2.2, the values of \mathbf{a}_{nnn} are not zero.

Node	\mathbf{a}_{nnn} (X ₁ -direction)	\mathbf{a}_{nnn} (X ₂ -direction)	\mathbf{a}_{nnn} (X ₃ -direction)
1 (Lower)	-0.0400	-0.0185	-0.0446
2	0.0022	0.0136	-0.0298
3	0.0142	0.0028	-0.0124
4 (Middle)	0.0211	0.0109	0.0000

Table 4.2

From the results presented in Table 4.2, it is apparent that this CCF implementation does not guarantee time continuity for all meshes. In both the finite thickness layer and surface based formulations, the source of the discontinuity is the discrepancy between the nodal forces generated by cohesive tractions, and the nodal forces generated by the formerly connected bulk elements. Theoretically, the values of the nodal contributions that result from these tractions could be adjusted to provide better agreement with the pre-separation bulk element nodal forces. For instance, the nodal force components that result from the cohesive stresses could be scaled such that their values match the contributions of the disconnected bulk elements. This scaling could then be phased out as the separation process progresses. Another approach would be to match the nodal contributions from cohesive tractions on individual facets with the bulk element that is no longer connected to the node. Thus each facet would have individual scaling factors for each node that belongs to it. An alternative to the scaling factor approach is to ensure that the cohesive stresses do not drop immediately after separation. If Φ_1 is set such that the cohesive stress increases or remains flat during the initial phase of the separation process, the shock that occurs from time discontinuity will not have the ability to detrimentally affect the solution process (see Papoulia [24]). This is the method chosen for the analyses that follow. Note that the initial negative slope shown in section 4.2.1.2 is a result of a highly hydrostatic constraint condition (uniaxial strain). This condition is rare, and it will be shown that the cohesive stresses do increase after the separation process begins for the conditions present in the example problems.

4.3 Mesh Refinement Study on a Double Cantilever Beam

As a first step to simulating surface generation using the CCF in a realistic problem, a mesh refinement study has been performed for both the SBF and FTLF on a series of linear elastic double cantilever beams. Specifically, four double cantilever beam meshes with varying levels refinement were simulated as shown in Figure 4.9. These meshes are quasi-2D in that they contain only 1 layer of elements in the thickness direction, and are subjected to a plane stress boundary condition. Mesh generation was performed using the MGEN mesh generation code written by M.M. Rashid. The meshes are subjected to kinematic boundary conditions, such that the nodes at the ends of each beam are displaced away from the centerline, as illustrated in Figure 1.5. The quantitative details of each mesh are presented in Table 4.3.

	Coarse0	Coarse	Medium	Fine	V. Fine
Nodes	3434	3434	5322	8418	22654
Elements	1600	1600	2544	4092	11152
Smallest Element	0.4 mm	0.4 mm	0.2 mm	0.1 mm	0.05 mm
Mass Scaling	No	x100	x100	x100	x100
Number of Active Separating Facets	1-2	1-2	1-2	2-3	4-5

Table 4.3: Double Cantilever Beam Mesh Information

As stated in Table 4.3, mass scaling of 10^2 is applied to the meshes to increase the maximum stable time step by a factor of 10. The results for the unscaled problem are not shown, but they did indicate that there was no significant discrepancy between the scaled and unscaled simulations. While the CCF framework does allow for crack extension along any facet (i.e. any direction), for the purposes of this particular analysis, crack extension was confined to the centerline of the mesh. An opening velocity of 50 mm/s

(increased linearly from zero over 0.01 s) was specified. These simulations were run until the crack reached the end of the refined zone, which yields about 20 mm of crack growth over the duration of the problem.

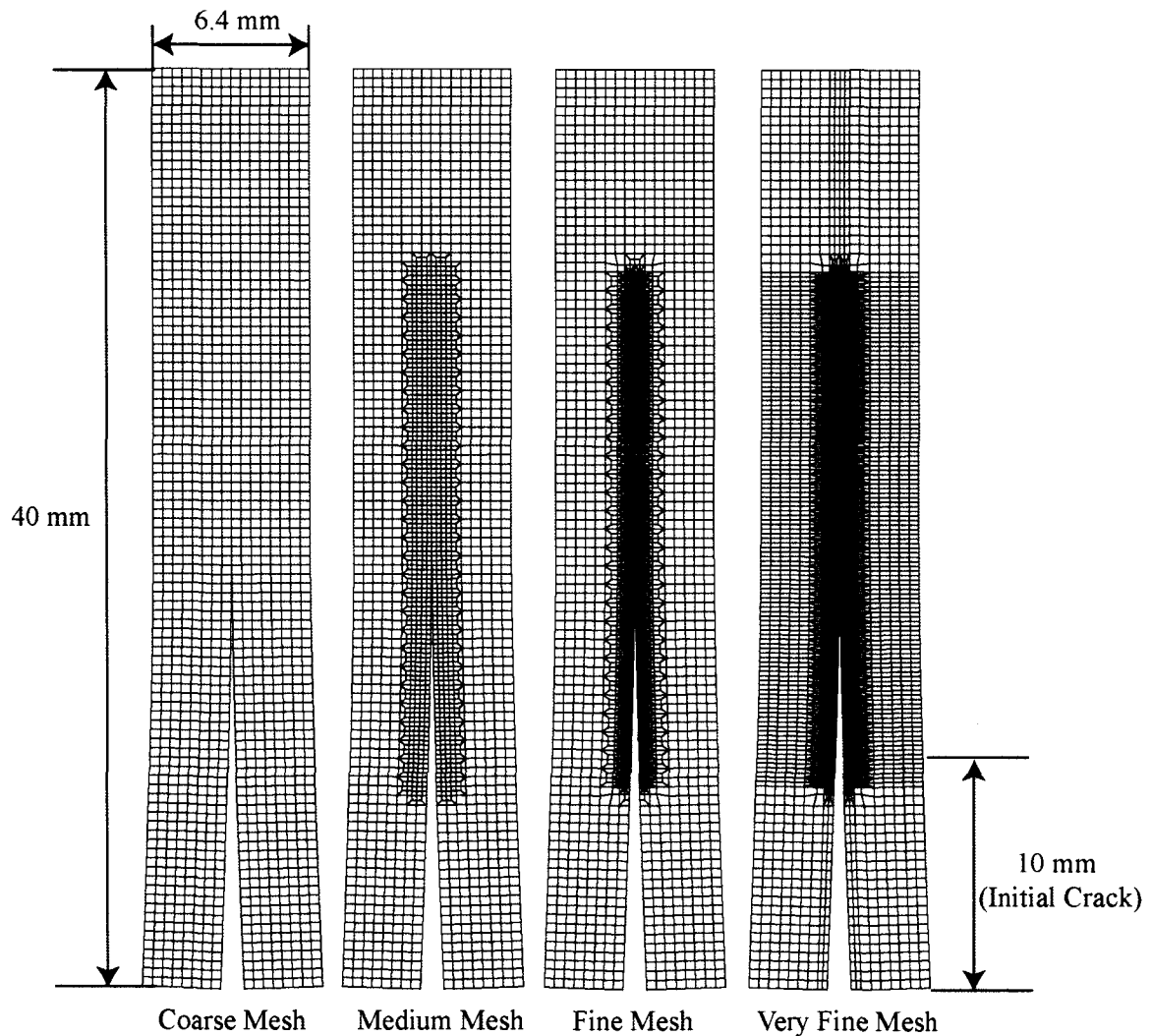


Figure 4.9: Deformed Double Cantilever Beam Meshes

The results of these analyses are presented as plots of the *opening force vs crack mouth* opening displacement (*CMOD*) and *Rate of Energy Dissipation* (i.e. *G*) vs *Crack Extension*. The *opening force* and *CMOD* are readily available as output from the finite

element code. The rate of energy dissipation is calculated by taking the total energy dissipated over a period of time, and dividing it by the amount of new surface area created over that period of time. The size of the time interval that is used is about 0.2 ms.

This procedure may be expressed as:

$$G(t) = \frac{EnergyDissipated(t + 0.1ms) - EnergyDissipated(t - 0.1ms)}{SurfaceArea(t + 0.1ms) - SurfaceArea(t - 0.1ms)} \quad (4.9)$$

The energy dissipated is calculated by subtracting the kinetic and elastic strain energies from total energy input to the system. The new surface area generated is calculated by summing the area of all CCF facets multiplied by their separation coefficients. Thus an unruptured ($s=0$) facet will contribute zero area, and a fully ruptured ($s=1$) facet will contribute all of its area to the summation. Finally, crack extension is calculated by dividing the new surface area generated by the thickness of the specimen.

Figure 4.10 and 4.12 plot the *Force* vs *CMOD* for the finite thickness layer and surface based formulations respectively. In order to smooth the force-time history, a 4th order low-pass Butterworth filter with a cutoff frequency of 10,000 Hz was applied. Observe that the force data exhibit large oscillations that decrease as the mesh is refined. This decrease is explained by considering that a decrease in the size of a facet leads to a smaller cohesive force contribution, in addition to increasing the number of facets that are actively in the process of separating at one time. The reduction in force is important, because loss of cohesive traction occurs rather abruptly. Thus the loss of traction from a smaller facet delivers a smaller overall shock to the system. Furthermore, an increase in the number of facets that participate in the rupture process allows a smoother transition to

occur, as the loss of traction in a trailing facet will be less “violent” due to lower stress/strain in adjacent bulk elements.

Figures 4.11 and 4.13 plot the *energy dissipation rate vs crack extension*. As expected from the double cantilever beam geometry, the dissipation rate is nearly constant throughout the extension process. The constant dissipation rate is a result of a constant *cohesive stress/gap opening* relation, as follows. In the case of linear elasticity, the rupture function fixes the cohesive stress/gap opening relation to be constant for all loading conditions. In other words, the *cohesive stress vs gap opening* plots will look like Figures 4.2 and 4.3 in all cases. The area under the cohesive stress/gap opening curve is equal to the dissipation rate in a cohesive zone method, but is only a close approximation to the dissipation rate for the CCF. This is a result of the manner in which the cohesive stresses are applied for the FTLF (not only tractions are applied!), and the potential of the SBF to dissipate energy under unload/reload. In any case, the values of G for the finite thickness layer and surface based formulations are 0.55 and 0.56 kJ/m² respectively.

Figures 4.10-4.13 indicate that the “fine” and “very fine” meshes have converged. Since the material is linear elastic, LEFM along with elementary beam-theory considerations may be used to determine the force (P) and displacement ($CMOD$) given the energy dissipation rate (G) and crack size (a):

$$P = \sqrt{\frac{G B E I}{a^2}} \quad (4.10)$$

$$CMOD = \frac{P a^3}{E I} \quad (4.11)$$

where (I) is the second moment of area, (a) is the crack length, and (B) is the thickness of the beam. Since LEFM assumes that the crack advances under $G=G_c$, and an estimate of G_c is available from figures 4.11 and 4.13, the value of P may be calculated for a range of crack lengths (a) using equation 4.10. Once P is known for values of (a), the $CMOD$ is calculated through equation 4.11. Now that P and $CMOD$ are defined, the LEFM solution is plotted in figures 4.10 and 4.12 as the dotted black line.

A significant result of this set of simulations is that the mesh convergence may be linked to the number of active facets (i.e. facets that are actively undergoing the separation process at the same time). The coarse and medium meshes (1-2 active facets) remain far from the converged solution, while the fine mesh (2-3 active facets) and the very fine mesh (4-5 active facets) appear to have converged.

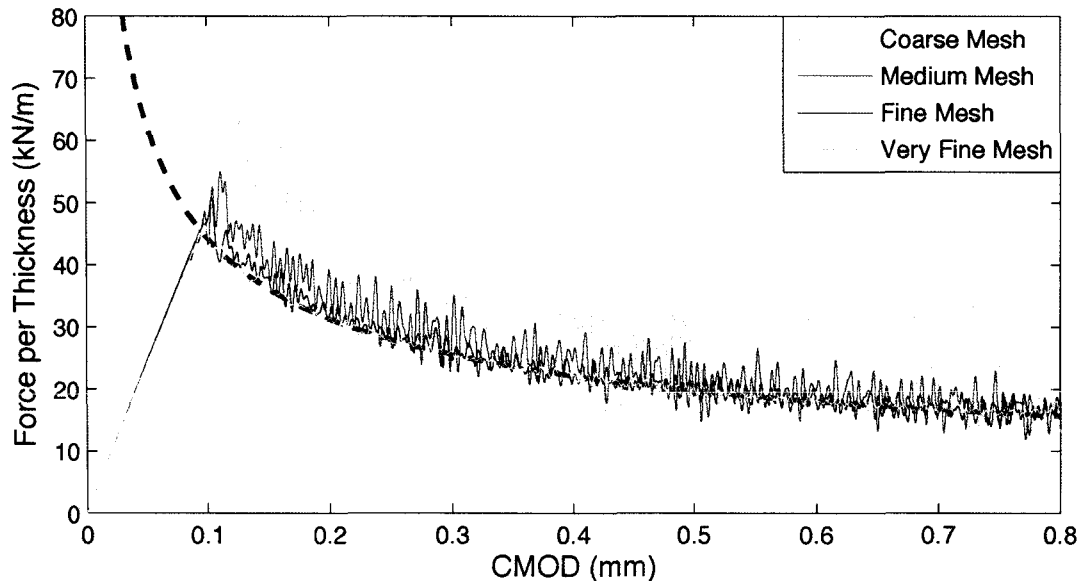


Figure 4.10: Opening Force (LPF @10,000 Hz) per unit Thickness vs CMOD for Linear Elastic Double Cantilever Beam (Finite Thickness Layer Formulation)

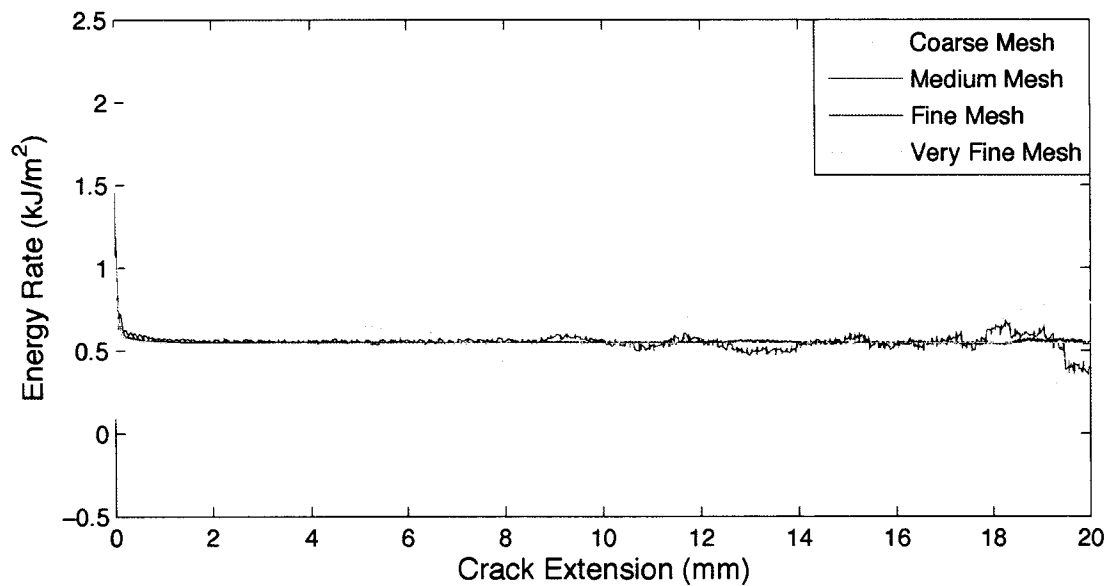


Figure 4.11: Rate of Energy Dissipation vs Crack Extension for Linear Elastic Double Cantilever Beam (Finite Thickness Layer Formulation)

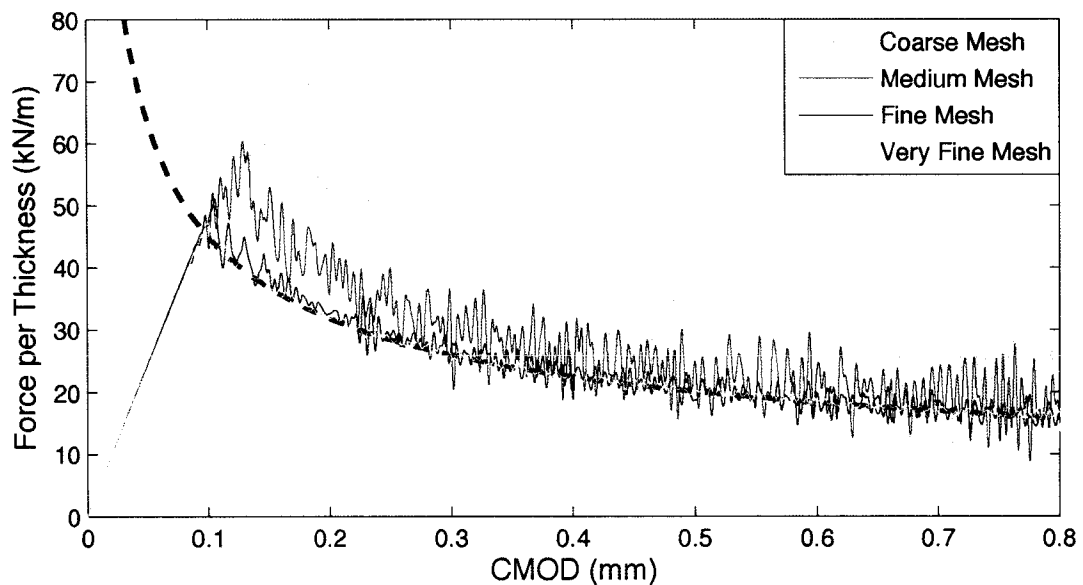


Figure 4.12: Opening Force (LPF @10,000 Hz) per unit Thickness vs CMOD for Linear Elastic Double Cantilever Beam (Surface Based Formulation)

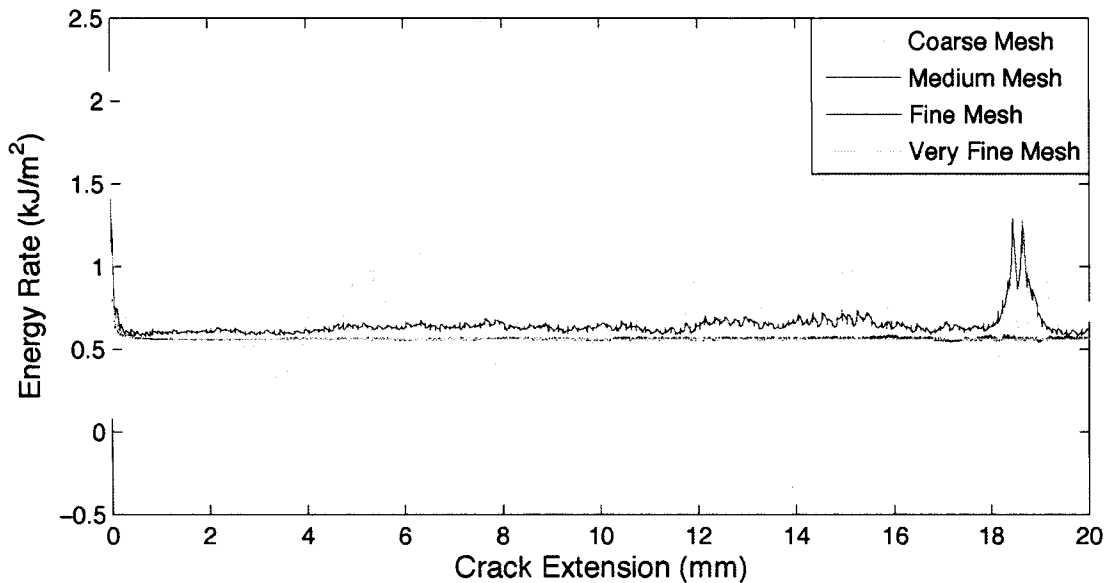


Figure 4.13: Rate of Energy Dissipation vs Crack Extension for Linear Elastic Double Cantilever Beam (Surface Based Formulation)

4.4 Mesh Refinement Study on a Periodic Plate

The previous problem showed that the CCF exhibits mesh convergence when modeling a linear elastic double cantilever beam. However, the question of whether this implies that convergence may be assumed for unstable crack growth (displacement-controlled DCB exhibits stable crack growth), and the presence of a more complex material behavior, remains. To further explore mesh convergence of the CCF, four plates consisting of a 21-6-9 steel modeled using a Gurson dilatant plasticity constitutive model, under periodic boundary conditions were simulated. The problem geometry consists of a 24 mm square plate of 0.3 mm thickness containing an 8 mm slit through the bottom portion of the vertical centerline. The baseline mesh is a 30x30x1 arrangement of elements. Mesh refinement is limited to the region surrounding the vertical centerline (crack path) of the

plate as illustrated by the partially deformed meshes in Figure 4.14. A summary of the mesh configurations is given in Table 4.4.

	Coarse0	Coarse	Medium	Fine	V. Fine
Nodes	1922	1922	2526	3730	6134
Elements	900	900	1200	1800	3000
Smallest Element	0.8 mm	0.8 mm	0.4 mm	0.2 mm	0.1 mm
Active Facets	0-2	0-2	1-10	4-many	10-many

Table 4.4: Periodic Plate Mesh Information

The boundary conditions are such that the initial configuration of the BVP represents a single cell (24mm x 48mm) within a periodic array of through-thickness cracks (16 mm in length) in an infinite plate. This situation is emulated by restricting surface normal motion along the top/bottom of the mesh. Then, the left and right boundaries of the mesh are subjected to a normal velocity of 0.02 m/s that is increased from zero over 0.01 seconds. The through-thickness deformations are unconstrained, thus the plate is considered to be in plane stress. Once again a mass-scaling factor of 100 was used, and was determined to have little effect on the solution.

To consider the effect of extending the crack in the plate problem, imagine two linear elastic plates subjected to equal boundary displacements. The plates differ in that plate A contains a short crack, and plate B contains a long crack. For this particular geometry and boundary conditions, it can be shown that plate B will have a higher stress intensity factor than plate A at the same level of remote displacement. This means that once the critical stress intensity factor is reached and crack extension commences, the stress intensity only increases, even with no further increase in remote displacement. Therefore this problem is considered to exhibit unstable crack growth.

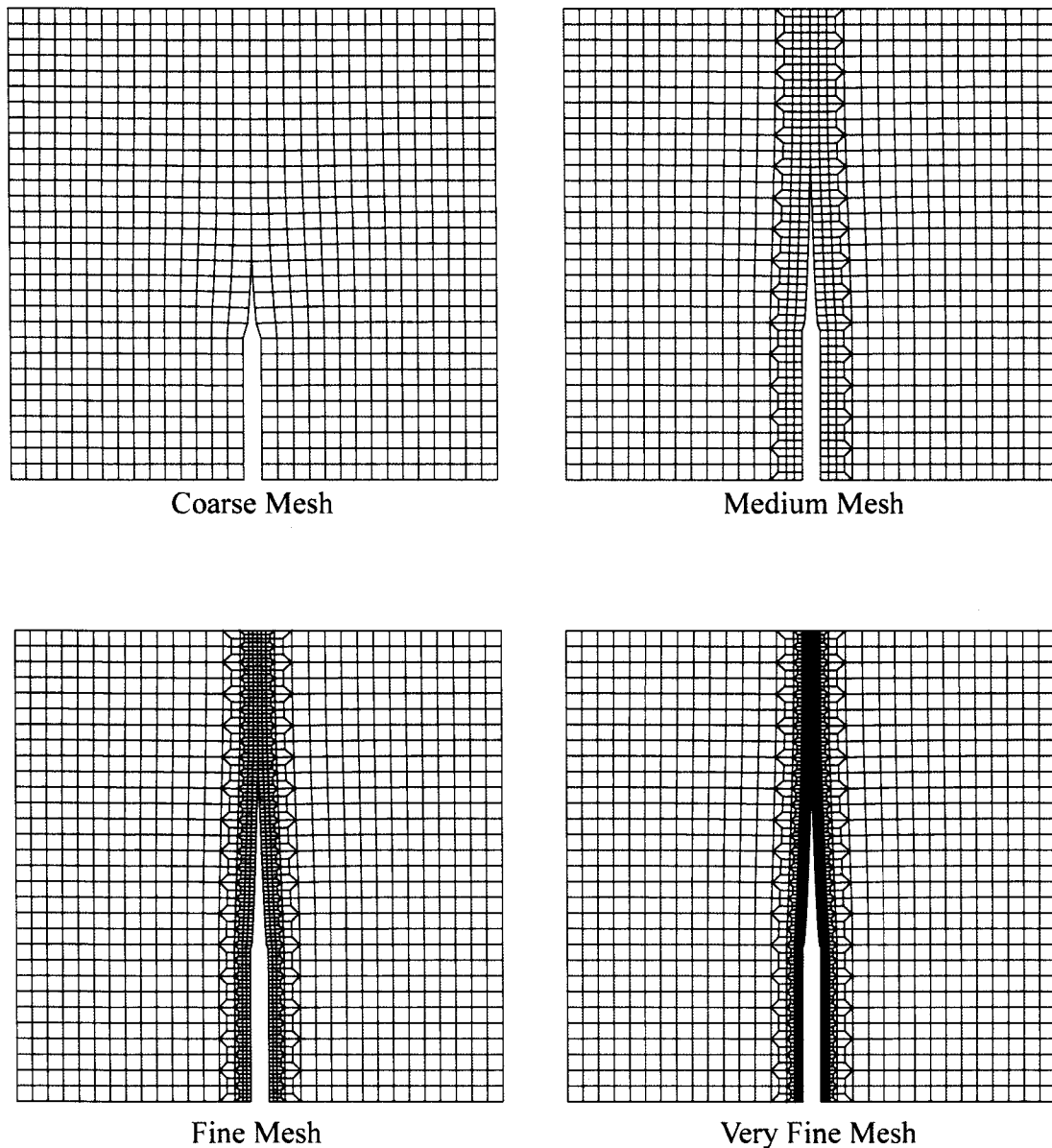


Figure 4.14: Illustration of Periodic Plate Meshes

Figure 4.15 shows a plot of the applied force versus time for the four levels of mesh refinement. In comparing this plot to the analogous plots (4.10 and 4.12) for the DCB problem, it should be borne in mind that the present problem is far more complex than the earlier one. Not only is the material response given by an elaborate dilatant plasticity model, but also dynamic crack growth occurs. Nonetheless, the medium, fine, and very

fine meshes appear to be moving towards uniform convergence over the entire time period.

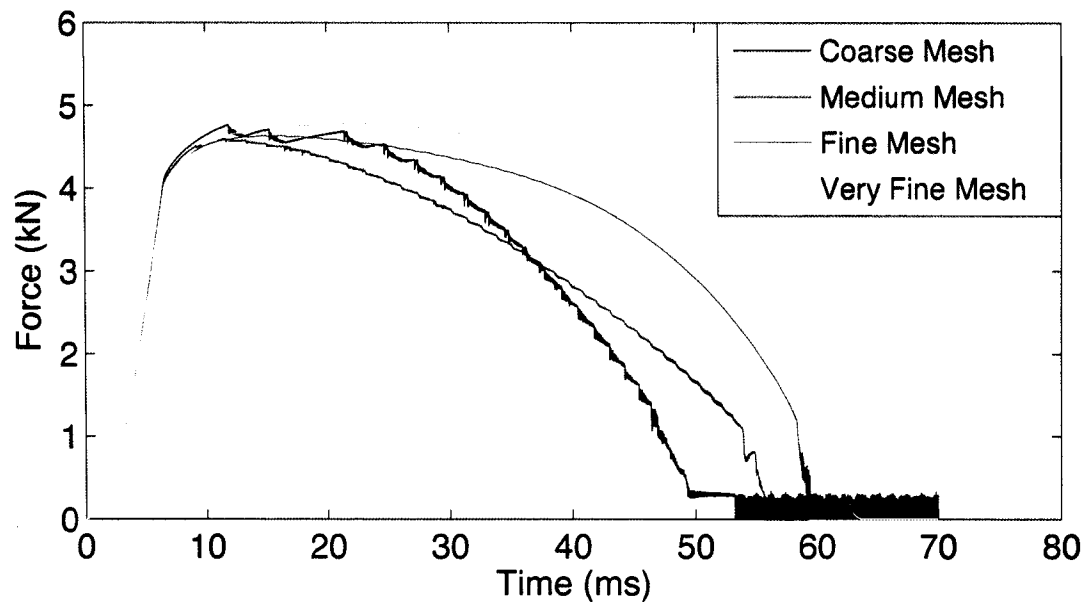


Figure 4.15: Periodic Plate – Force vs Time

Figure 4.16 shows the rate of energy dissipation plotted against normalized crack extension. The rate of energy dissipation is calculated using the relation in equation 4.9. The normalized crack extension is simply the crack extension normalized by the total possible length of the crack. Thus after the crack has propagated all the way through the plate, the normalized crack extension is equal to unity. Over the first portion of the normalized crack extension range, the curves do not display a consistent trend that would indicate convergence. However, after 0.6 normalized crack extension the curves show good correlation. Note that the coarse mesh is actually on top of the fine and very fine meshes over this range, while the medium mesh is slightly offset.

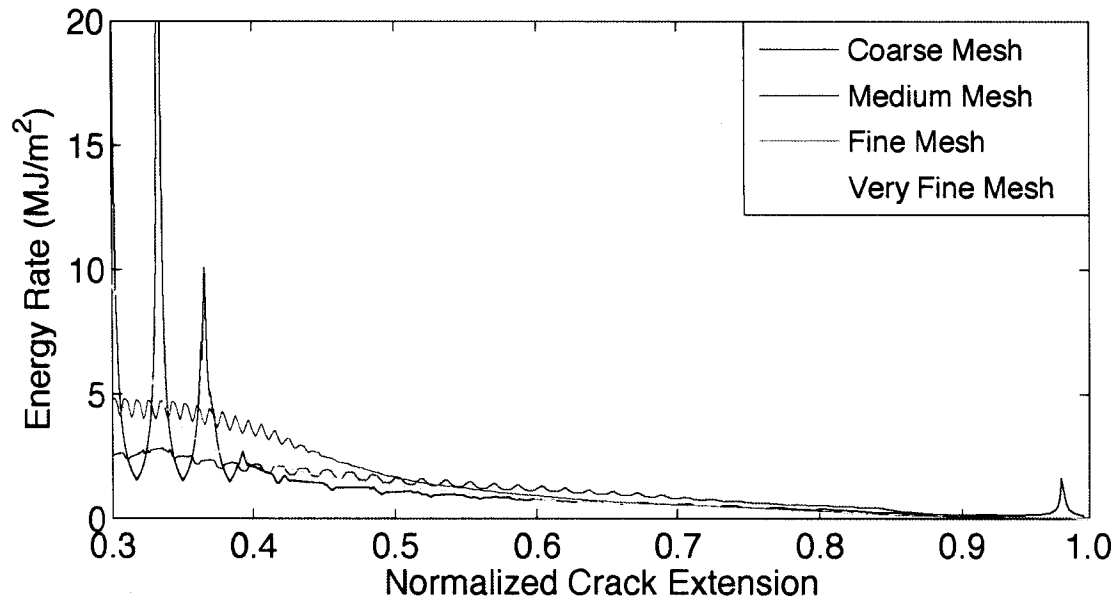


Figure 4.16: Periodic Plate – Energy Rate vs Normalized Crack Extension

Figure 4.17 presents a plot of crack velocity against normalized crack extension. In contrast to the previous figures, the crack velocity plot shows strong indications of mesh convergence over most of the crack extension. Notice the sharp spikes in the crack velocities taken from the coarse and medium meshes. These spikes indicate that the separation process does not have sufficient resolution to present a smooth transition as in the case of the fine and very fine meshes. The data indicates that the fine and very fine meshes have approached a converged solution until a normalized crack extension of about 0.82. As the zone of separating facets reaches the boundary of the plate, the crack velocities lose their repetitive pattern and fluctuate wildly. This event can also be observed in figure 4.15 as the force drops abruptly as the plate approaches complete separation. This illustrates a consistent problem that the CCF appears to display. When a near-incompressible material is specified along with the constant volume assumption described in section 3.1.3, the CCF exhibits unstable behavior if there are only a small number of partially separated facets remaining. In other words, the CCF may not handle

complete separation well when an incompressible material is used. However the specification of a moderate amount of cohesive damping as defined in section 3.2.5 typically stabilizes the problem.

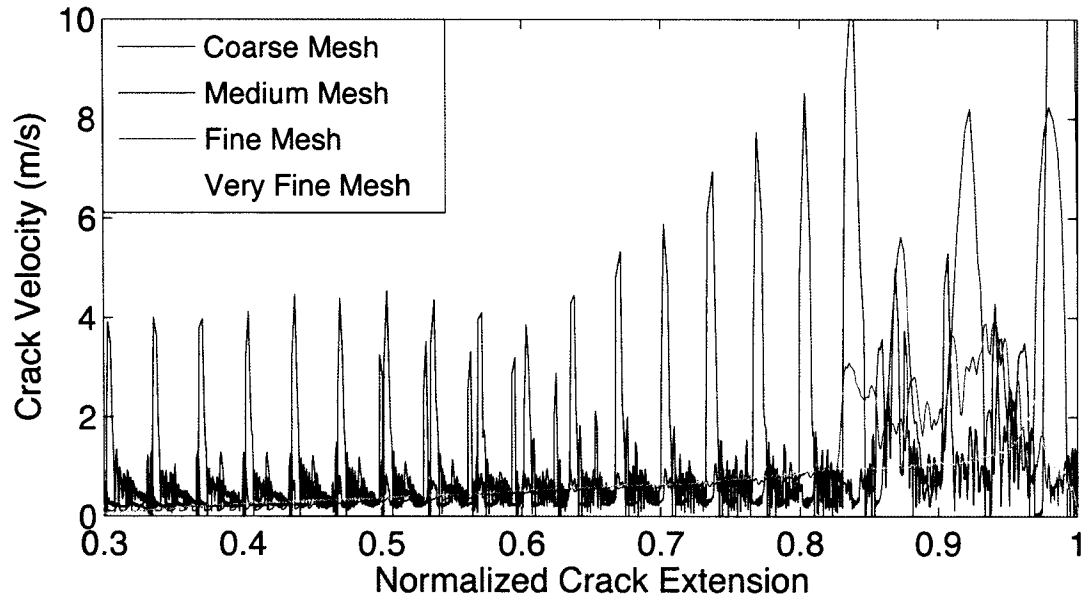


Figure 4.17: Crack Velocity vs Normalized Crack Extension

4.5 CCF Gurson Model Calibration

In the previous section, a plate of 21-6-9 steel was modeled using a Gurson type dilatant plasticity model. Prior to this modeling effort, constitutive parameters were calibrated using experimental data, to ensure sufficient accuracy. One common method for calibration of elastic-plastic constitutive models is to perform experimental uniaxial tension tests, then fit the data with the computed response under a one-dimensional uniaxial stress assumption. In many cases, rather than using a numerical algorithm written specifically to enforce the one-dimensional uniaxial stress assumption, a simple finite element analysis with only one element and appropriate boundary conditions is used to fit the data. These approaches work well as long as the one-dimensional

assumption is valid. Upon accumulating large amounts of plastic strain, the uniaxial specimen may exhibit strain localization and necking, thus invalidating the one-dimensional assumption. This shortcoming is compounded when modeling material separation, as separation features do not begin to appear until after the onset of necking in ductile metals. Therefore, to utilize the Gurson model in a CCF surface generation problem, another method of calibration must be used.

The first step in the method for constitutive calibration of the Gurson model is to determine baseline elastic-plastic parameters, while keeping the void volume fraction equal to zero (Recall that the Gurson model is equivalent to J2 Plasticity if $f=0$). This baseline calibration may be done using the simple one-dimensional assumption mentioned above. Once a suitable set of plasticity parameters is found, the parameters governing nucleation of voids must be determined. Again, the one-dimensional assumption is adequate for this purpose. Once plasticity and void nucleation parameters are found that accurately model the uniaxial test prior to strain localization, the one-dimensional model must be put aside in favor of a more complicated tool.

The next step in the calibration is to adjust the nucleation parameters such that strain localization and necking occur at the appropriate point in the loading. To accomplish this phase of the calibration, an actual uniaxial tensile test must be simulated. Logically, the specimen dimensions that provided the test data should be used. Once the nucleation parameters have been adjusted, the rupture parameters (Φ_1 , Φ_2) are calibrated. The value of Φ_1 should ideally be determined by selecting a value of the rupture function in the

necking region after significant necking has occurred, although the amount of necking at which this should be done somewhat arbitrary. Note that because the Gurson model is capable of softening, and the finite element code used here has no re/meshing capability, it is possible that localization may occur in the bulk elements. In order to ensure that localization initialized instead across a CCF facet (through gap opening), the value of Φ_1 can be set artificially low so that the facet is activated prior to softening. In conjunction with this lower Φ_1 , the stress reduction factor may be adjusted so only small amounts of stress reduction occur over the initial stages of the separation process. These small stress reductions ensure that the closing tractions are reduced, thus forcing localization to occur across a facet.

Further adjustments to the rupture parameters and the stress reduction factor are done through correlation with data from a series of 3-point bend specimens. The 3-point bend specimen is a test designed to quantify fracture resistance, and thus is well suited to calibrating the parameters that govern the fracture process in the CCF. Using data plots of *applied force* vs *CMOD*, the value of Φ_1 and the initial stress reduction are adjusted. If the separation results in a premature drop in applied top force, then either the value of Φ_1 must be increased, or the amount of stress reduction applied must be reduced. Next, the value of Φ_2 and the remainder of the stress reduction factor (recalling that the stress reduction factor is a function of the separation coefficient) are calibrated using the experimental force vs *CMOD* data plots. After this, fine-tuning of void nucleation and rupture parameters is done until satisfactory results are obtained.

4.6 Simulation of a Uniaxial Tension Test

The uniaxial tension specimen is a cylindrical bar of 1.42 mm radius, and an effective length of 12.7 mm. (Effective length simply refers to the extensometer gauge length used to measure strain.) An image of the mesh after necking has occurred is shown in Figure 4.18. Note that the image shows a complete specimen, while the simulation actually consisted of a quarter of the specimen with fixed surface normal displacements to provide symmetry boundary conditions. The mesh consists of 4875 nodes and 4128 elements, with separation being restricted to the mid-plane of the specimen. In order to trigger necking at the mid-plane, the radius of the center band of nodes was reduced by 2%. The specimen is loaded at its ends with a specified velocity of 0.1 m/s, which rises from zero over 0.1 seconds.

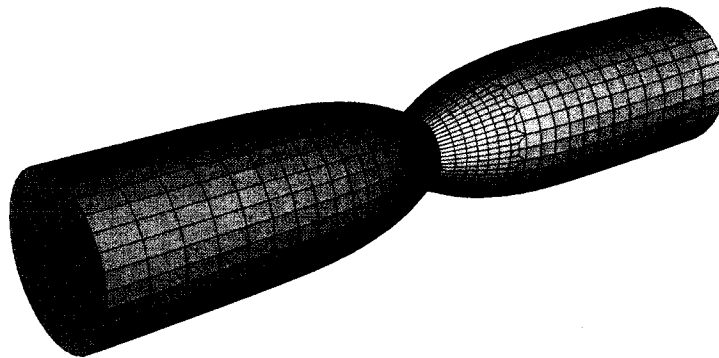


Figure 4.18: Uniaxial Tension Test Simulation After Necking Occurs

In addition to the necking evident in figure 4.18, uniaxial tension specimens that fracture by void growth and coalescence are expected to rupture from the center outward. This is attributed to a high rate of void growth in the center of the specimen, which in turn is a result of the high tensile pressure that necking induces. This feature is modeled by the CCF Gurson implementation as shown in Figure 4.19, which shows cross sections of the

specimen at different stages of separation, as well as the stress-strain plot that includes 4 experimental data curves (blue lines). The letters on the plot indicate the location of each stage. Figure 4.19 clearly illustrates that the separation process begins in the center of the specimen and moves towards the outer radius. Note that the specimen remains partially connected longer than the data suggest. This is a result of the lack of mesh refinement, which in this case leads to poorly shaped bulk elements along the outer surface of the cylinder. Because the CCF inherently links the rupture material to the bulk element, the separation process is significantly affected by these poorly shaped elements. This is further illustrated by the plots of *cohesive traction vs gap opening* for separating facets at different points along the radius. Remembering that the cohesive traction does not constitute the totality of the rupture model, as cohesive stresses are also applied in Λ , figure 4.20 illustrates that the traction separation curves gradually change as the surface of the cylinder is approached. Specifically, the material under less confinement (near the outer surface) remain connected over a greater range of gap openings, which results in a higher “fracture toughness” (i.e. higher required energy to generate a surface). However, the outer layer of rupturing facets exhibits a substantial change in shape from the next facet inward.

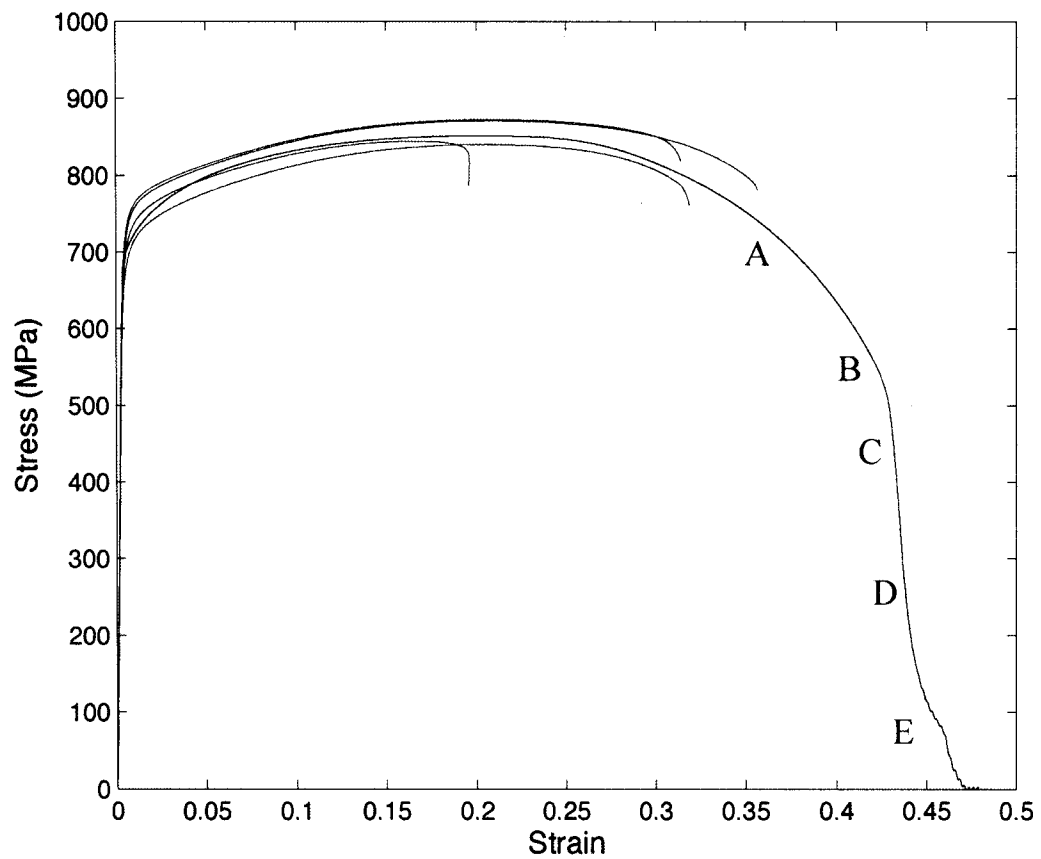
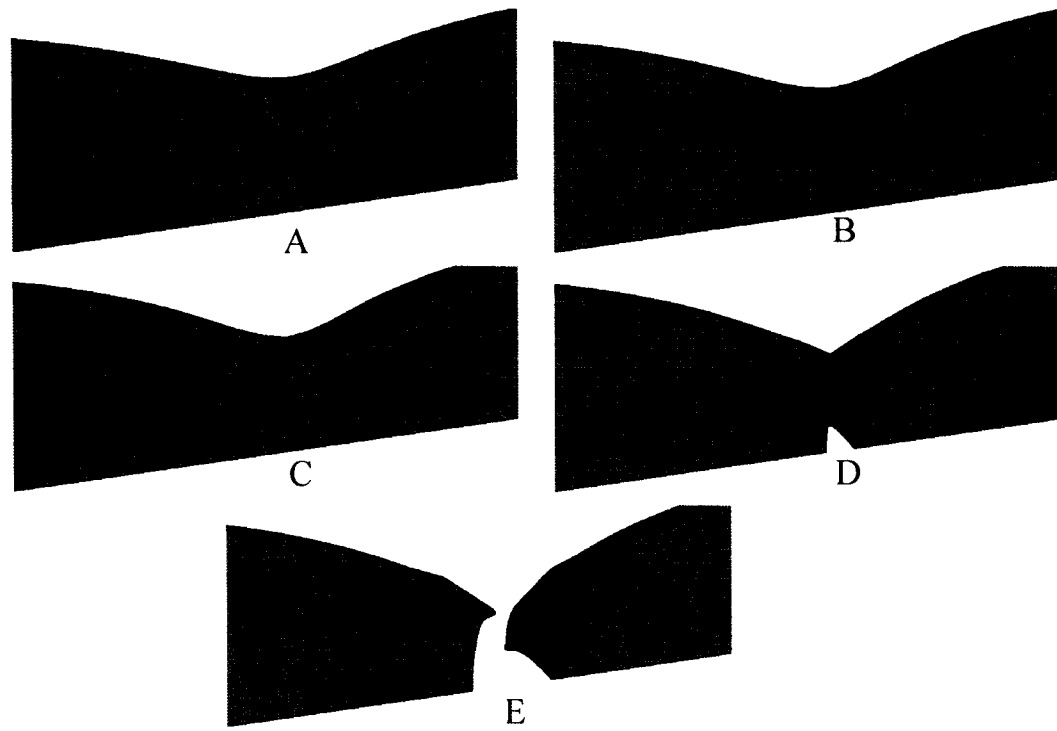


Figure 4.19: Failure of a Uniaxial Tension Test Specimen. Necked Meshes with Cohesive Elements in Red, and Stress Strain Plot including Experimental Data.

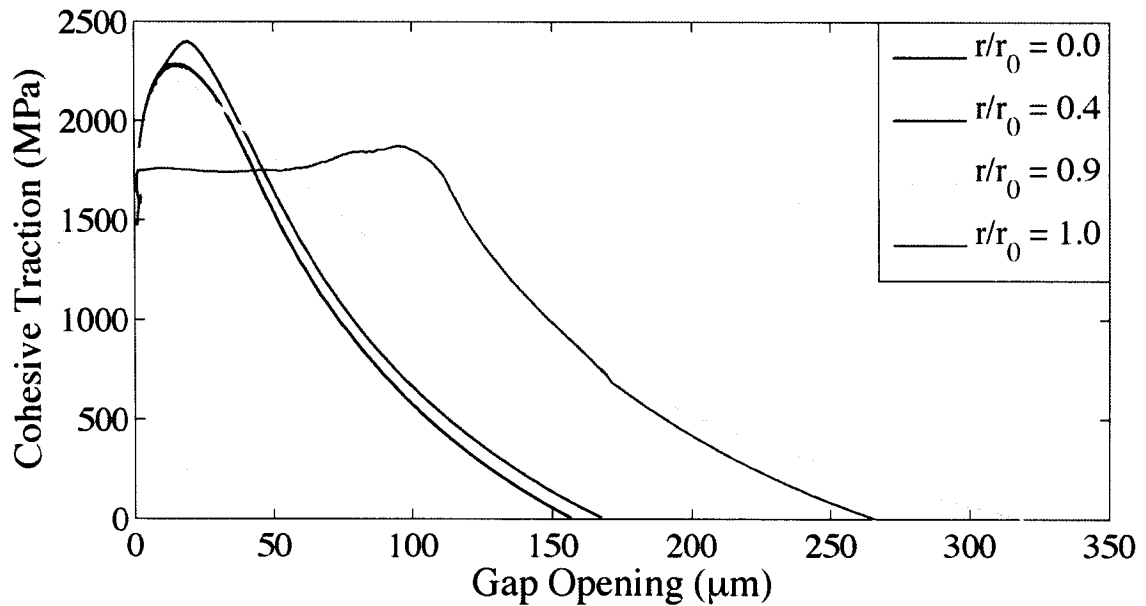


Figure 4.20: Uniaxial Tension Test - Cohesive Traction vs Gap Opening at Various Radii

4.7 Simulation of a 3-Point Bend Specimen

As mentioned previously, data from three separate 3-point bend specimens of 21-6-9 steel has been obtained courtesy of B.P. Somerday (Sandia National Laboratories). The test data from the 3-point bend tests have been used in the manner described in section 4.5 to calibrate the Gurson constitutive parameters as well as the rupture parameters.

Note that the specimens were taken from different locations in a rolled billet, thus varying material properties are exhibited. Accordingly and for simplicity, the constitutive parameters were calibrated to provide an average response. The 3-point bend test involves pre-cracking the specimen at mid-span, then applying a velocity at mid-span while the specimen is simply supported. This is summarized in figure 4.21.

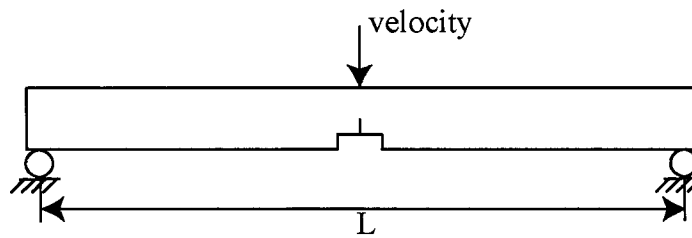


Figure 4.21: Schematic of 3-Point Bend Test

The meshed 3-point bend specimen is illustrated in figure 4.22 along with relevant dimensions. From the side view, the clip gauge gap is visible along the bottom of the specimen. A clip gauge was placed between the opposing faces on each side of the gap to measure *CMOD*. For consistency, the *CMOD* values produced from the simulation are measured from equivalent locations. Typically, in experimental 3-point bend specimens side notches are machined along the mid-span of the specimen to ensure that crack propagation occurs along a vertical path, and also to promote plane strain conditions at the crack tip. These notches can be seen from the top view of the mesh. Geometry generation and meshing was performed with the commercial mesh generator TrueGrid©. The mesh is refined near mid-span, and consists of 26,783 nodes, 23,820 elements with a minimum element dimension of 0.006 mm.

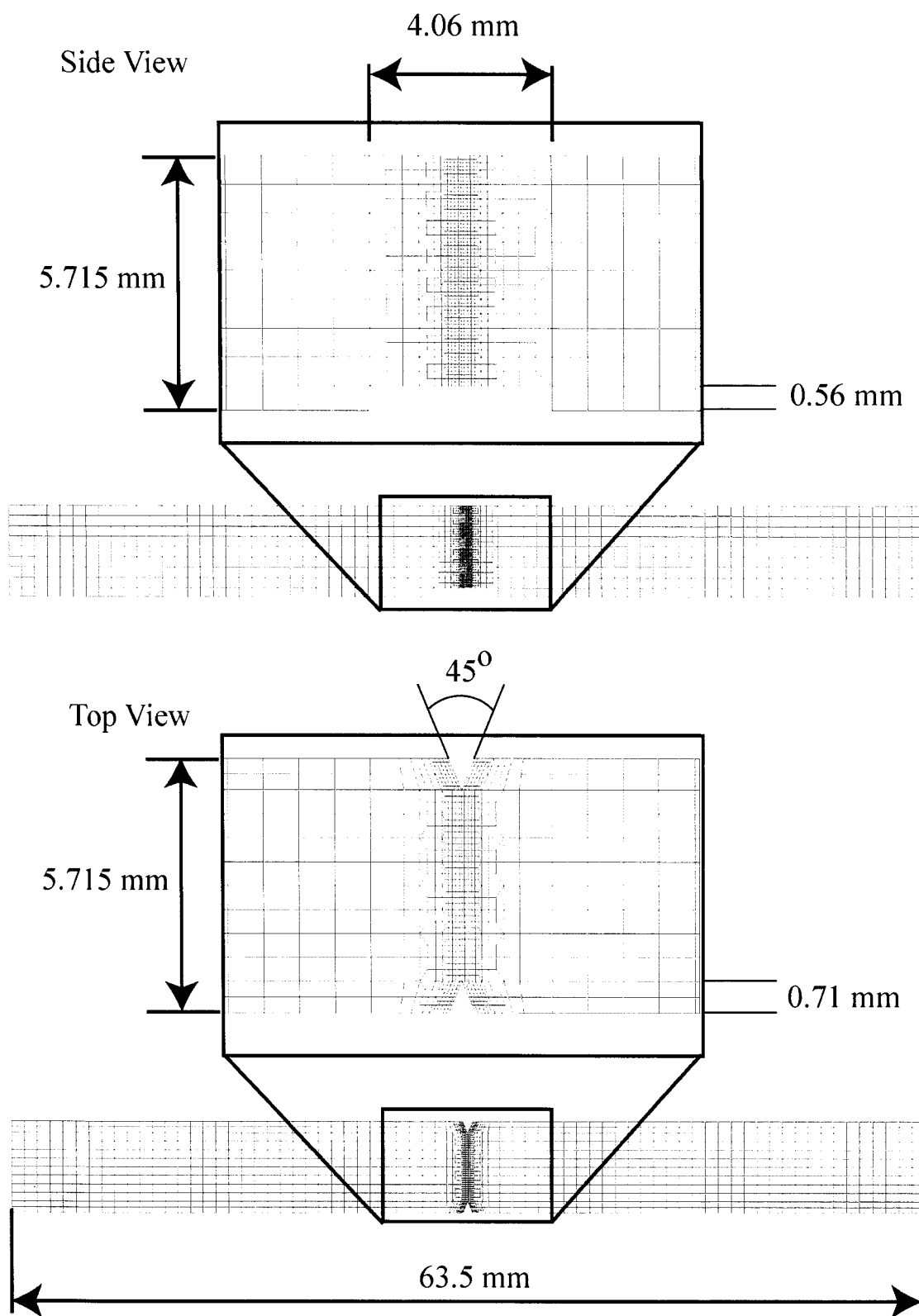


Figure 4.22: Mesh Used in Simulation of 3-point Bend Test

A pre-crack of length 2.58 mm, which runs through half the specimen height, is specified, and the 3-point bend mesh is loaded in a similar manner to that shown in figure 4.21. At the left and right extremes of the mesh, a set of nodes (4 nodes high and thru the thickness of the beam = 42 nodes) is given a fixed kinematic boundary condition in the vertical direction. A set of nodes (6 nodes wide and thru the thickness of the beam = 273 nodes) along the top mid-span surface of the beam is then subjected to a velocity boundary condition in the negative vertical direction of 0.05 m/s. A mass-scaling factor of 100 was used to increase the minimum stable time step by a factor of 10.

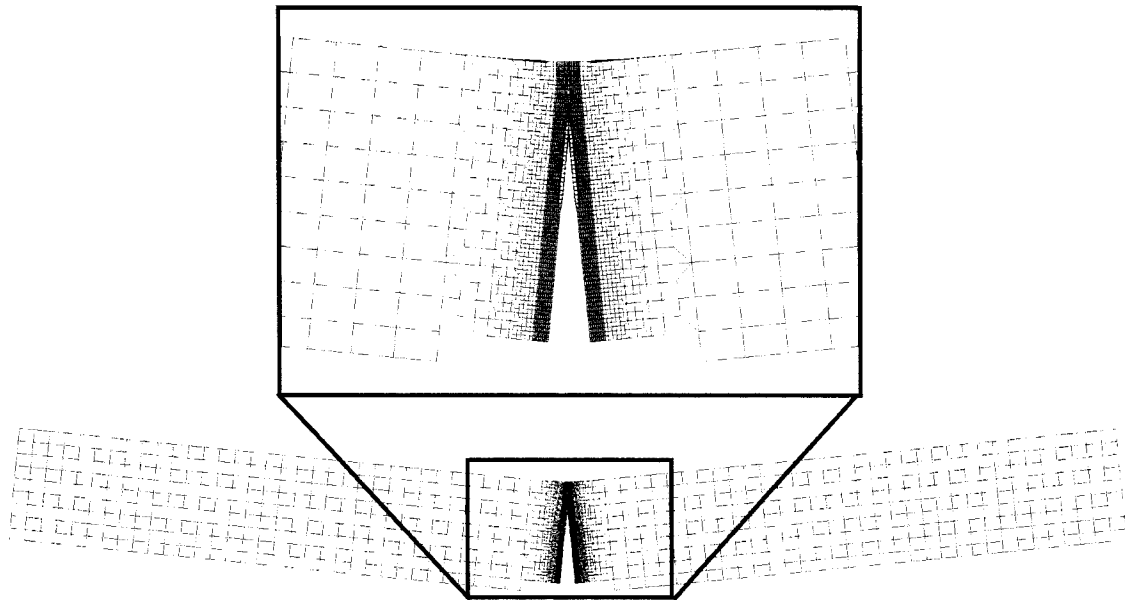


Figure 4.23: Deformed Mesh From Simulation of 3-point Bend Test

Side view images of the deformed mesh are shown in Figure 4.23. Figure 4.24 provides a cut-away view of the separation plane near the end of loading, with the active facets colored according to the current value of the separation coefficient. The color scheme is such that red indicates near full separation ($s=1$) and blue indicates minimal separation. Note is that the number of active facets along the general direction of crack propagation

is about 4. From the results of the preceding mesh refinement studies it is inferred that the mesh is suitable for the problem. Note that the shape of the separation zone is not what one might expect. Specifically, as in the uniaxial tension test, the hydrostatic stress should be much higher at points in the interior of the specimen, than on the surface. This situation would typically result in a curved zone of facets that lead at the center (concave down-“tunneling”). However, figure 4.24 clearly indicates a mildly opposite situation, with a curved zone of facets that lead at the edges (concave up). The reason for this is that the notches that are machined into the sides of the specimen create a stress concentration near the outer surface of the specimen, thus the material in this region is far from plane-stress, as it is far from the specimen faces. This is confirmed by images of the specimen, in which the specimen was cut along the separation plane after testing to reveal the shape of the rupture front.

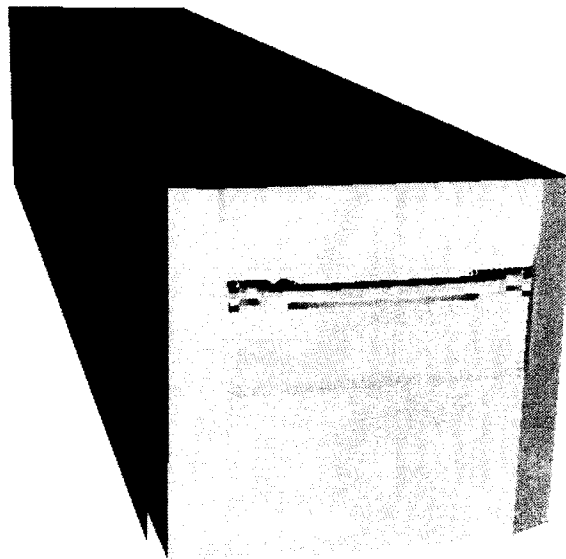


Figure 4.24: Rupture Zone Taken From the Simulation of a 3-point Bend Test

Figure 4.25 shows a plot of the applied *top force* vs *CMOD* for both the simulation and experiment. The figure suggests that the CCF together with the Gurson dilatant plasticity model is capable of accurately modeling ductile rupture in the material.

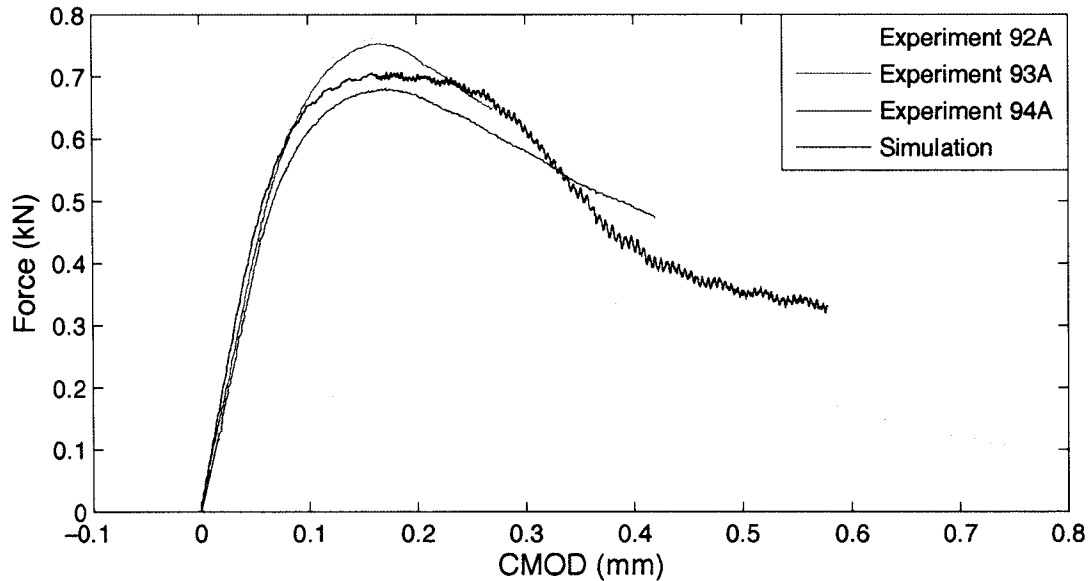


Figure 4.25: 3-Point Bend Simulation – Applied Top Force vs. CMOD

Figure 4.26 plots the energy dissipation per crack area (rate of energy dissipation) against the crack extension length. This curve shows that the dissipation rate is initially large, decreases to a nearly constant level, and then begins to rise again. The drop in dissipation rate is typical of 3-point bend tests on ductile material; however, the rise in dissipation rate is not commonly observed in experiment. One contributing factor to this rise in dissipation rate is the manner in which the kinematic boundary condition is applied to the top of the plate. In the KBC specification, nodes on the top surface are displaced downward at an equal rate. This leads to a situation that appears as though the beam is being loaded at mid-span by a “rigid plate”. As the displacements from this KBC grow large, plastic strain occurs in the region surrounding the “rigid-plate”. Thus additional dissipation, which is unrelated to the crack-tip field, is included in the calculation of the

dissipation rate. In addition, the “rigid-plate” specification results in a local compressive stress field directly below the area of KBC application that affects a larger region than a real-world displacement enforcement would. As the crack-tip region travels up the height of the beam, it is subjected to the influence of this compressive field. As a result of the Gurson constitutive assumptions, a reduction in pressure results in a decrease in the rate void growth. Since the rupture function is equal to the void volume fraction, the rupture function does not evolve as quickly as it did in the absence of this near tip compressive field. As a result, more plastic dissipation will occur for a given increment of crack extension.

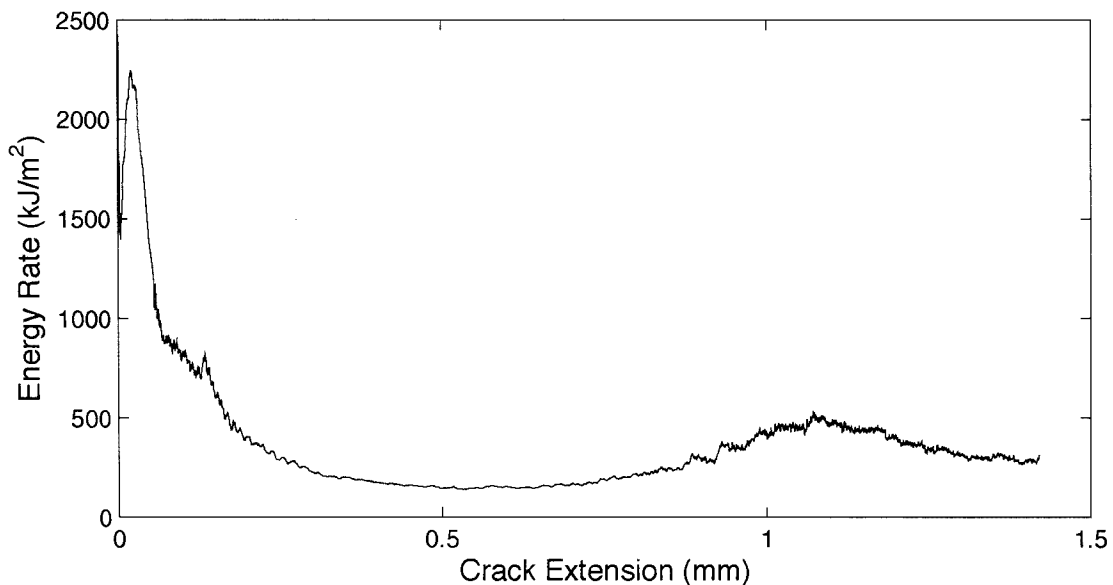


Figure 4.26: Dissipation Rate vs Crack Extension for Simulated 3-point Bend Test

While the dissipation rate is a useful quantity, it is difficult to calculate from experimental data. Instead, the use of J-R curves is widely accepted as the primary means by which data from an experimental fracture test is presented. Therefore Figure 4.27 presents the simulated J-R curve as calculated from the ASTM 1820 [53] procedure for 3-point bend specimens. The J-R curve exhibits typical characteristics of a 3-point bend

specimen in that the slope initially decreases with crack extension. After some amount of crack extension, boundary conditions influence the surface separation process as discussed above, which is reflected in the eventual increase in slope of the J-R curve.

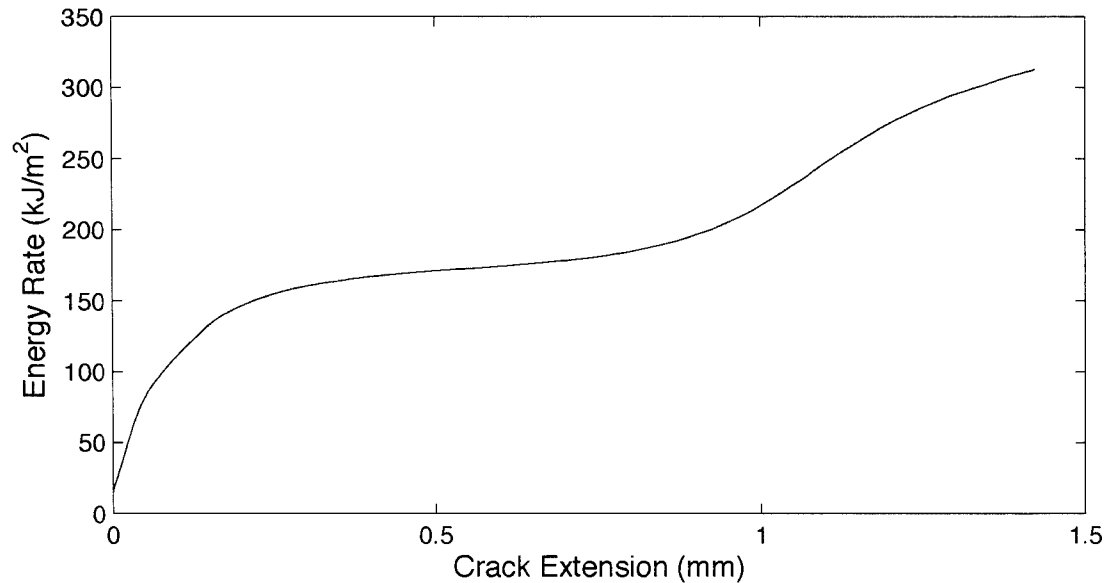


Figure 4.27: J-R Curve For Simulated 3-point Bend Test

4.8 Confinement Study of a 3-point Bend Specimen

In order to study how varying levels of confinement affects a CCF surface separation problem, a thin sheet 3-point bend mesh was also studied. This sheet mesh is similar to the previous geometry, but does not model the width of the specimen, as shown in Figure 4.28. This mesh consists of 6459 nodes, and 4612 elements with a minimum element dimension of 0.006 mm. A pair of constraints in the through-thickness direction is used to approximate plane stress and plane strain. The plane stress condition is achieved by simply constraining a single face of the specimen in the thru-thickness direction, while the plane strain constraint is a result of confining both front and back surfaces in the thru-thickness direction. These problems were run with the same loading rates as the fully 3-

dimensional mesh. Note that this “sheet” problem would be difficult to perform experimentally due to the potential for out-of-plane buckling.

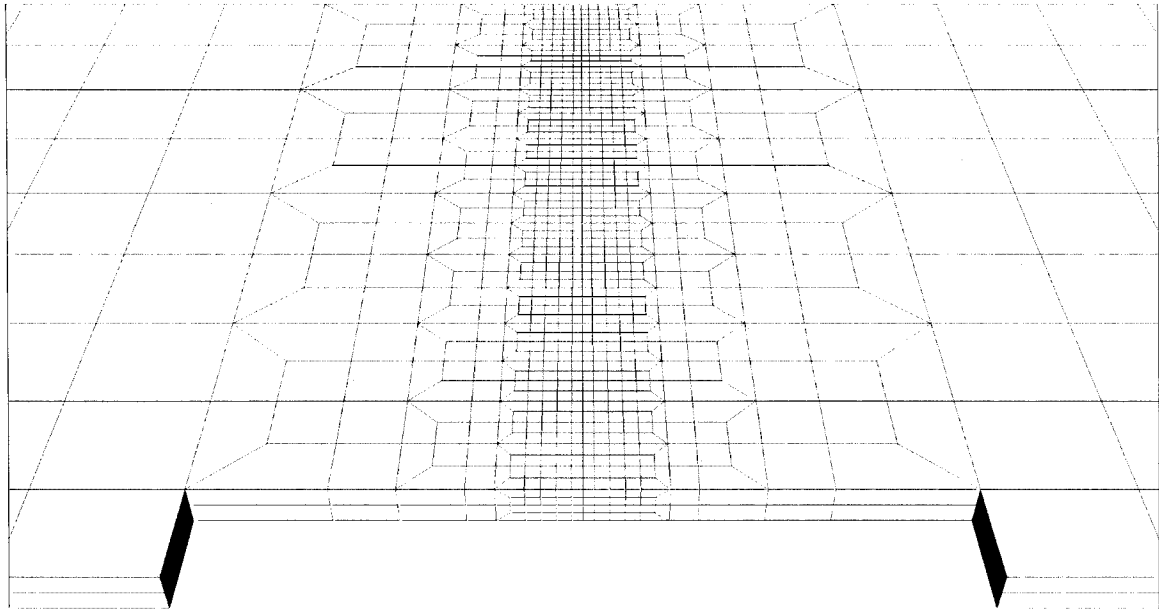


Figure 4.28: Sheet Mesh of 3-point Bend Specimen

Figure 4.29 plots the force per unit thickness against the *CMOD* for both the plane stress and plane strain analyses. The plane stress condition is observed to be much “tougher” than the plane strain condition, retaining its load carrying capacity well past the point at which the plane strain case has lost capacity. This qualitative observation is confirmed by the energy dissipation rate plot given in Figure 4.29, which shows that the plane stress problem requires ten times more dissipation per separation area than does the plane strain problem. This comparison suggests that the CCF is naturally suited to account for constraint effects, in contrast to the conventional cohesive zone method.

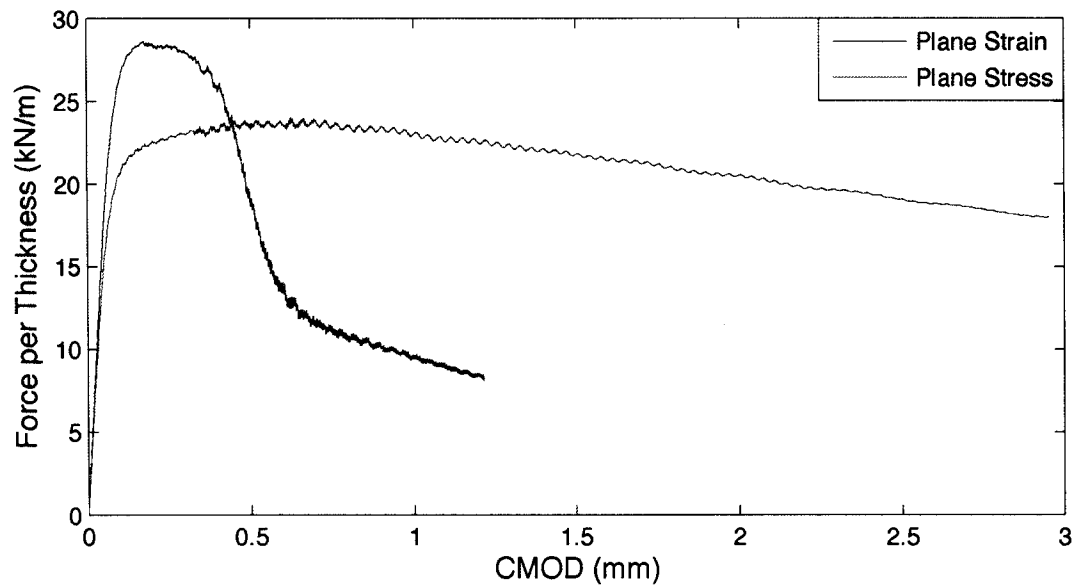


Figure 4.29: Force Per Unit Thickness vs CMOD from 3-point Bend Sheet Mesh

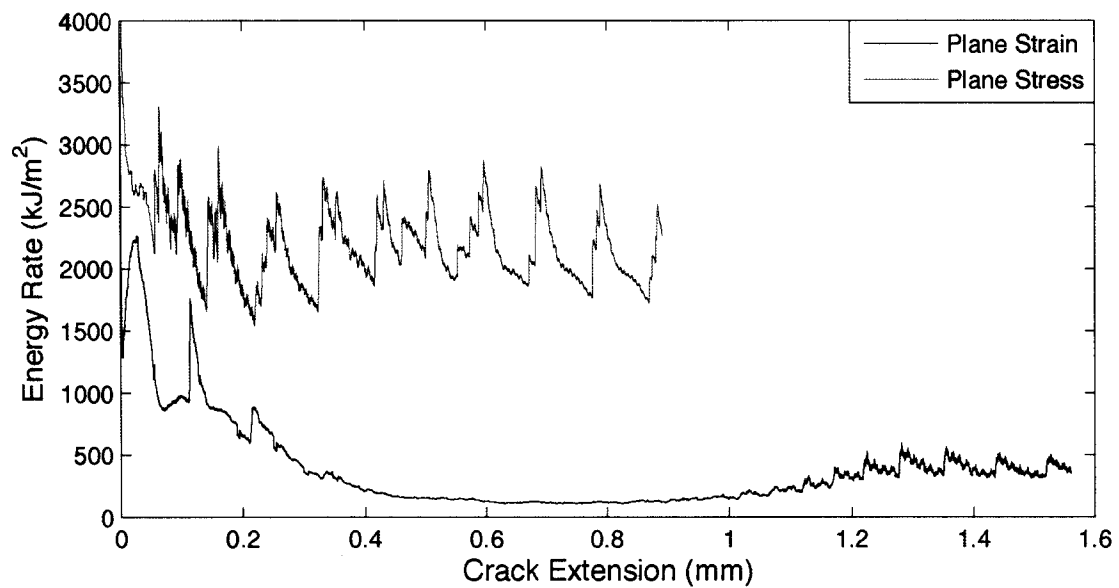


Figure 4.30: Energy Dissipation Rate vs Crack Extension from 3-point Bend Sheet Mesh

4.9 Summary

The Cohesive Continuum Framework has been enabled in an explicit dynamic Lagrangian finite element code for the purpose of exploring the behavior and capabilities of the CCF. A linear elastic constitutive relation was used in simple example problems and to model a brittle steel, while a Gurson dilatant plasticity void growth model was implemented to model a forged 21-6-9 steel. The surface based and finite thickness layer formulations have been implemented, although the surface based formulation was seen to perform poorly for near-incompressible materials, and therefore does not appear to be effective in conjunction with the Gurson material.

For purposes of initial evaluation of the CCF, a simple test plate problem was loaded in uniaxial strain, including 2 unloading cycles, to produce cohesive traction vs gap opening data as a point of comparison with standard cohesive zone models. In addition the linear elastic test plate was subjected to a complex loading path that contains changes in loading direction, including compression. In these analyses, the FTLF exhibited physically realistic behavior and displayed the ability to change loading direction and handle compression without difficulty. The unloading and subsequent reloading of the SBF showed that the use of an energy limiter results in energy dissipation for a complete unload/reload cycle. In addition, both versions of the CCF, as implemented in this study, exhibited modest departures from strict time continuity for certain mesh and loading configurations. Possible remedies were discussed.

Mesh refinement studies were performed on a linear elastic double cantilever beam, as well as on a cracked Gurson plate with periodic boundary conditions. In the case of the double cantilever beam, the analyses show excellent convergence when using both the FTLF and SBF. In the much more complex case of the Gurson plate, convergence under mesh refinement is again observed, albeit perhaps at a slower rate. Slight numerical instabilities are seen for the coarser meshes, but these may be controlled through the use of cohesive damping.

The procedure used to calibrate the Gurson constitutive parameters is discussed in detail. The results of the uniaxial tension simulation and the 3-point bend simulation are presented and compared with experimental data. Of note is that the analysis of the uniaxial tension test exhibits rupture initiation from the interior of the specimen, as is commonly observed in experiments on ductile metals. Furthermore, the shape of the rupture front in the 3-point bend specimen matches well with experiment.

Finally, a confinement study on a sheet mesh of the 3-point bend specimen was performed. The sheet mesh was subjected to boundary conditions such that plane stress and plane strain conditions are approached. The results of these analyses indicate that the plane stress case engenders much more dissipation per separation area than does the plane strain. Thus, the CCF is very capable of accounting for the effect of constraint, which is a ubiquitous feature of ductile fracture and which is not naturally captured in conventional cohesive-zone models.

5 Summary and Direction of Future Work

In this study, the Cohesive Continuum Framework (CCF) has been presented as a new tool for modeling the generation of new surfaces in a continuum body. While the CCF draws motivation from current cohesive zone methodology presented as in, e.g., [11-24, 28, 29], it is the stated goal the CCF to address certain shortcomings of standard cohesive zone formulations. In particular, the lack of an intrinsic dependence on near-tip constraint level is of substantial concern as discussed in [29-31]. Other issues include the mesh dependence of initially elastic cohesive zone models [23], and the time continuity of initially rigid cohesive zone models [24].

In the conventional cohesive zone construct, the cohesive traction is dependent only on the gap opening displacement. This fundamental assumption of the cohesive zone model represents a serious limitation in respect to modeling certain kinds of fracture behavior, and any attempt to develop an approach that is free from these limitations must ultimately depart from this simple form of the traction-separation relation. Herein, it is postulated that a standard bulk constitutive relation has the capability to generate cohesive tractions if appropriate kinematic input could be provided. From this postulate the concept of the gradient-like bridging tensor \mathbf{G} (section 2.2.2) emerges. In defining the kinematics of the rupturing material layer, two separate formulations been advanced. The finite thickness layer formulation (section 2.2.2.1) assumes the rupture process occurs within a finite thickness layer. On the other hand, the assumption that the rupturing material is idealized to a rupture surface leads to the surface based formulation (section 2.2.2.2). These formulations are treated as separate implementations of the CCF. Through the bridging

tensor, deformations from the surrounding bulk are integrated with the gap vector and length scale to generate kinematics that are used to update a material state through a standard constitutive relation. In section 2.2.3, the stress state of the enriched material is then used to generate the cohesive stress. The cohesive stress is applied to the body in a manner consistent with the kinematics that was used for the material update. To quantify the progression towards material rupture, a scalar rupture function is defined in section 2.2.1. This rupture function derives its value based on the material state in the rupturing layer; the material model is thereby required to supply state variables that correlate with the progression toward rupture.

The Cohesive Continuum Framework has been implemented in a 3-dimensional structural dynamics finite element code (CCFEM) written for the sole purpose of providing a test platform for the CCF. A detailed discussion of the implementation challenges is presented in chapter 3. Using this code, several analyses have been performed; their results are presented in chapter 4. Through the analyses in section 4.4.2, the CCF is seen to be capable of realistically modeling the rupture process through complex loading paths (i.e. change in loading direction, unloading, compression). Through mesh refinement studies of a linear elastic double cantilever beam (section 4.3), and a periodic array of cracks in an infinite plate (section 4.4), the convergence properties of the CCF under mesh refinement were studied. The periodic plate is of substantial note, as it represents a somewhat unstable dynamic crack growth problem. A procedure to calibrate material parameters along with the CCF rupture parameters was presented in section 4.5. This calibration procedure requires a simple 1-dimensional simulation, a 3-

dimensional uniaxial tension simulation (section 4.6), and a 3-point bend simulation (section 4.7). Through multiple simulations of each test, the material and rupture parameters are iteratively adjusted to give good agreement with experiment. Of special note is that the shape of the rupture front in the 3-point bend simulation agrees with experimental observations. In section 4.8, a 3-point bend sheet mesh is used to study constraint effects, whereby boundary conditions are used to produce plane stress and plane strain conditions in the bulk. These analyses illustrate the CCF's intrinsic ability to represent the effects of constraint. In these analyses, the plane stress simulation requires approximately 10 times more energy dissipation to generate a new surface than does the plane strain case.

Based on the success of the analyses presented in chapter 4, the Cohesive Continuum Framework appears to offer some attractive capabilities that are absent from the standard cohesive zone construct. The CCF provides a natural multi-axial capability, as well as the ability to undergo changes in loading directions without adverse consequences.

Furthermore, the CCF naturally resists compressive loading after the separation process has begun. However, there remains work to be done. The analysis in section 4.2.3 shows that the CCF does not guarantee time continuity in the acceleration across the rupture plane, although modification of the CCF to exhibit unconditional time continuity appears possible through the use of nodal scaling factors. Additionally, the surface based formulation as presented here does not perform well when a near-incompressible material is used. Since the surface based formulation is not subject to the same length-scale-to-

element-size restrictions as is the finite thickness layer formulation, it would be a worthwhile endeavor to develop a more robust SBF implementation.

References

1. T.L. Anderson, *Fracture Mechanics*, CRC Press, (2005).
2. C.E. Inglis, "Stresses in a Plate Due to the Presence of Crack and Sharp Corners." *Transactions of the Institute of Naval Architects*, Vol. 55, pp. 219-241, (1913).
3. A.A. Griffith, "The Phenomena of Rupture and Flow in Solids." *Philosophical Transactions*, Series A, Vol. 221, pp. 163-198, (1920).
4. H.M. Westergaard, "Bearing Pressure and Cracks", *Journal of Applied Mechanics*, Vol. 6, pp. 49-53, (1939).
5. G.R. Irwin, "Analysis of Stresses and Strains near the End of a Crack Traversing a Plate." *Journal of Applied Mechanics*, Vol. 24, pp. 361-364, (1957).
6. I.N. Sneddon, "The distribution of stress in the Neighborhood of a Crack in an Elastic Solid.", *Proceedings, Royal Society of London*, Vol. A-187, pp. 229-260.
7. M.L. Williams, "On the Stress Distribution at the Base of a Stationary Crack." *Journal of Applied Mechanics*, Vol. 24, pp. 109-114, (1957).
8. J.R. Rice, "A Path Independent Integral and the Approximate Analysis of Strain Concentration of Notches and Cracks." *Journal of Applied Mechanics*, Vol. 35, pp. 379-386, (1968).
9. J.W. Hutchinson, "Singular Behavior at the End of a Tensile Crack Tip in a Hardening Material", *Journal of the Mechanics and Physics of Solids*, Vol. 16, pp. 13-31, (1968).
10. J.R. Rice and G.G. Rosengren, "Plane strain deformation near a crack tip in a power-law hardening material." *Journal of the Mechanics and Physics of Solids*, Vol. 16, pp. 1-12, (1968).
11. D.S. Dugdale, "Yielding of steel sheets containing slits", *Journal of the Mechanics and Physics of Solids*, Vol. 8, pp. 100-104, (1960).
12. G.I. Barenblatt, "The mathematical theory of equilibrium cracks in brittle fracture", *Advances in Applied Mechanics*, Vol. 7, pp. 55-129, (1962).
13. A. Needleman, "A continuum model for void nucleation by inclusion debonding", *Journal of Applied Mechanics*, Vol. 54, pp. 525-531, (1987).
14. J. R. Rice and J.S. Wang, "Embrittlement of Interfaces by Solute Segregation", *Materials Science and Engineering*, Vol. A107, pp. 23-40, (1989).
15. A. Needleman, "An analysis of decohesion along an imperfect interface", *International Journal of Fracture*, Vol. 42, pp. 21-40, (1990).
16. X.P. Xu and A. Needleman, "Numerical simulations of fast crack growth in brittle solids", *J. Mech. Phys. Solids*, Vol. 42, pp. 1397-1434, (1994).
17. X.P. Xu and A. Needleman, "Numerical simulations of dynamic interfacial crack growth allowing for crack growth away from the bond line", *Int. J. Fracture*, Vol. 74-3, pp. 253-275, (1995).
18. X.P. Xu and A. Needleman, "Numerical simulations of dynamic crack growth along interface", *Int. J. Fracture*, Vol. 74-4, pp. 289-324, (1995).
19. V. Tvergaard and J.W. Hutchinson, *Journal of the Mechanics and Physics of Solids*, Vol. 40, pp. 1377-1397, (1992).
20. G.T. Camacho and M. Ortiz, "Computational Modelling of Impact Damage in Brittle Materials", *Int. J. Solids Structures*, Vol. 33, pp. 2899-2938, (1996).

21. G.T. Camacho and M. Ortiz, "Adaptive Lagrangian modelling of ballistic penetration of metallic targets", *Comp. Methods Appl. Mech. Engrg.*, Vol. 142, pp. 269-301, (1997).
22. M. Ortiz and A. Pandolfi, "Finite-deformation irreversible cohesive elements for three-dimensional crack-propagation analysis", *International Journal of Numerical Methods in Engineering*, Vol. 44, pp. 1267-1282, (1999).
23. P. Klein, J. Foulk, E.P. Chen, S. Wimmer, H. Gao, "Physics based modeling of brittle fracture: cohesive formulations and applications and mesh-free methods", *Sandia National Laboratory Technical Report*, SAND2001-8099, (2000).
24. K.D. Papoulia, Chin-Hang Sam, and S.A. Vavasis, "Time Continuity in Cohesive Finite Element Modeling", *International Journal of Numerical Methods in Engineering*, Vol. 58, pp. 679-701, (2003).
25. D. C. Drucker, "Some implications of work-hardening and ideal plasticity", *Quarterly Appl. Math*, Vol. 7, pp. 411-418, (1950).
26. R. Hill, "A general theory of uniqueness and stability in elastic-plastic solids", *J. Mech. Phys. Solids*, Vol. 6, pp. 236-249, (1958).
27. J. R. Rice, "The localization of plastic deformation", in: *W. Koiter (Ed.), Theoretical and Applied Mechanics*, pp. 207-220, (1976).
28. K.K. Mathur, A. Needleman, V. Tvergaard, "Three dimensional analysis of dynamic ductile crack growth in a thin plate", *J. Mech. Phys. Solids*, Vol. 44, pp. 439-464 (1996).
29. F. Costanzo, "A continuum theory of cohesive zone models: deformation and constitutive equations", *International Journal of Engineering Science*, Vol. 36, pp. 1763-1792, (1998).
30. T. Siegmund and W. Brocks, "Prediction of the work of separation and the implications to modeling", *Int. J. Fracture*, Vol. 99, pp. 97-116, (1999)
31. T. Siegmund and W. Brocks, "A numerical study on the correlation between the work of separation and the dissipation rate in ductile fracture", *Eng. Fracture Mech.*, Vol. 67, pp. 139-154, (2000)
32. A.L. Gurson, "Continuum theory of ductile rupture by void growth: part I—yield criteria and flow rules for porous ductile media," *ASME J. Eng. Mater. Technol.*, Vol. 99, pp. 2, (1977).
33. A.L. Gurson, "Porous rigid-plastic material containing rigid inclusions - Yield function, plastic potential, and void nucleation", *Proc. Int. Conf. Fracture*, Vol. 2A, pp 357-364, (1977).
34. M. M. Rashid, "Incremental kinematics for finite element applications", *International Journal for Numerical Methods in Engineering*, Vol. 36, pp. 3937-3956, (1993).
35. D.P. Flanagan, and T. Belytschko, "Eigenvalues and Stable Time Steps for the Uniform Strain Hexahedron and Quadrilateral", *Journal of Applied Mechanics*, Vol. 51, pp. 35-51, (1984).
36. D.P. Flanagan and T. Belytschko, "A Uniform Strain Hexahedron and Quadrilateral with Orthogonal Hourglass Control", *International Journal for Numerical Methods in Engineering*, Vol. 17, pp. 679-607, (1981).
37. T. Belytschko, J.S.-J.Ong, W.K. Liu, and J.M. Kennedy, "Hourglass Control in Linear and Nonlinear Problems", *Computer Methods in Applied Mechanics and Engineering*, Vol. 43, pp. 251-276, (1984).

38. J.C. Nagtegaal, D.M. Parks, J.R. Rice, "On numerically accurate finite element solutions in the fully plastic range", *Comput. Meth. Appl. Mech. Eng.*, Vol. 4, pp.153-77, (1974).
39. T.J.R. Hughes, "Generalization of selective integration procedures to anisotropic and nonlinear media", *Internat. J. Numer. Meths. Engrg.*, Vol. 15 pp.1413-18, (1980).
40. J.C. Simo and S. Rifai, "A class of mixed assumed strain methods and the method of incompatible modes", *International Journal of Numerical Methods in Engineering*, Vol 29, pp. 1595-1638, (1990).
41. J.C. Simo and F. Armero, "Geometrically non-linear enhanced strain mixed methods and the method of incompatible modes", *International Journal of Numerical Methods in Engineering*, Vol. 33, pp. 1413-1449, (1992).
42. J.C. Simo and F. Armero, and R.L. Taylor "Improved version of assumed enhanced strain tri-linear elements for 3D finite deformation problems", *Comp. Meth. Appl. Mech. Engng.* Vol. 110, pp. 359-386. (1993)
43. E.A. de Souza Neto, D. Peric, M. Dutko, and D.R.J. Owen, "Design of Simple Low Order Finite Elements for Large Strain Analysis of Nearly Incompressible Solids", *International Journal of Solids and Structures*, Vol. 33, pp. 3277-96. (1996)
44. M.M. Rashid and M. Selimotic, "A three dimensional finite element method with arbitrary polyhedral elements", *International Journal of Numerical Methods in Engineering*, in press.
45. J.R. Rice and D.M. Tracey, "On the ductile enlargement of voids in triaxial stress fields", *Journal of Mechanics and Physics of Solids*, Vol. 17, pp. 201-217, (1969).
46. A. Needleman and V. Tvergaard, "An Analysis of ductile rupture in notched bars", *J. Mech. Phys. Solids*, Vol. 32, pp. 461-490, (1984).
47. A. Needleman, and J.R. Rice, "Limits to ductility set by plastic flow localization", *Mechanics of Sheet Metal Forming*, pp. 237-267, (1978).
48. C.C. Chu and A. Needleman, "Void Nucleation effects in biaxially stretched sheets", *J Eng. Materials Technol.*, Vol. 102, pp. 249-256 (1980).
49. V. Tvergaard, "Influence of voids on shear band instabilities under plane strain conditions." *Int. J. Fracture*, Vol. 17, pp. 389-407, (1981).
50. V. Tvergaard, "On localization in ductile materials containing spherical voids", *Int. J. Fracture*, Vol. 18, pp. 237-252, (1982).
51. L.M. Brown, Embury, J.D, "The initiation and growth of voids as second phase particles", *Proc. 3rd Int. Conf. on Strength of Metals and Alloys*, pp. 164-169, (1973).
52. H. Andersson, "Analysys of a model for void growth and coalescence ahead of a moving crack tip", *J. Mech. Phys. Solids*, Vol. 25, pp. 217-233, (1977).
53. ASTM E 1820-99. *Annual Book of ASTM Standards*, Vol. 03.01, pp. 972-1005, (1999).